INTERACTIONS OF AZOLE MOLECULES WITH COPPER IONS AND COPPER SURFACES COVERED WITH CHEMISORBED H, O, OH OR Cl

Matjaž Dlouhy

Doctoral Dissertation
Jožef Stefan International Postgraduate School
Ljubljana, Slovenia

Supervisor: Prof. Dr. Anton Kokalj, Department of Physical and Organic Chemistry, Jožef Stefan Institute, Ljubljana, Slovenia

Evaluation Board:
Prof. Dr. Ingrid Milošev, Chair, Department of Physical and Organic Chemistry, Jožef Stefan Institute, Ljubljana, Slovenia
Asst. Prof. Dr. Črtomir Podlipnik, Member, Faculty of Chemistry and Chemical Technology, University of Ljubljana, Ljubljana, Slovenia
Dr. Christian Feiler, Member, Institute of Surface Science, Helmholtz-Zentrum Hereon, Geesthacht, Germany

MEDNARODNA PODIPLOMSKA ŠOLA JOŽEFA STEFANA
JOŽEF STEFAN INTERNATIONAL POSTGRADUATE SCHOOL

Matjaž Dlouhy

INTERACTIONS OF AZOLE MOLECULES WITH COPPER IONS AND COPPER SURFACES COVERED WITH CHEMISORBED H, O, OH OR Cl

Doctoral Dissertation

INTERAKCIJE AZOLNIH MOLEKUL Z BAKROVIMI IONI IN BAKRENIMI POVRŠINAMI, PREKRITIMI S KEMISORBIRANIM H, O, OH ALI Cl

Doktorska disertacija

Supervisor: Prof. Dr. Anton Kokalj

Ljubljana, Slovenia, May 2023

We think of life as an inexhaustible well. And yet everything happens only a certain number of times, and a very small number really. How many more times will you remember a certain afternoon of your childhood, some afternoon that's so deeply a part of your being that you can't even conceive of your life without it? Perhaps four, or five times more? Perhaps not even that. How many more times will you watch the full moon rise? Perhaps twenty. And yet it all seems limitless.

—Paul Bowles, *The Sheltering Sky*

Acknowledgments

Completing a doctoral dissertation is a challenging and rewarding journey, and it would not have been possible without the support and encouragement of many.

I am immensely indebted to my mentor Prof. Dr. Anton Kokalj for his guidance, patience, and direction throughout my studies. His feedback and advice have been instrumental in my success, and I am deeply thankful for the opportunities and knowledge he provided me with.

I would like to extend a special thanks to Senior Research Associate Dr. Antonija Lesar, who saw my passion for research and motivated me to take on the research journey. Her recognition gave me the confidence and drive to pursue my goals. Additionally, I am incredibly grateful to Prof. Dr. Ingrid Milošev for giving me a chance all those years ago. Their willingness to take a chance on me has been a pivotal moment in my career.

I am appreciative of the Slovenian Research Agency for their financial support through grant number PR-08976. This funding has enabled me to carry out my research, and I am honored for the opportunity to be able to contribute to my field of study.

I would like to thank the members of the evaluation committee for their expertise, time and efforts in evaluating my work. Their valuable feedback has helped me to improve the form of my thesis and has undoubtedly contributed to the overall quality of the work.

To my colleagues, both past and present, thank you for your help, discussions, lunches, and willingness to listen. Your contributions to my research and your support during the ups and downs have been invaluable, and I am happy for the time we have spent together.

To my friends, both old and the ones I made along the way, I want to express my deepest gratitude. You have been my companions throughout my journey, and I cannot thank you enough for your friendship, encouragement, and support. Your belief in me, your kind words, and your warm embraces have been a constant source of strength and inspiration, and I could not have made it through this without you. The memories we have shared and the laughter we have exchanged will forever be etched in my heart, and I am grateful for every one of you. I am truly blessed to call all of you my friends, and I will cherish our bonds for the rest of my life.

Finally, I would like to express my deepest gratitude to my family. Your faith in me, unconditional love, and unwavering support have been a constant source of strength throughout my life. During stormy days, you have always been there for me, providing a listening ear and words of encouragement. You are the ones who stand by my side, show me light when all others fade, and give me hope for help, upon which I can always rely. I am truly grateful for your presence in my life, as you have been my rock and my anchor. Without your belief in me, I would not be where I am today. I thank you not only with my words but with everything I have become.

To all who have contributed to my journey, I would once again like to express my heartfelt appreciation.

Iskrena hvala in globok poklon vsem.

Abstract

In real environments, copper and other metal surfaces are never clean. Even during active dissolution in corrosion, they are likely to be covered with adsorbed corrosion-relevant species such as O, OH, H, and Cl. To explore the impact of such species on the bonding of imidazole, used herein as an archetypal model of azole corrosion inhibitors on Cu(111), we conducted a systematic computational study based on the Density-Functional Theory. Over 400 diverse adsorption configurations were considered, with close attention paid to the effects of variables such as surface coverage, the type of corrosion-relevant species, and the distance between the imidazole molecule and the corrosion-relevant species. We demonstrate that O and Cl enhance the adsorption bonding of imidazole, while H has almost no effect, and OH either diminishes or has a negligible impact on the imidazole adsorption. The effect of the adsorbed corrosion-relevant species on the imidazole adsorption usually diminishes with the increasing distance between adsorbed species and imidazole, and with decreasing coverage of corrosion-relevant species. We identified three coadsorption effects of O, OH, H, and Cl on the non-dissociative adsorption of imidazole, including hydrogen bond formation, enhancement of the N–Cu bond, and work-function change induced by coadsorbates. We also found that if the coverage of corrosion-relevant species is too high, then the chemisorption of imidazole is prevented either sterically or due to the unavailability of free surface sites.

Moreover, our study shows that chemisorbed O and OH species promote deprotonation of azole molecules on the investigated copper surfaces, as exemplified by benzotriazole, imidazole, and Cu(111). The N–H bond cleavage is involved in such deprotonation. By undergoing molecular deprotonation during adsorption, the resulting adsorption states are more stable, which increases the persistence of chemisorbed azole molecules. Our findings demonstrate that deprotonated benzotriazole molecules exhibit stability that is roughly 1 eV higher on O/Cu(111) and OH/Cu(111), compared to an adsorbed intact molecule on bare Cu(111). However, for imidazole, the degree of stabilization is significantly weaker and ranges from 0.1 to 0.5 eV.

Further, we investigated the formation of coordination complexes between copper central ions and 19 different N-heterocyclic inhibitor molecules in an aqueous medium, using a cluster/continuum model, which involves a few explicit water molecules and the surrounding water described implicitly. Our results indicate that most of the investigated ligands have the potential to coordinate with Cu(I) and Cu(II) ions, forming stable two- or four-coordinated complexes, respectively. The thermodynamic stability of these coordination compounds was also evaluated.

Povzetek

V naravi baker in druge kovinske površine niso nikoli čiste. Tudi med aktivnim raztapljanjem pri koroziji so verjetno prekrite s korozijsko pomembnimi zvrstmi, kot so O, OH, H in Cl, adsorbiranimi na površini materiala. Da bi raziskali vpliv takšnih zvrsti na vezavo imidazola, ki smo ga uporabili kot arhetipski model azolnih inhibitorjev korozije na Cu(111), smo izvedli sistematično modelno študijo, ki temelji na teoriji gostotnega funkcionala. Upoštevali smo več kot 400 različnih adsorpcijskih konfiguracij, pri čemer smo posebno pozornost namenili vplivu spremenljivk, kot so pokritost površine, vrsta korozijsko pomembnih zvrsti ter razdalja med molekulo imidazola in korozijsko pomembno zvrstjo. Dokazali smo, da O in Cl ojačata adsorpcijo imidazola, medtem ko H skoraj nima učinka, OH pa bodisi oslabi adsorpcijo imidazola bodisi ima zanemarljiv vpliv nanjo. Pokazali smo, da se vpliv adsorbiranih korozijsko pomembnih zvrsti na adsorpcijo imidazola zmanjšuje z večanjem razdalje med adsorbiranimi zvrstmi in imidazolom ter z zmanjševanjem pokritosti korozijsko pomembnih zvrsti. Na podlagi naših raziskav smo izluščili tri učinke, ki jih imajo zvrsti O, OH, H, in Cl na adsorpcijo imidazola. To so: nastanek vodikove vezi, ojačitev vezi N–Cu in spememba izstopnega dela, ki jo povzročijo omenjeni koadsorbati. Pokazali smo, da se imidazol ne more kemisorbirati na Cu(111), če je pokritost s korozijsko pomembnimi vrstami prevelika, bodisi zaradi steričnih preprek bodisi zaradi nerazpoložljivosti prostih mest na površini materiala.

Na primeru inhibitorjev benzotriazola in imidazola ter površine Cu(111) ugotavljamo, da kemisorbirana O in OH spodbujata deprotonacijo adsorbiranih azolnih molekul. Deprotonacija vključuje cepljenje vezi N–H pri benzotriazolu in v manjši meri vezi C–H pri imidazolu. Z molekulsko deprotonacijo med adsorpcijo lahko nastanejo stabilnejša adsorpcijska stanja, kar poveča obstojnost kemisorbiranih molekul. Naše ugotovitve kažejo, da je stabilnost deprotonirane molekule benzotriazola na O/Cu(111) in OH/Cu(111) za približno 1 eV višja v primerjavi z adsorbirano molekulo v nespremenjeni osnovni obliki na čisti površini Cu(111). Na primeru imidazola je stopnja stabilizacije bistveno šibkejša in znaša od 0,1 do 0,5 eV.

Nadalje smo raziskali nastanek koordinacijskih kompleksov med bakrovimi ioni in 19 različnimi N-heterocikličnimi molekulami inhibitorjev v vodnih medijih z uporabo gručno/kontinuirnega modela, kjer je nekaj molekul vode opisanih ekplicitno, ostala voda pa je upoštevana implicitno. Naši rezultati kažejo, da večina preučevanih ligandov koordinira z ioni Cu(I) in Cu(II), pri čemer Cu(I) tvori stabilne dvokoordinirane, Cu(II) pa štirikoordinirane komplekse. Ocenili smo tudi termodinamično stabilnost teh koordinacijskih kompleksov.

Contents

List of Figures

List of Tables

Abbreviations

DefTZVP ... triple-zeta basis set of Ahlrichs including valence polarization functions
DFT ... density-functional theory
MN15 ... Minnesota-15 functional
PAW ... projector augmented wave method
PBE ... Perdew–Burke–Erzenhof
PBE-D2 ... PBE functional with the D2 empirical dispersion correction of Grimme
PBE+D" ... reparametrized PBE-D2 functional
PWscf ... plane-wave self-consistent-field program
PWTK ... PWscf ToolKit
SMD ... solvation model based on density
ZPE ... zero-point energy

Symbols

Constants

e	elementary charge	$1.602177 \cdot 10^{-19}$ C
h	Planck constant	$6.626070 \cdot 10^{-34}$ kg m^2 s^{-2}
k_B	Boltzmann constant	$1.380649 \cdot 10^{-23}$ kg m^2 s^{-2} K^{-1}

Units

Å	ångström	$1 = 10^{-10}$ m
atm	standard atmosphere	1 atm = 101325 kg m^{-1} s^{-2}
Borh	bohr	1 bohr = $5.2918 \cdot 10^{-11}$ m
D	debye	1 D = $3.3356 \cdot 10^{-30}$ C m
eV	electronvolt	1 eV = $1.6022 \cdot 10^{-19}$ kg m^2 s^{-2}
K	kelvin	1 K = −272.15 °C
M	molarity	1 M = 1 g mol^{-1}
ML	monolayer	1 ML = n^2 adsorbates in $(n \times n)$ supercell
nn$_\mathrm{Cu}$	nearest-neghbour Cu–Cu distance	1 nn$_\mathrm{Cu}$ = $2.5822 \cdot 10^{-10}$ m
Ry	rydberg	1 Ry = $2.1799 \cdot 10^{-18}$ kg m^2 s^{-2}

Other symbols

br	bridge adsorption site
C_6	dispersion coefficient
χ	electronegativity
d	adsorbate height
E	total energy of a system
ΔE	a change of energy as a system goes from state A to state B
E_0	the Kohn-Sham energy computed at absolute zero temperature without considering the zero-point energy
E_ads	adsorption energy
E_b	molecular adsorption binding energy
ΔE_b	binding energy describing the effect of the coadsorbates on the non-dissociative adsorption
$\Delta E_\mathrm{deproto}$	deprotonation reaction energy
E_des	desorption energy
E_form	energy of a formation of a coordination complex
ΔE_stab	total stabilization energy
E_trv	thermal energy of translation, rotation, and vibration
η	chemical hardness
fcc	face-centered-cubic three-fold hollow adsorption site
G	Gibbs energy
$\Delta G^{\ominus}$	standard reaction Gibbs energy
hcp	hexagonal-close-packed three-fold adsorption site

IE	...	inhibition efficiency
L	...	azole-type ligand
Mol	...	deprotonated molecule
MolH	...	intact molecule
μ	...	chemical potential
ΔN	...	electron charge transfer
N_{ineq}	...	number of symmetry inequivalent top sites
ν	...	frequency
$\Delta\Phi$	...	adsorption-induced work-function change
ρ	...	electron charge density
$\Delta\rho$	...	electron charge density difference
S	...	entropy
T	...	temperature
τ	...	residence time
Θ	...	surface coverage expressed in monolayer units
θ	...	surface coverage expressed in Bohr^{-2}
top	...	top adsorption site
υ	...	stoichiometric coefficient
X	...	a generic label designating H, O, OH, or Cl

Chapter 1

Introduction

> *Hephaistos answered, /.../*
> *"I can find him armor that shall amaze the eyes of all who behold it."*
> *He threw tough copper into the fire, /.../*
> *He set his great anvil on its block,*
> *With one hand grasped his mighty hammer /.../*
> *And with many wonders did his cunning hand enrich it.*
>
> —Homer, *Iliad*, 18: 462–478
>
> (translation by S. Butler)

Copper has been used and applied in many ways over the past 11,000 years. Due to its excellent mechanical and chemical properties, thermal conductivity, and corrosion resistance, it is an invaluable metal in many fields of industry, architecture, and art [1]. Consequently, copper is often exposed to harsh environments containing a variety of aggressive species that could cause corrosion.

Corrosion is a spontaneous natural chemical process with a tremendous negative impact on the environment and the global economy, with estimated costs annually reaching approximately 250 euros per global capita [2]. While corrosion cannot be prevented, different modes of protection can mitigate its effects on the destruction of materials.

Depending on the application, different modes of protection are used to decelerate corrosion. For closed systems, such as oil pipelines, boilers, cooling systems, and storage tanks, corrosion inhibitors are often applied [3]. Corrosion inhibitors are substances used in low concentrations that can considerably slow down the corrosion of metals and alloys [3], [4].

An extensive effort is being made to replace chromate-based corrosion inhibitors (which are carcinogenic) with more eco-friendly and biodegradable organic alternatives [3], [5]. Many studies are being conducted to determine whether a vast variety of organic molecules can be used as efficient corrosion inhibitors. According to Winkler [6], as many as 10^{80} small organic molecules are potential candidates for corrosion inhibitors, making the selection almost infinite. Among them, azoles—five-membered aromatic compounds containing one nitrogen atom and at least one other heteroatom (N, O, or S)—and their derivatives have long been known for their ability to mitigate corrosion of copper and its alloys.

Although the exact mechanism of how inhibitors impede corrosion is usually not known, it is generally accepted that a molecule must adsorb to act as an inhibitor [7], [8]. Interactions between inhibitor molecules and, mostly, bare metal surfaces have already been comprehensively investigated by many experimental and computational studies by our group and those of others (see Refs. [9], [10] and the references therein). Obot et al. [11] justifiably criticized such calculations as naive because in real environments metal surfaces are most likely never clean. Copper forms a thin oxide layer that can considerably reduce the rate of corrosion reactions. However, in the case of localized corrosion, exposed bare surfaces are likely to be covered with adsorbed species contained in the corrosive media, such as H, O, OH, and Cl. The first three species are typically involved in cathodic corrosion reactions, either oxygen reduction or hydrogen evolution. In contrast, chloride can activate the anodic corrosion reaction – the dissolution of a metal. The lack of studies dealing with the effects of these chemisorbed species on the adsorption of inhibitor molecules has created a void in understanding the fundamental aspects of corrosion inhibition, such as their effect on the surface electronic properties (e.g., work function and band gap), adsorption bonding, lateral cohesive intermolecular forces between adsorbed molecules and other coadsorbed species, and the possibility of dissociative chemisorption or other chemical transformations of inhibitors upon adsorption, to list a few. This void is addressed in this thesis by means of molecular modeling based on density-functional theory (DFT). In order to better understand physiochemical properties that cannot be explained with experimental tools, computational molecular modeling is increasingly being utilized in many fields of research, also corrosion science.

One of the most obvious advantages of computational modeling is that one has direct control over atomic positions and can relate structural properties to electronic ones. A detailed knowledge of the geometries of all species involved in a specific reaction is thus required. Interaction between species are due to valence electrons, therefore the quantum mechanical description of the corresponding process is necessary. In quantum mechanics, a system of interest, whether it is an atom, a molecule, or a solid is described with the Schrödinger equation. A direct solution to an exact many-body Schrödinger equation problem is impossible, hence many approximations and methods have been developed to address this issue.

DFT proposes a radically different approach to solving a many-body problem compared to wave-function-based methods. Hohenberg and Kohn demonstrated in 1964 that the ground state electron density contains all the necessary information for any given system. In the following year, Kohn and Sham (1965) established that density can be determined by solving an effective one-particle problem. This resulted in an enormous computational breakthrough as systems, such as surfaces and large molecules with hundreds of atoms could be investigated.

In the past decade, computational studies based on DFT gained momentum as a tool for screening new potential corrosion inhibitor molecules and for studying their adsorption characteristics [10]. As molecular adsorption represents an important step in achieving the inhibitory effect, it is crucial to investigate the adsorption bonding also from an atomistic perspective. Modeling based on DFT utilizing a periodic slab model of a surface is often incorporated into studies as a synergistic lever that contributes to the understanding of experimental research in the field of corrosion science.

It should be noted, as already pointed out by Kokalj [12], that despite a sane intuitive "*strong adsorption*" premise, DFT calculations revealed that some outstanding inhibitors of copper, such as benzotriazole and several other azoles, interact only weakly with bare copper surfaces. For example, an intact benzotriazole molecule bonds only by about 0.5 eV onto Cu(111) surface [13], [14], which is similar in strength to the solvation interaction between benzotriazole molecule and water solvent [15], [16]. On the other hand, Cl atom binds around 4-times more strongly to the Cu(111) surface than an intact benzotriazole molecule. This observation questions the "*the stronger the adsorption, the better the inhibitor*" premise because benzotriazole is an outstanding inhibitor for copper, whereas chloride is a well-known corrosion activator.

However, as important as the binding between the inhibitor and the surface may be, it is only one among various aspects to be considered. Kutej et al. [17] provided another example; they investigated coadsorption phenomena and proposed an interesting indirect mechanism of corrosion inhibition, indicating that the inhibitor enhances the binding of hydrogen at sites located within a certain radius from the adsorbed inhibitor, thus impeding the hydrogen evolution, which is a cathodic reaction.

Almost a barrierless dissociative adsorption of some azole corrosion inhibitors in the close proximity of surface O or OH species have been reported in recent years by our group [18]–[20] and others [21], [22]. This thesis tries to explore this phenomenon further on the molecular level by focusing on the adsorption behavior of some common azole compounds, such as imidazole and benzotriazole, on a surface previously covered with O or OH.

The Cl^- induced corrosion proceeds through a dissolution of metal via the formation of soluble $[CuCl_2]^-$ complexes [5]. It seems that the strong bonding of Cl to the surface weakens the bonds between Cu atoms thus resulting in the formation of more stable soluble copper–chloride complexes [23]. Computational studies in the literature mainly focus on the adsorption of inhibitor molecules at surfaces. In contrast, their interaction with metal ions in an aqueous solution and the formation of coordination complexes are rarely addressed in the context of corrosion inhibition. The formation of stable and soluble coordination complexes may help accelerate the anodic dissolution of metals by forming stable soluble complexes with metal ions that can participate in the anodic dissolution process. A thorough review of the literature reveals that some computational studies have addressed the coordination complexation of inhibitor molecules with metal ions in terms of corrosion protection [24], [25]. However, a more comprehensive and systematic computational study is called for, as there is no uniform consensus on what makes a certain molecule a good corrosion inhibitor.

Investigation of coordination complexes formed in corrosive media between metal ions and inhibitor molecules is an important step toward understanding why inhibitor molecules that bind strongly to metal surfaces do not necessarily act as efficient inhibitors. By forming stable and soluble complexes between inhibitor molecules and copper ions, corrosion could be accelerated. In contrast, insoluble complexes could precipitate from aqueous media to the metal surface, creating a protective barrier. This implies that studying complexes between inhibitor molecules and metal ions is relevant, yet such studies are scarce in the literature.

Chapter 2

Aim of Work

The purpose of this thesis is to extend computational studies relevant to corrosion inhibition by exploring interactions between corrosion inhibitor molecules and other species present on a copper surface, as well as with dissolved copper ions that may be present in the aqueous medium surrounding it. The results presented in this thesis are, therefore, divided into two parts.

In the first part, the thesis employs a systematic molecular modeling approach to scrutinize the adsorption characteristics of imidazole and to some extent benzotriazole at the atomic level. The main focus is devoted to studying the interactions occurring at the vacuum/surface interface using periodic-boundary conditions. The primary purpose is to perform a systematic computational study in order to understand how, and to what extent corrosion-relevant species, like H, O, OH, and Cl, affect the adsorption of the inhibitor molecule to the copper surface. It also strives to evaluate the imidazole and benzotriazole dissociative adsorption induced by chemisorbed O and OH.

In the second part, some light is shed on the formation of coordination complexes between corrosion inhibitors and hydrated copper ions. To this end, 19 different N-heterocyclic molecules and Cu(I) or Cu(II) ions are considered. It is worth noting that this aspect is only rarely addressed by computational methods in the literature. The thesis thus aims to find connections between formed copper ion–molecule complexes and corrosion inhibition properties of the investigated molecules.

2.1 Hypotheses

Originating from the aim of the thesis, the following hypotheses have been postulated:

1. Chemisorbed H, O, OH, and Cl affect the adsorption of the inhibitor molecule.

2. The nature and extent of the effect of H, O, OH, or Cl on the adsorbed inhibitor molecules depend on the proximity of the molecule, the type of chemisorbed species, and surface coverage.

3. Chemisorbed O and OH promote the dissociative adsorption of imidazole and benzotriazole.

4. Cu(I) and Cu(II) ions interact with investigated azole molecules in an aqueous medium, resulting in the formation of coordination complexes.

Chapter 3

Technical Details

This chapter is divided into two sections. The first section briefly describes the computational method and other technical details used in the computational modeling of adsorption on copper surfaces. The second section provides a detailed description of the computational method used to perform calculations of coordination complexes between copper ions and N-heterocyclic molecules in the aqueous solvent. Both sections also define the relevant thermodynamic quantities, chemical reactions considered, and other technical details, notations, and definitions used in this work.

3.1 Absorption Calculations

Technicalities connected to the method used to perform the adsorption calculations on Cu(111) are described below. First, computational details are briefly addressed, followed by an explanation of how the thermodynamic stability of the systems was evaluated.

3.1.1 Computational details

DFT calculations were performed using the PBE+D" method, which consists of the Perdew-Burke-Ernzerhof (PBE) exchange-correlation functional [26] and a reparametrized Grimme empirical dispersion correction known as D2 [27]. The double prime that appears in the term PBE+D" indicates that the C_6 parameter of Cu has been re-parameterized from its original value of 375 Ry/Bohr^6 to a value of 140 Ry/Bohr^6 [28] in order to reduce the molecule surface overbinding of the original PBE+D2 method [29]–[31]. The Kohn-Sham orbitals were expanded in a plane-wave basis set with a kinetic energy cutoff of 30 Ry (240 Ry for the charge density). The core electrons were described with ultrasoft pseudopotentials [32], [33]. The calculations were performed using the PWscf code from the Quantum ESPRESSO distribution [34], [35]. The computational workflows were automated using the PWTK scripting environment [36].

Molecular graphics were produced by the `xcrysden` graphical package [37]. XY plots and histograms were plotted with the `Gnuplot` program [38] and post-processing of figures was done in `Inkscape` [39].

3.1.2 Copper surface

The crystal structure of bulk copper is characterized by a face-centered cubic (fcc) lattice in which each copper atom is surrounded by 12 nearest neighbors. A conventional crystal unit cell of the fcc bulk copper is depicted in Figure 3.1. In order to obtain a Cu(111) surface from the crystal structure of bulk copper, it is necessary to cleave the crystal along the

(111) plane, as illustrated in Figure 3.1. In calculations, the (111) surface is represented by a slab consisting of several (111) layers. Convergence calculations indicate that adsorption energies rapidly converge with slab thickness. Hence, a slab consisting of several layers is sufficient. Here we use a Cu(111) slab consisting of four atomic layers. The Cu(111) surface was chosen due to its stability compared to other copper surfaces [13]. A unit cell of a four-layer Cu(111) slab is shown in Figure 3.1. Larger surfaces can be generated by multiplying the unit cell in the x and y directions resulting in different $(n \times m)$ supercells, where n and m stand for multipliers of a unit cell expansion in the x and y directions, respectively.

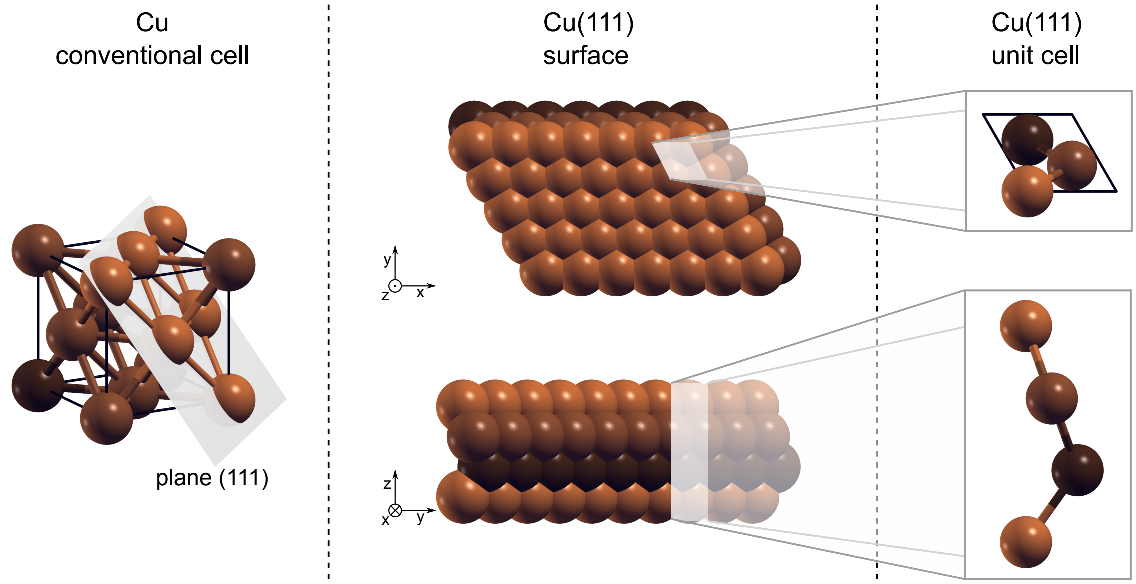

Figure 3.1: Left: the Cu fcc conventional unit cell. Middle: Cu(111) slab consisting of four (111) layers. Right: top- and side-view of the atoms within the unit cell of a four-layer Cu(111) slab.

In our study, Cu(111) was modeled by a periodic multi-slab model consisting of four (111) layers, with the bottom layer constrained to the bulk positions compatible with the calculated equilibrium bulk lattice parameter of Cu of 3.65 Å [40], as shown in Figure 3.2. All other degrees of freedom were relaxed. Adsorbates were adsorbed on the top side of the slab. The thickness of the vacuum region—the distance from the upper Cu layer of the reference slab to the bottom layer of the slab above it—was set to about 25.5 Å, and a dipole correction of Bengtsson [41] was applied approximately in the middle of the vacuum region. The dipole correction serves to eliminate an induced electric field that arises perpendicular to the surface of a slab as a consequence of the periodic boundary conditions imposed on the electrostatic potential. Adsorption calculations were performed with supercells of different sizes ranging from (2×2) to (6×6). Brillouin-zone integrations were performed with the special-point technique [42] using the Methfessel–Paxton smearing [43] of 0.03 Ry. Shifted $\frac{12}{n} \times \frac{12}{m} \times 1$ k-point meshes were used for the $(n \times m)$ super cells, where n and m range from 2 to 6; for the (5×5) supercell the $3 \times 3 \times 1$ k-point mesh was used. Spin polarization was considered for isolated atoms and radicals.

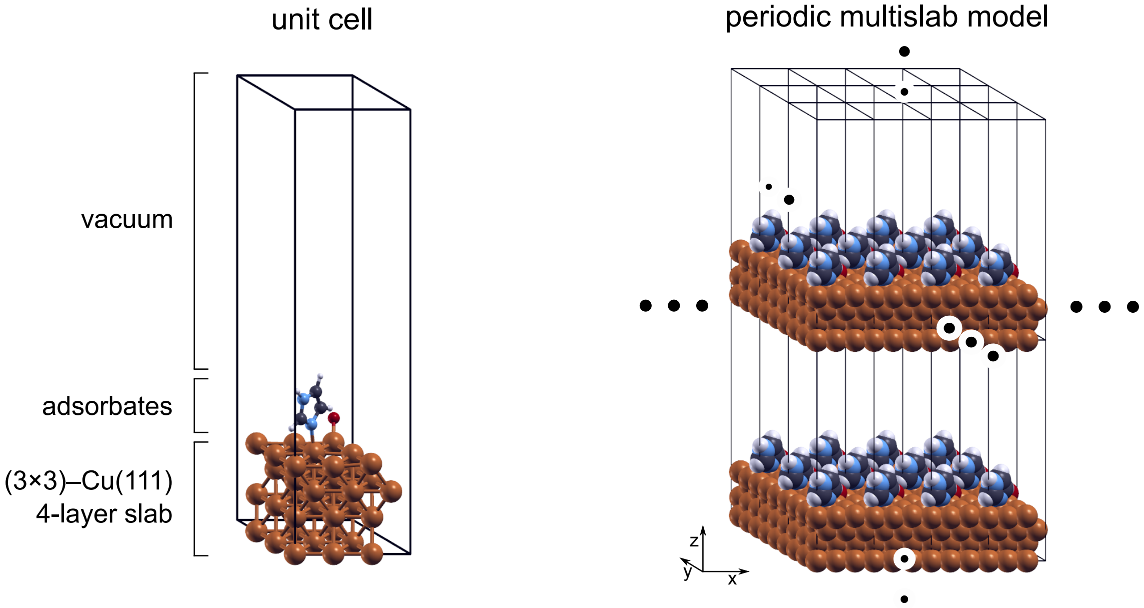

Figure 3.2: A slab model of Cu(111) used in this work. On the left, one unit cell is drawn, consisting of the four-layer Cu(111) slab, adsorbed species, and a vacuum region. On the right, periodic multi-slab model is shown that describes the surface with 3D periodic-boundary conditions.

3.1.3 Definitions of labels

The MolH label is used as a generic label to indicate a neutral molecule throughout the thesis. For inhibitor molecules, uniform abbreviated names are utilized. For example, ImiH, and BTAH labels are used for imidazole and benzotriazole molecules, respectively. Mol (note that H is omitted) is used as a generic label to indicate a deprotonated molecule.

The label X is used as a generic label to designate the H, O, OH, or Cl species. The Cu(111) surface covered with a given X species is labeled as X/Cu(111), whereas a molecule adsorbed on X/Cu(111) is labeled as MolH @ X/Cu(111) (read as: molecule adsorbed at copper(111) surface covered with X coadsorbate).

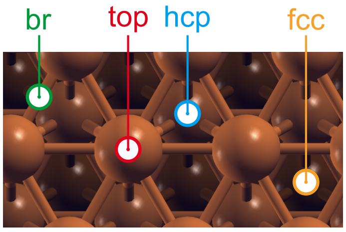

Figure 3.3: Schematic presentation of high-symmetry adsorption sites and their labels: face-centered cubic (fcc) and hexagonal-closed packed (hcp) three-fold hollow sites, bridge (br), and top sites.

Adsorbed X species are labeled as $X_{(ads)}$. To indicate to which adsorption site $X_{(ads)}$ is adsorbed to, the X_{fcc}, X_{hcp}, X_{br}, and X_{top} labels are used, where the subscripts fcc and hcp pertain to the face-centered-cubic and hexagonal-close-packed three-fold hollow sites, respectively, while the subscripts br and top correspond to the bridge and top sites. The fcc, hcp, bridge, and top adsorption sites are depicted in Figure 3.3.

3.1.4 Surface coverage

The surface coverage (Θ) is expressed in monolayer (ML) units, defined as the inverse of the number of surface Cu atoms per adsorbate; for example, if the $(n \times n)$ super cell contains one adsorbed molecule, then the corresponding molecular coverage is $1/n^2$ ML.

3.1.5 Modes of adsorption

Both non-dissociative and dissociative adsorption of azole molecules is considered. In non-dissociative adsorption, none of the molecular bonds are broken during adsorption, whereas dissociative adsorption involves bond breaking after a molecule interacts with a surface.

3.1.6 Energy equations

The molecular adsorption binding energy (E_b) was calculated as:

$$E_\mathrm{b} = E_\mathrm{A/surf} - (E_\mathrm{surf} + E_\mathrm{A}), \tag{3.1}$$

where A stands for the adsorbate (either MolH, H, O, OH, or Cl) and $E_\mathrm{A/surf}$ is the total energy of adsorbate/surface system, E_surf is the total energy of the bare slab, and E_A is the total energy of the isolated adsorbate, where H, O, OH, and Cl were treated as spin-polarized.

To address how $\mathrm{H_{(ads)}}$, $\mathrm{O_{(ads)}}$, $\mathrm{OH_{(ads)}}$, or $\mathrm{Cl_{(ads)}}$ affect the non-dissociative adsorption binding energy, we defined ΔE_b as:

$$\Delta E_\mathrm{b} = E'_\mathrm{b} - E_\mathrm{b}, \tag{3.2}$$

where E_b is the binding energy of a molecule on bare Cu(111), calculated with Eq. (3.1), and E'_b is the binding energy of a molecule on X/Cu(111) surface, calculated as:

$$E'_\mathrm{b} = E_\mathrm{MolH/X/surf} - (E_\mathrm{X/surf} + E_\mathrm{MolH}), \tag{3.3}$$

where $E_\mathrm{MolH/X/surf}$, $E_\mathrm{MolH/surf}$ and E_MolH are total energies of MolH @ X/Cu(111) coadsorption system, X/Cu(111) system, and isolated inhibitor molecule, respectively.

The adsorption energies (E_ads) of X species were calculated with respect to isolated stable molecular species. For X = H, O, or Cl, the adsorption energies were calculated for the $\mathrm{X_2}$ molecule according to the reaction:

$$\mathrm{Cu(111)} + \tfrac{1}{2}\mathrm{X_2} \rightarrow \mathrm{X/Cu(111)}, \tag{3.4}$$

whereas for X = OH, the adsorption energy was calculated with respect to the water molecule according to the reaction:

$$\mathrm{Cu(111)} + \mathrm{H_2O} \rightarrow \mathrm{OH/Cu(111)} + \tfrac{1}{2}\mathrm{H_2}. \tag{3.5}$$

In contrast, for the non-dissociative adsorption of imidazole and benzotriazole molecule, its adsorption energy is given by the binding energy E_b of Eq. (3.1), which corresponds to the reaction:

$$\mathrm{Cu(111)} + \mathrm{MolH} \rightarrow \mathrm{MolH/Cu(111)}. \tag{3.6}$$

Reactions (3.4)–(3.6) imply that the adsorption energies were calculated as:

$$\text{for H, O, Cl:}\quad E_{\text{ads}} = E_{\text{X/surf}} - E_{\text{surf}} - \frac{1}{2}E_{\text{X}_2}, \tag{3.7}$$

$$\text{for OH:}\quad E_{\text{ads}} = E_{\text{OH/surf}} + \frac{1}{2}E_{\text{H}_2} - E_{\text{surf}} - E_{\text{H}_2\text{O}}, \tag{3.8}$$

$$\text{for MolH:}\quad E_{\text{ads}} = E_{\text{MolH/surf}} - E_{\text{surf}} - E_{\text{MolH}}. \tag{3.9}$$

The comparison of Eqs. (3.7)–(3.9) with Eq. (3.1) reveals that E_{b} and E_{ads} are related to each other by a constant that is specific to each adsorbate. The calculated values of these constants are:

$$\text{for H:}\quad E_{\text{ads}} = E_{\text{b}} + 2.25\ \text{eV}, \tag{3.10}$$

$$\text{for O:}\quad E_{\text{ads}} = E_{\text{b}} + 2.85\ \text{eV}, \tag{3.11}$$

$$\text{for OH:}\quad E_{\text{ads}} = E_{\text{b}} + 3.01\ \text{eV}, \tag{3.12}$$

$$\text{for Cl:}\quad E_{\text{ads}} = E_{\text{b}} + 1.42\ \text{eV}, \tag{3.13}$$

$$\text{for MolH:}\quad E_{\text{ads}} = E_{\text{b}}. \tag{3.14}$$

A change of energy as a system goes from one state (say, state A) to another state (state B) is denoted by a generic label ΔE and is calculated as:

$$\Delta E = E_{\text{B}} - E_{\text{A}}, \tag{3.15}$$

where E_{A} and E_{B} are the total energies of states A and B, respectively.

Molecular adsorption energies are calculated with respect to an isolated MolH molecule in a vacuum. Depending on the substrate, the adsorption energy of non-dissociative adsorption is equivalent to either E'_{b} or E_{b}, i.e.:

$$E_{\text{ads}} = E_{\text{MolH/surf}} - (E_{\text{surf}} + E_{\text{MolH}}), \tag{3.16}$$

where "surf" stands for either X/Cu(111) or bare Cu(111). For deprotonated molecules, adsorption energy is calculated as:

$$E_{\text{ads}}^{\text{diss}} = E_{\text{(Mol+H)/surf}} - (E_{\text{surf}} + E_{\text{MolH}}), \tag{3.17}$$

where $E_{\text{(Mol+H)/surf}}$ is the total energy of an adsorption system with H and deprotonated Mol coadsorbed on the surface; the superscript "diss" in $E_{\text{ads}}^{\text{diss}}$ indicates "dissociative" adsorption.

3.1.7 Electronic structure analysis

The electron charge density difference, $\Delta\rho(\mathbf{r})$, was used to characterize chemical bonds between the adsorbed species and the surface as well as lateral interactions between the inhibitor molecule and the coadsorbed X species. Charge density difference was calculated as:

$$\Delta\rho(\mathbf{r}) = \rho_{\text{A/surf}}(\mathbf{r}) - \rho_{\text{A}}(\mathbf{r}) - \rho_{\text{surf}}(\mathbf{r}), \tag{3.18}$$

where the subscripts have the same meaning as defined above. Geometries of the standalone systems (A and surf) were kept consistent with that of the A/surf adsorption system. For MolH @ X/Cu(111) coadsorption systems, electron charge densities were calculated as:

$$\Delta\rho(\mathbf{r}) = \rho_{\text{MolH/X/surf}}(\mathbf{r}) - \rho_{\text{MolH}}(\mathbf{r}) - \rho_{\text{X/surf}}(\mathbf{r}). \tag{3.19}$$

A planar integrated electron charge density difference was calculated as:

$$\Delta\rho(z) = \int_A \Delta\rho(x,y,z)\ \mathrm{d}x\ \mathrm{d}y, \tag{3.20}$$

where the integration runs over the area A spanned by the surface supercell, z is the surface normal direction, and $\Delta\rho(x,y,z) \equiv \Delta\rho(\mathbf{r})$. The first-moment function of $\Delta\rho(z)$ was calculated as:

$$\mu(z) = \int_{-a}^{z} z'\Delta\rho(z')\ \mathrm{d}z', \tag{3.21}$$

where $-a$ is the z-component of the specific point in vacuum beneath the slab, such that $\Delta\rho(-a) = 0$. The first-moment function $\mu(z)$ is related to the surface normal-component of the adsorption-induced dipole moment $\mu_\perp$ because for the models utilized herein—with adsorbates adsorbed only on one side of the slabs—$\mu_\perp$ can be calculated as:

$$\mu_\perp = \int_{-a}^{C-a} z\Delta\rho(z)\ \mathrm{d}z, \tag{3.22}$$

where C is the size of the supercell along the z-direction. Note that both $-a$ and $C-a$ are located in vacuum, such that $\Delta\rho(-a) = \Delta\rho(C-a) = 0$.

The surface normal-component of the adsorption-induced dipole moment is related to the adsorption-induced work-function change ($\Delta\Phi$) via the Helmholtz relation (in atomic Hartree units):

$$\Delta\Phi = 4\pi\theta e_0\mu_\perp \tag{3.23}$$

where $\mu_\perp$ is expressed in e Bohr unit, θ is the adsorbate coverage (in Bohr^{-2}), and e_0 stands for the elementary charge ($e_0 = 1$ e). Note that among currently considered $\mathrm{X_{(ads)}}$, only OH possesses a permanent molecular dipole and to capture it by $\mu_\perp$, the respective $\Delta\rho(z)$ was calculated as:

$$\Delta\rho(z) = \rho_{\mathrm{OH/surf}}(z) - \rho_{\mathrm{O}}(z) - \rho_{\mathrm{H}}(z) - \rho_{\mathrm{surf}}(z). \tag{3.24}$$

The adsorption induced work-function change can be obtained from Eq. (3.23) that in turn utilizes Eqs. (3.19)–(3.22). While these equations are very useful for a detailed analysis, they are cumbersome for routine calculation of $\Delta\Phi$ because they require additional post-processing calculations. For the models utilized herein, with adsorbates adsorbed only on one side of the slabs, $\Delta\Phi$ can be straightforwardly obtained from the PWscf output provided that the dipole correction was used. In this case, $\mu_\perp$ of Eq. (3.23) is opposite to the self-consistently determined dipole of the counteracting dipole layer utilized in the dipole correction.

3.1.8 Bader charge analysis

Bader charges were calculated using the `Bader` code [44], [45] by generating charge densities with the projector-augmented-wave (PAW) potentials [46], [47] and 1000 Ry kinetic energy cutoff for the charge density, using single-point calculations of structures relaxed with ultrasoft pseudopotentials.

3.2 Calculations of Hydrated Coordination Complexes

Technical details for performing calculations of coordination complexes in aqueous phase is outlined in this section. A cluster/continuum approach was utilized, combining explicitly treated water molecules in the first solvation shell and an implicit aqueous solvent model to describe the surrounding water. A method for evaluating the thermodynamic stability of complexes is also briefly described.

3.2.1 Computational details

DFT calculations in vacuum and in aqueous phase were performed with the hybrid MN15 energy functional [48] using `Gaussian16` program package [49]. All atoms were described by the all-electron Def2TZVP basis set of Ahlirichs [50]. An SMD continuous solvation model [51] was used to describe the aqueous solvent implicitly. `GoodVibes` program [52] was used to calculate the correction to standard Gibbs energies. To this end, the quasi-harmonic approximation of the Cramer-Truhlar method [53] was employed. This involved increasing the vibrational frequencies below 100 cm^{-1} to 100 cm^{-1} to compensate for the inaccuracy of the harmonic oscillator model for low-frequency vibrational modes. Similar to adsorption calculations, the `xcrysden` graphical package [37] was used to produce molecular graphics. 2D plots were plotted with `Gnuplot` [38] and post-processing of figures was done in `Inkscape` [39].

3.2.2 N-heterocyclic ligands

Herein, 19 N-heterocyclic compounds shown in Figure 3.4 were studied for their ability to form coordinative complexes with Cu(I), or Cu(II) ions.

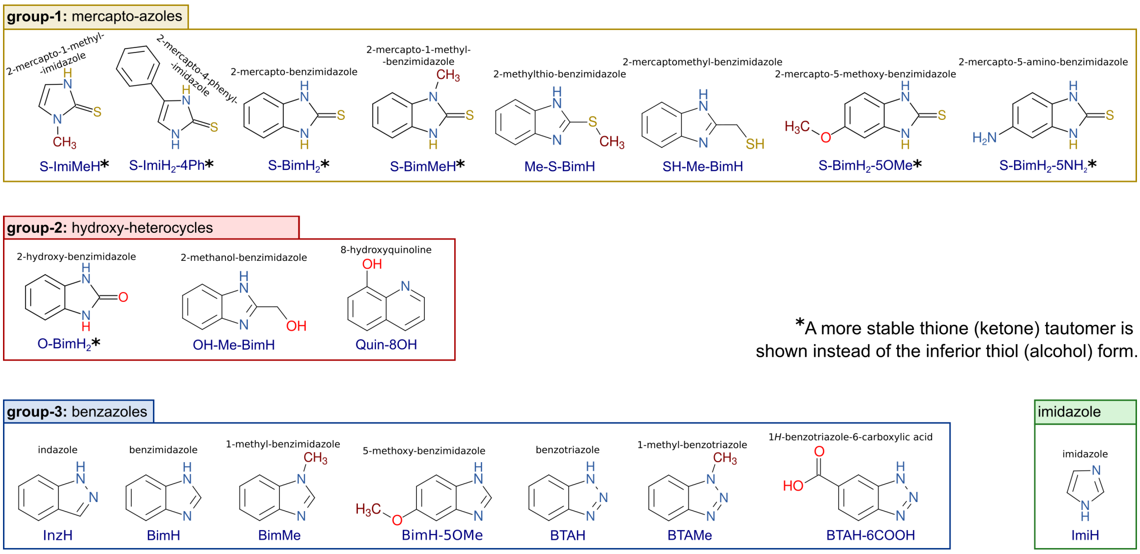

*A more stable thione (ketone) tautomer is shown instead of the inferior thiol (alcohol) form.

Figure 3.4: 19 N-heterocyclic organic molecules and their labels used to study the coordination complexes with Cu(I) and Cu(II). These molecules are taken from the dataset of Kokalj et al. [54]. All but one of them (Quin-8OH) belong to the azole family. Molecules are divided into four groups: (1) eight molecules having an SH functional group (mercapto-azoles)—among them, six molecules (marked with *) tautomerize from thiol to thione; (2) three molecules with an OH functional group (hydroxy-heterocycles)—among them one molecule (marked with *) predominantly exist is the ketone instead of the alcohol form; (3) seven benzazoles, and (4) imidazole.

All molecules, except 8-hydroxyquinoline, belong to the azole group—five-membered heterocyclic aromatic compounds containing a nitrogen atom and at least one other heteroatom as part of the ring. Each molecule has its own abbreviation label according to Figure 3.4. For the purpose of simplicity, a generic label L is used to designate an N-heterocyclic ligand, regardless of its net charge.

Seven of the considered molecules in Figure 3.4 marked with an asterisk (*) are subject to either thiol–thione or alcohol–ketone tautomerization as shown in Figure 3.5. In such a case, a more stable thione (ketone) is shown in Figure 3.4 and was used in calculations instead of its inferior thiol (alcohol) tautomer.

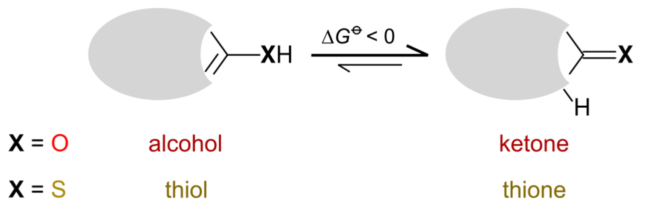

Figure 3.5: Molecules containing a hydroxyl (mercapto) group near an sp^2-hybridized C atom are subject to tautomerization. In aqueous solution, solvated thiones are about 0.5 eV more stable than thiols, as indicated by the calculated $\Delta G^{\ominus}$ [54], which is the difference between the standard Gibbs energies of both isomeric forms. Similarly, for hydroxy-heterocycles, the O-BimH$_2$ ketone is around 0.6 eV more stable than the OH-BimH alcohol [54]. This particular instance of keto-enol tautomerism is known as lactam-lactim tautomerism. In lactam-lactim interconversion, hydrogen migrates between the oxygen and nitrogen atoms. In this thesis, lactam-lactim tautomerization is referred to as ketone-alcohol tautomerization because the latter term is more widely known.

pK_a values and speciation distribution charts gathered in Appendix A were estimated with atomic charge method developed by Dixon and Jurs [55] as implemented in the `MavinSketch` program. Based on the speciation distribution charts, ligands were considered in the speciation form that is the stablest at pH 7. Therefore, 18 molecules were treated as neutral ligands, while 1H-benzotriazole-6-carboxylic acid (BTAH-6COOH) was considered in its deprotonated carboxylate form (BTAH-6COO$^-$).

Most of the investigated molecules have at least one electron-rich atom (N, O, or S) that can participate in the dative (coordinate) bond with the central copper ion. There are two molecules that can also act as bidentate ligands (Quin-8OH and BTAH-6COO$^-$), where a ligand forms two dative bonds with the central ion.

3.2.3 Energy equations

The reaction energy for the formation (E_form) of a coordination complex between ligands and copper ion can be calculated as:

$$E_\mathrm{form} = E(\mathrm{complex}) - E(\mathrm{copper\ ion}) - \sum_{i=1}^{N} E_i(\mathrm{ligand}), \tag{3.25}$$

where $E(\mathrm{complex})$ corresponds to the total energy of a coordination complex, $E(\mathrm{copper\ ion})$ is the total energy of either a Cu(I) or Cu(II) ion, $E_i(\mathrm{ligand})$ is the total energy of an i-th ligand, and N is the number of ligands.

The energy of the studied system at a specified temperature T can be expressed as:

$$E(T) = E_0 + E_\mathrm{trv}(T), \tag{3.26}$$

where E_0 is the Kohn-Sham energy computed at 0 K without considering the Zero Point Energy (ZPE). $E_\mathrm{trv}(T)$ stands for the combined thermal energy of translation, rotation, and vibration at temperature T, including the ZPE. ZPE corresponds to $E_\mathrm{trv}(0)$, where translational and rotational internal thermal energies are zero and vibration energy equals to ZPE. Calculating E_0 is much easier and demands fewer computational resources compared to calculating the vibrational frequencies of a system. Hence, the energy can be calculated on two levels of rigor – either as E_0 at 0 K without ZPE, which is widely used and less demanding, or as $E(T)$, which incorporates the ZPE and demands more computational power. Once the vibrational frequencies are obtained, determining standard Gibbs energy at a given temperature T is straightforward:

$$G^{1\text{atm},(\text{g}),T} = E_0 + E_{\text{trv}}(T) + k_{\text{B}}T - TS_{\text{trv}}(T, 1\text{atm}), \tag{3.27}$$

where all contributions to the energy and entropy of a system at a given temperature T can be calculated using the respective statistical-mechanic equations [56] as implemented in the `Gaussian 16`, and `GoodVibes` program package.

The standard reaction Gibbs energy for the formation of a coordination complex in aqueous medium was calculated using a thermodynamic cycle as proposed by Bryantsev et al. [57]. All contributions to the standard Gibbs energy for a given solvated species (S), and water molecule are shown in Figure 3.6. This combines gas-phase calculations and implicit solvent calculations to obtain the Gibbs energy of solvation at a given concentration and temperature. The implicit solvent calculations have a convenient feature because, due to their parametrization, the Gibbs energy of solvation can be straightforwardly calculated as a difference between energies in the solvent and vacuum:

$$G_{\text{solv}} = E_0^{(\text{aq})} - E_0^{(\text{g})}, \tag{3.28}$$

where $E_0^{(\text{aq})}$ represents the total energy at 0 K of the relaxed system in the aqueous phase and $E_0^{(\text{g})}$ is the total energy of the relaxed system in vacuum at 0 K, which is assumed to be equivalent to the gas-phase.

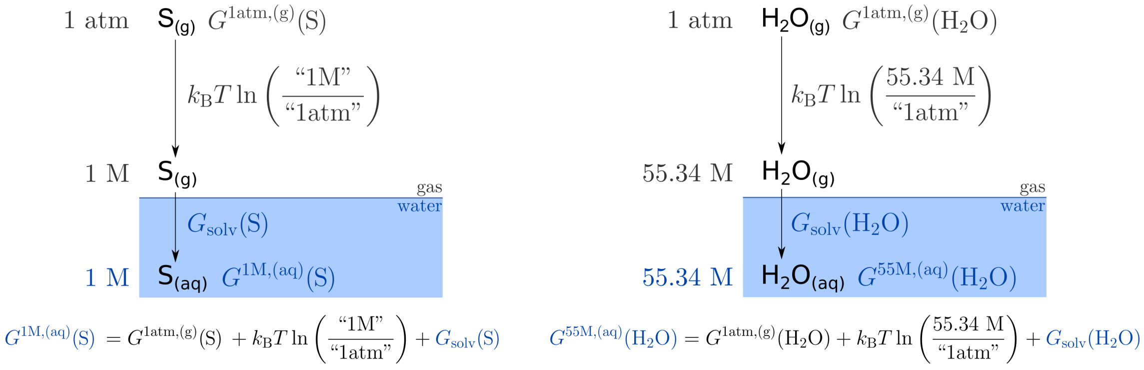

Figure 3.6: Schematic representation of all contributions to the Gibbs energy for considered non-water species S [left] and water molecule [right].

Taking into account all contributions to the standard Gibbs energy for solvated species (S) as depicted in Figure 3.6, the standard Gibbs energy at 1 M concentration, $G^{1\text{M},(\text{aq})}(\text{S})$, can be calculated using the following expression:

$$G^{1\text{M},(\text{aq})}(\text{S}) = G^{1\text{atm},(\text{g})}(\text{S}) + k_{\text{B}}T\ln\left(\frac{\text{“1M”}}{\text{“1atm”}}\right) + G_{\text{solv}}(\text{S}), \tag{3.29}$$

where a standard state concentration of 1 M was chosen for species solvated in the aqueous medium, and partial pressure of 1 atm represents a standard state in the gas phase. The labels "1M" and "1atm" are symbolic representations of the respective concentrations, which at 298.15 K correspond to:

$$\text{“1M”} \Rightarrow 1\ \text{M}, \tag{3.30}$$

$$\text{“1atm”} \Rightarrow 1\ \text{atm} \equiv 0.04088\ \text{M}. \tag{3.31}$$

A self-solvation of a water molecule requires special treatment as the concentration of liquid water at 298.15 K is 55.34 M. The Gibbs energy of liquid water at this conditions can thus be written as:

$$G^{55\text{M},(\text{aq})}(\text{H}_2\text{O}) = G^{1\text{atm},(\text{g})}(\text{H}_2\text{O}) + k_\text{B}T \ln\left(\frac{55.34\ \text{M}}{\text{“1atm"}}\right) + G_\text{solv}(\text{H}_2\text{O}). \tag{3.32}$$

A general expression for calculating standard Gibbs energy of a reaction can be written as:

$$\Delta G^\ominus = \sum_i^{\text{products}} \upsilon_i G_i^\ominus - \sum_j^{\text{reactants}} \upsilon_j G_j^\ominus , \tag{3.33}$$

where the first term is a sum of all standard Gibbs energies of products ($G_i^\ominus$) multiplied by the corresponding stoichiometric υ_i coefficient, and the second term represents a sum of all standard Gibbs energies of reactants ($G_j^\ominus$) by taking into account the stoichiometric coefficients υ_j.

According to the experimental results of hydrated Cu(I) and Cu(II) ions, Cu(I) usually binds with two ligands in a linear geometry, whereas Cu(II) usually binds with four ligands in a square-planar geometry [58] with ligands like water and other molecules. Hence, the thermodynamics of the formation of coordination complexes with Cu(I) was treated using the following two elementary steps:

$$\begin{aligned}
[\text{Cu(H}_2\text{O)}_2]^{1+} + \text{L} &\xrightarrow{\Delta G_1^\ominus} [\text{Cu(H}_2\text{O)(L)}]^{1+} + \text{H}_2\text{O} \\
[\text{Cu(H}_2\text{O)(L)}]^{1+} + \text{L} &\xrightarrow{\Delta G_2^\ominus} [\text{Cu(L)}_2]^{1+} + \text{H}_2\text{O},
\end{aligned}$$

where one water ligand is substituted with one monodentate L ligand per elementary reaction step. Similarly can be written also for the hydrated Cu(II) ion, which forms 4-coordinated complexes:

$$\begin{aligned}
[\text{Cu(H}_2\text{O)}_4]^{2+} + \text{L} &\xrightarrow{\Delta G_1^\ominus} [\text{Cu(H}_2\text{O)}_3\text{(L)}]^{2+} + \text{H}_2\text{O} \\
[\text{Cu(H}_2\text{O)}_3\text{(L)}]^{2+} + \text{L} &\xrightarrow{\Delta G_2^\ominus} [\text{Cu(H}_2\text{O)}_2\text{(L)}_2]^{2+} + \text{H}_2\text{O} \\
[\text{Cu(H}_2\text{O)}_2\text{(L)}_2]^{2+} + \text{L} &\xrightarrow{\Delta G_3^\ominus} [\text{Cu(H}_2\text{O)(L)}_3]^{2+} + \text{H}_2\text{O} \\
[\text{Cu(H}_2\text{O)(L)}_3]^{2+} + \text{L} &\xrightarrow{\Delta G_4^\ominus} [\text{Cu(L)}_4]^{2+} + \text{H}_2\text{O}.
\end{aligned}$$

In depicted reactions, in total up to four water ligands can be substituted with L ligands. Standard reaction Gibbs energy ($\Delta G^\ominus$) for each reaction step can be calculated using a general expression for calculating standard reaction Gibbs energy from Eq. 3.33. Note that in this case all stoichiometric coefficients are equal to one.

A general reaction of water molecule substitution from hydrated copper ion with neutral molecular ligands (L) can be written as follows:

$$[\mathrm{Cu(H_2O)}_n(\mathrm{L})_m]^{x+}_{(\mathrm{aq})} + k\mathrm{L}_{(\mathrm{aq})} \rightarrow [\mathrm{Cu(H_2O)}_{n-k}(\mathrm{L})_{m+k}]^{x+}_{(\mathrm{aq})} + k\mathrm{H_2O}_{(\mathrm{aq})}, \tag{3.34}$$

where coefficients n and m correspond to a number of water molecules and ligands L in the reactant complex, respectively, and k is a number of substituted water molecules.

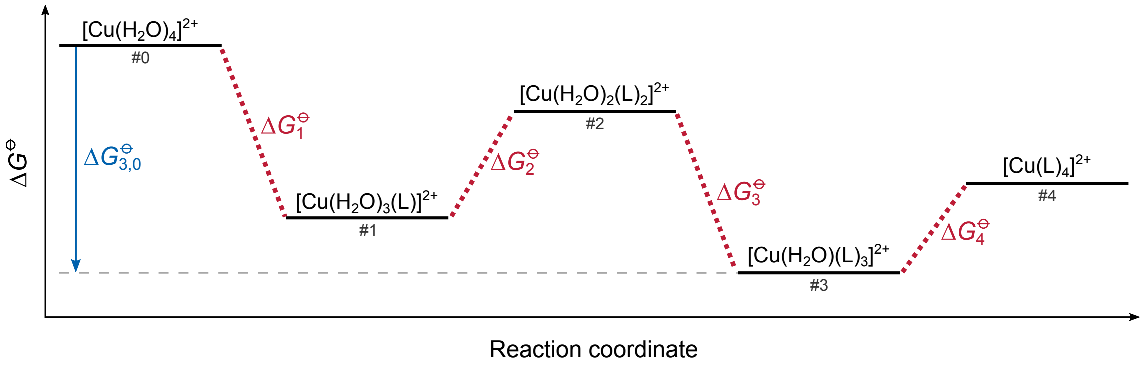

Figure 3.7: Schematic representation of the formation of $[\mathrm{Cu(L)_4}]^{2+}$ from $[\mathrm{Cu(H_2O)_4}]^{2+}$. All considered elementary reaction steps are shown.

A schematic representation of a reaction profile for the formation of $[\mathrm{Cu(L)_4}]^{2+}$ is shown in Figure 3.7. $\Delta G^\ominus$ for each reaction step can be calculated using the Eq. 3.33. $\Delta G^\ominus_{\mathrm{to,from}}$ describes standard Gibbs energy of reaction steps needed to get from a complex containing m L ligands, to a complex containing $m + k$ L ligands.

$$\Delta G^\ominus_{\mathrm{to,from}} \equiv \Delta G^\ominus_{m+k,m} \tag{3.35}$$

Generally, $\Delta G^\ominus$ for the formation of a specific L-containing complex from a hydrated copper ion ($m = 0$) is represented by $\Delta G^\ominus_{k,0}$.

Chapter 4

Adsorption Calculations

The results obtained within the scope of adsorption calculations will be presented and discussed hereinafter. Two sections are included in this chapter. In the first section, the effect of chemisorbed H, O, OH, and Cl on the adsorption of imidazole on Cu(111) is scrutinized by means of systematic DFT calculations, where the role of coverage, a type of the coadsorbed $X_{(ads)}$ species, and the distance between imidazole and $X_{(ads)}$ are addressed [59]. While in the second section, we concentrate primarily on deprotonation of imidazole and benzotriazole induced by $O_{(ads)}$ and $OH_{(ads)}$ [60].

4.1 Effect of Coadsorbed Species on Imidazole Adsorption

In this section, we discuss how investigated coadsorbed species—H, O, OH, and Cl (henceforth referred to as $X_{(ads)}$) affect the adsorption bonding of imidazole on Cu(111). First, standalone adsorption of investigated species is briefly described. Then, the impacts of coverage, the kind of $X_{(ads)}$ species, and the distance between imidazole and $X_{(ads)}$ were investigated using a comprehensive high-throughput DFT study including over 400 distinct adsorption configurations. The explanation of effects coadsorbed species have on the adsorption of imidazole was published in an article pertaining to this thesis, entitled *How adsorbed H, O, OH, and Cl affect plain adsorption of imidazole on copper* [59].

4.1.1 Adsorption on bare Cu(111)

Imidazole prefers to adsorb on a top site of Cu(111) by forming the N–Cu bond with its N3 atom [24], [61], [62] (Figure 4.1). Among the possible orientations of imidazole around the N–Cu bond (i.e., the "helicopter" orientation), the staggered orientation is predicted to be marginally more stable than the eclipsed one by 0.01 eV (for the two orientations, see Figure 4.1). In the smallest (2×2) supercell considered, only the staggered orientation is viable because molecules avoid each other more effectively in this orientation.

H, O, OH, and Cl species prefer to adsorb onto three-fold hollow sites (Table 4.1). Among the two hollow sites, the fcc hollow site is marginally preferred over the hcp site, except for O, for which the difference is somewhat greater (about 0.1 eV).

The dependence of adsorption energy on the coverage of H, O, OH, and Cl species and imidazole molecule on bare Cu(111) is shown in Figure 4.2, where supercells ranging from (2×2) to (6×6) are considered, corresponding to coverages ranging from 1/4 to 1/36 ML, respectively. Only the most stable sites (top site for imidazole and fcc site for the X species) are taken into account, with the exception of OH, for which the less stable bridge site is also considered because, in some cases, OH_{fcc} shifts to OH_{br} upon imidazole adsorption. While the adsorption energy of imidazole exhibits a strong dependence on the coverage (the

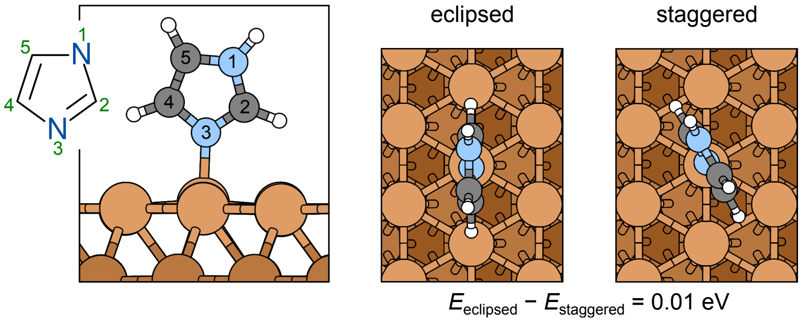

Figure 4.1: Imidazole adsorbed on Cu(111) is depicted in top- and side-views, along with its skeletal structure and atom numbering. Staggered and eclipsed "helicopter" orientations of imidazole are considered. In the eclipsed orientation, the molecular plane is aligned such that the C2–H and C4–H bonds point to the neighboring Cu atoms, whereas in the staggered orientation, they point toward bridge sites in between the neighboring Cu atoms. The staggered orientation is marginally more stable (by 0.01 eV).

binding energy becomes more exothermic by about 0.3 eV as coverage decreases from 1/4 to 1/36 ML), the adsorption energies of X species are relatively insensitive to the coverage, with the exception of OH_{fcc} at 1/4 ML, where E_{ads} is by 0.1 eV more endothermic than at lower coverages.

Table 4.1: Adsorption binding energies (E_b) and adsorbate heights (d) for H, O, OH, and Cl at high-symmetry adsorption sites on (2 × 2)–Cu(111). The reported d values correspond to the z-coordinate difference between the adsorbate and the average height of the Cu atoms to which the adsorbate binds; for diatomic OH, the z-coordinate of the O atom is taken. There are some high-symmetry adsorption sites that are not local minima, and for some of them, the values were obtained with constrained relaxation.

	E_b (eV)				d (Å)			
	fcc	hcp	bridge	top	fcc	hcp	bridge	top
H	−2.50	−2.49	−2.35	−1.87	0.91	0.93	1.06	1.53
O	−4.50	−4.39	-4.00^a	−2.71	1.12	1.13	1.22^a	1.76
OH	−2.98	−2.95	−2.87	−2.41	1.38	1.40	1.51	1.88
Cl	−3.39	−3.38	−3.30	−3.00	1.87	1.88	1.93	2.19

[a] Calculated with the constrained relaxation.

The reason the adsorption energy of imidazole and, to a lesser extent, of OH_{fcc} depends on the coverage can be attributed to lateral dipole–dipole interactions. Due to its strong permanent dipole moment, imidazole exhibits long-range lateral dipolar interactions [61].[1] A similar argument can also explain the slightly weaker adsorption of OH_{fcc} at the high coverage of 1/4 ML. For example, among the adsorbed X species, OH_{fcc} exhibits the largest adsorption-induced change of the work function (Figure 4.3) and, consequently, the largest surface-normal component of the dipole. Additionally, it protrudes from the surface more than the other X species. Therefore, its dipolar interactions are less sceened by the metal than those of the other adsorbates which are located closer to the surface.

Figure 4.3 reveals that $O_{(ads)}$ and $Cl_{(ads)}$ increase the work function, $H_{(ads)}$ has almost no effect on it, and $OH_{(ads)}$ decreases the work function. The figure demonstrates that the

---

[1] The DFT calculated value of dipole moment of imidazole is 3.8 D [61], [63].

adsorption-induced change of the work function is linearly proportional to the adsorbate coverage, a trend expected from the Helmholtz Eq. (3.23). Typically, the adsorption-induced increase in work function is related to the negative charge of adsorbates positioned above the surface.

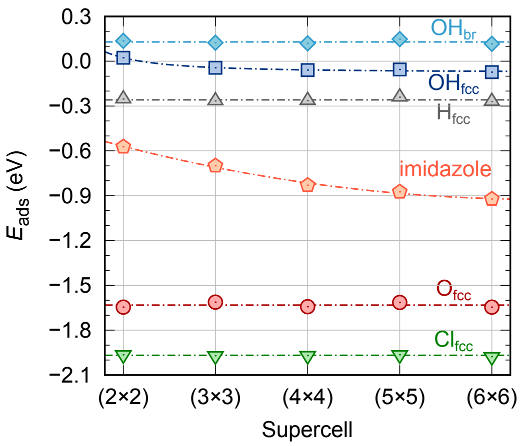

Figure 4.2: Adsorption energies (E_{ads}) for considered species on Cu(111) as a function of the $(n \times n)$ supercell size, corresponding to the adsorbate coverage of $1/n^2$ ML.

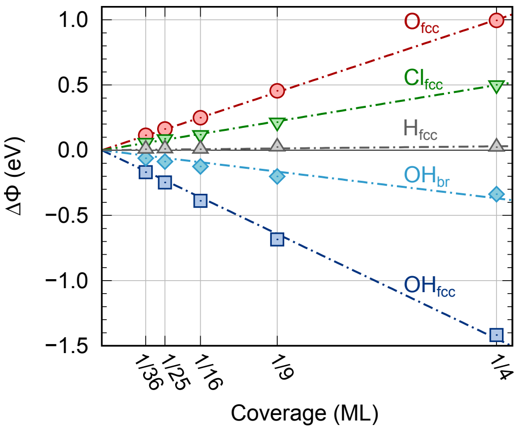

Figure 4.3: Adsorption induced work-function change ($\Delta\Phi$) of chemisorbed H_{fcc}, O_{fcc}, OH_{fcc}, OH_{br}, and Cl_{fcc} on Cu(111) as a function of the adsorbate coverage.

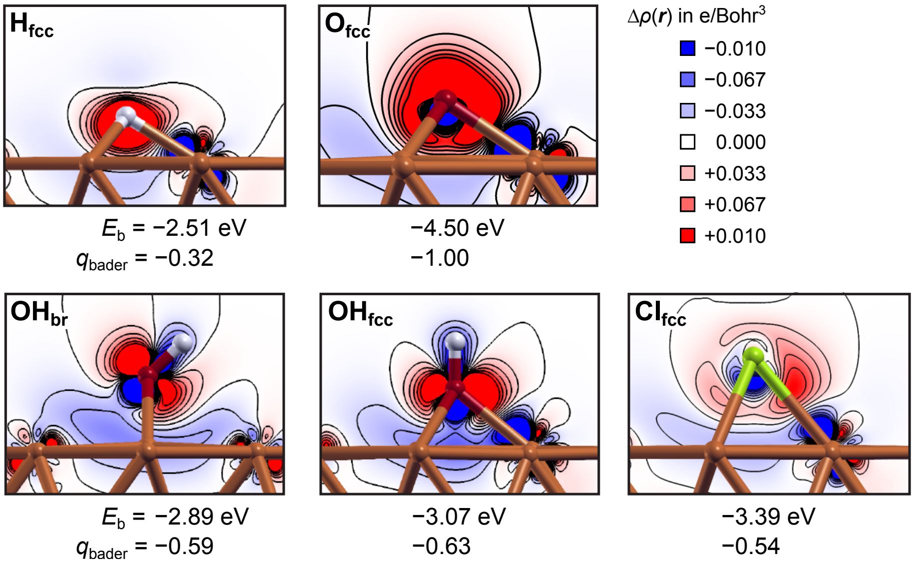

Figure 4.4: Electron charge density difference, $\Delta\rho(\mathbf{r})$ of Eq. (3.18), for H_{fcc}, O_{fcc}, OH_{br}, OH_{fcc}, and Cl_{fcc} on (4×4)–Cu(111). Eleven contours are drawn in a linear scale from -0.01 to $+0.01$ e/Bohr^3 with the increment of 0.002 e/Bohr^3. Electron excess regions are colored red and electron deficit regions are blue (i.e., electrons flow from blue to red regions). The corresponding binding energies and adsorbate Bader charges are also listed (negative values correspond to negatively charged adsorbates).

The plots of electron charge density difference of the X/Cu(111) systems depicted in Figure 4.4 display that all X adsorbates are negatively charged. This qualitative observation is compatible with the calculated Bader charges summarized in the same figure. It is worth noting that $H_{(ads)}$ is negatively charged, which is in stark contrast with cases where H adsorbs to an O atom at oxide surfaces (thus forming an OH group) and is proton-like. The reason that $H_{(ads)}$ has a negligible effect on the work function of Cu(111), despite its negative charge, can be related to its low height above the surface and a slight depletion of electron charge, seen in Figure 4.4 as a very faint bluish region located above the prominent red charge accumulation zone.

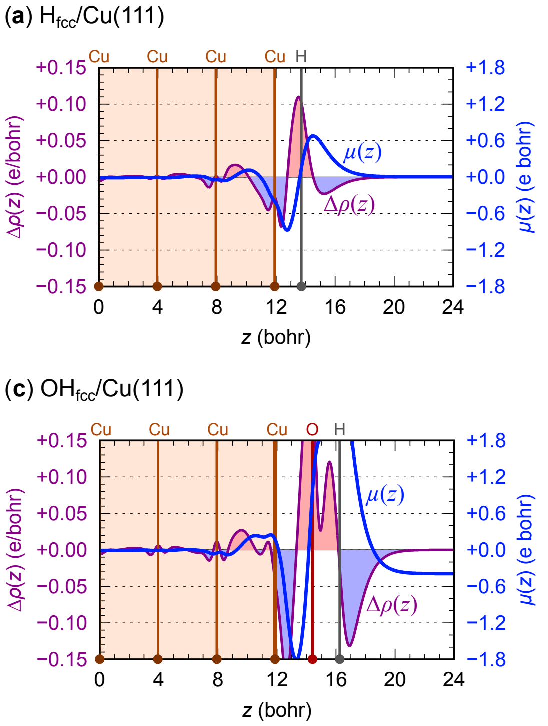

Figure 4.5: Planar integrated electron charge density difference $\Delta\rho(z)$ (purple curve), defined by Eq. (3.20), and the first moment function $\mu(z)$ (blue curve), defined by Eq. (3.21), for H_{fcc}, O_{fcc}, and OH_{fcc} on (4×4)–Cu(111). Note that $\Delta\rho(z)$ of OH_{fcc} was calculated as $\Delta\rho(z) = \rho_{OH/surf}(z) - [\rho_O(z) + \rho_H(z) + \rho_{surf}(z)]$. $\rho_O(z) + \rho_H(z)$ was employed rather than $\rho_{OH}(z)$ in order to capture also a permanent dipole of OH. The z positions of the Cu layers and adsorbate atoms are indicated by vertical lines. The value of $\mu(z)$ on the right side of the plot corresponds to the surface-normal component of the adsorbate dipole moment $\mu_\perp$ (i.e., adsorption-induced for H_{fcc} and O_{fcc} and permanent + adsorption-induced for OH_{fcc}).

The planar integrated charge density difference, $\Delta\rho(z)$ shown in Figure 4.5a, reveals electron charge depletion above the adsorbate considerably more clearly. Without this depletion, the negatively charged $H_{(ads)}$ atom would increase the work function as shown by the corresponding analysis of $\Delta\rho(z)$ and its first-moment function $\mu(z)$ in Figure 4.5a. For $O_{(ads)}$, this charge depletion is essentially absent (Figure 4.5b), and, correspondingly reflects in $O_{(ads)}$ induced increase of the work function. Similarly, the decrease of the work-function induced by $OH_{(ads)}$ can be attributed to its positively charged, outward-pointing H atom (Figure 4.5c). OH_{fcc} has a greater effect on the work function compared to OH_{br} because its polar O–H bond points normal to the surface, whereas for OH_{br}, the O–H bond is tilted (cf. Figure 4.4).

4.1.2 Adsorption of imidazole on X/Cu(111)

In this section, the effect of the coadsorbed X species on the adsorption of imidazole is characterized. As demonstrated above, imidazole prefers to adsorb on a top site, whereas X species prefer adsorption on an fcc site (see Table 4.1). Therefore, we considered the adsorption of imidazole on a top site with one X species pre-adsorbed onto an fcc hollow site per $(n \times n)$ supercell, with n ranging from 2 to 6. While on bare Cu(111), all top adsorption sites are equivalent, for $\mathrm{X_{fcc}}$/Cu(111), the number of symmetry inequivalent top sites increases with the supercell size. To make the symmetry of the $(n \times n)$–$\mathrm{X_{fcc}}$/Cu(111) systems more evident, Figure 4.6 shows them as colored hexagons, where the symmetry inequivalent top sites are color-coded.

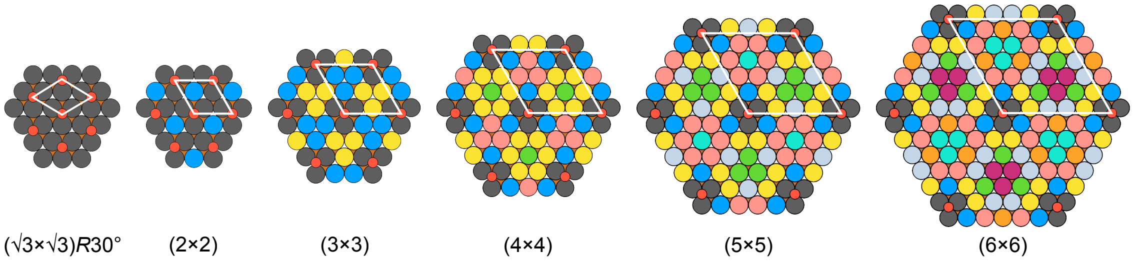

Figure 4.6: Schematic presentation of inequivalent top adsorption sites for the $(\sqrt{3} \times \sqrt{3})R30°$ and $(n \times n)$ $\mathrm{X_{fcc}}$/Cu(111) systems, with n ranging from 2 to 6. Reference supercells are indicated by white parallelograms. The coverage of $\mathrm{X_{(ads)}}$ is 1/3 ML for $(\sqrt{3} \times \sqrt{3})R30°$ and $1/n^2$ ML for $(n \times n)$ supercells. Small reddish balls represent the $\mathrm{X_{fcc}}$ adsorbates, whereas larger balls are the Cu atoms. Cu atoms (i.e., top adsorption sites) that are related by symmetry are colored with the same color.

For such systems, we found that the number of symmetry inequivalent top sites (N_ineq) can be expressed as follows [59]:

$$N_\mathrm{ineq} = n + \sum_{i=1}^{n} \mathrm{int}\left(\frac{i-1}{3}\right), \tag{4.1}$$

where n corresponds to the $(n \times n)$ supercell and $\mathrm{int}(j/k)$ is the integer division of j by k. Equation 4.1 was numerically validated by Kokalj up to the (1000×1000) supercell, which is sufficient for all practical purposes [59]. The dependence of the number of symmetry inequivalent top sites on the supercell size is presented graphically in Figure 4.7, whereas Figure 4.8 schematically plots the lateral distance from the position of the central fcc site to a given top site for all the inequivalent sites up to the largest considered (6×6) supercell.

At each supercell dimension, many of different adsorption geometries were considered in order to scrutinize the effect of adsorbed X species (X = H, O, OH, or Cl) on imidazole adsorption on Cu(111). The configurational search included all inequivalent top adsorption sites for each supercell evaluated. Different orientations of imidazole were probed at each site (note from Figure 4.1 that the difference between staggered and eclipsed "helicopter" orientation of imidazole is only 0.01 eV, indicating that the presence of $\mathrm{X_{(ads)}}$ can easily alter the orientation). Approximately 400 distinct adsorption configurations were considered (snapshots of all considered configurations for (4×4)–Cu(111) are gathered in Appendix B). The corresponding results are presented in Figure 4.9, where the effect of coadsorbed X species on the adsorption of imidazole is measured using ΔE_b of Eq. (3.2). To facilitate

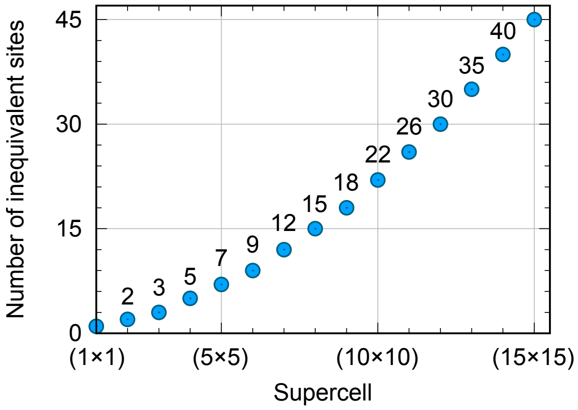

Figure 4.7: Number of symmetry inequivalent top sites for the $(n \times n)$–X_{fcc}/Cu(111) systems as a function of the supercell size (cf. Eq. (4.1)). Adapted from ref. [59].

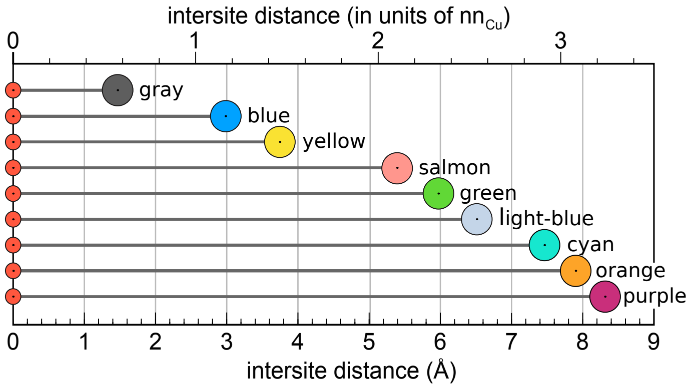

Figure 4.8: Schematic presentation of the lateral inter-site distance between the position of the central fcc site (small reddish balls) and a given top site (larger balls, colored according to Figure 4.6) for all the inequivalent top sites up the largest considered (6×6) supercell. The top abscissa axis represents the inter-site distance in units of the Cu–Cu nearest-neighbor distance (nn_{Cu}). The names of the color sites are also explicitly stated.

discussion, this effect is referred to as the X coadsorption effect, and the top adsorption sites are indicated by the colors defined in Figure 4.6.

In Figure 4.9, systems consisting only of one adsorbed imidazole molecule and one adsorbed X species per $(n \times n)$–Cu(111) supercell are considered. The most stable orientations of imidazole at different top sites of X/Cu(111) up to the green site are shown in Figure 4.10. For sites beyond the green site, different helicopter orientations of imidazole display similar stability due to the long distance between $X_{(ads)}$ and imidazole. Results depicted in Figure 4.9 reveal that the X coadsorption effect depends on the type and the coverage of the X species as well as the distance between the adsorbed imidazole and $X_{(ads)}$. On the nearest adsorption site (grey site), $H_{(ads)}$ destabilizes imidazole adsorption by 0.14 eV (not shown in Figure 4.9), whereas the other considered $X_{(ads)}$ species prevent the adsorption of imidazole thereon, which is not surprising because these sites are too close to the adsorbed X species, i.e., they are only 1.5 Å laterally away from the fcc site to which the X species is adsorbed. Even for $H_{(ads)}$, there is a strong tendency to avoid imidazole adsorption at the grey site by displacing either imidazole or $H_{(ads)}$ to a neighboring site to increase the distance between the two coadsorbates. Grey sites are therefore

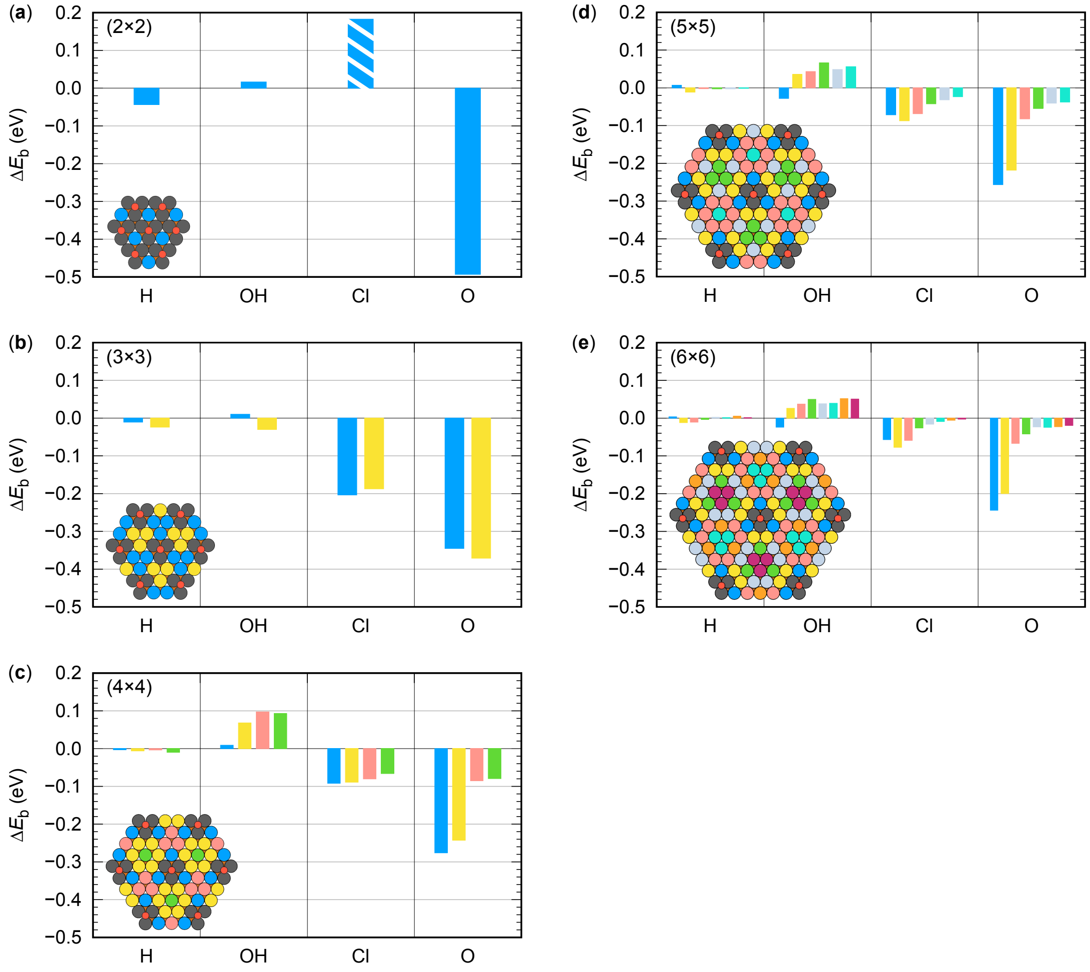

Figure 4.9: The effect of adsorbed H, OH, Cl, or O species on the adsorption of imidazole on Cu(111) as measured by ΔE_b of Eq. (3.2). Histograms represent the ΔE_b values of the most stable identified systems for each considered case. Bars are colored according to the top-site color coding of Figure 4.6. The blue bar corresponding to (2×2)–Cl/Cu(111) is stripped because in this case imidazole does not adsorb via N–Cu bonding (see Figure 4.11).

not considered in Figure 4.9 (note that the smallest $(\sqrt{3} \times \sqrt{3})R30^\circ$ supercell shown in Figure 4.6 consists of only grey sites, hence it is not considered in Figure 4.9).

Based on the size of the X species and the imidazole molecule, a simple analysis shows that surface sites can be classified into three regions based on the lateral inter-site distance:

(i) Pauli repulsion region, consisting of the nearest-neighbor grey sites, where imidazole cannot adsorb for X = O, OH, and Cl.[2]

(ii) Local region, consisting of blue and yellow sites, where H-bonds between the X species and imidazole are possible.

(iii) Distant region, consisting of the remaining sites. These sites are too far for the formation of X$\cdots$imidazole H-bonds (more than 5.3 Å away from the fcc site, Figure 4.8).

---

[2] At the $X_\mathrm{(ads)}$ coverage of at least 1/3 ML—as exemplified by the $(\sqrt{3} \times \sqrt{3})R30^\circ$ structure—only grey sites exist (Figure 4.6). This implies that at so high $X_\mathrm{(ads)}$ coverage, imidazole cannot adsorb for X = O, OH, and Cl. It will be shown later that imidazole can adsorb on Cu(111) covered with 1/3 ML or even 1/2 ML of $O_\mathrm{(ads)}$ if some O adatoms displace from fcc to hcp sites and thus make some top sites non-grey.

The ΔE_b results of Figure 4.9 indicate that among the considered X species, $O_{(ads)}$ displays the largest effect on the adsorption of imidazole, meaning it enhances the adsorption binding of imidazole ($\Delta E_\mathrm{b} < 0$). $Cl_{(ads)}$ also enhances the adsorption of imidazole (except at high coverage of 1/4 ML corresponding to (2×2)–Cl_fcc overlayer) but to a lesser extent than $O_{(ads)}$. Imidazole adsorption is not significantly affected by $H_{(ads)}$, whereas $OH_{(ads)}$ tends to diminish its adsorption strength.

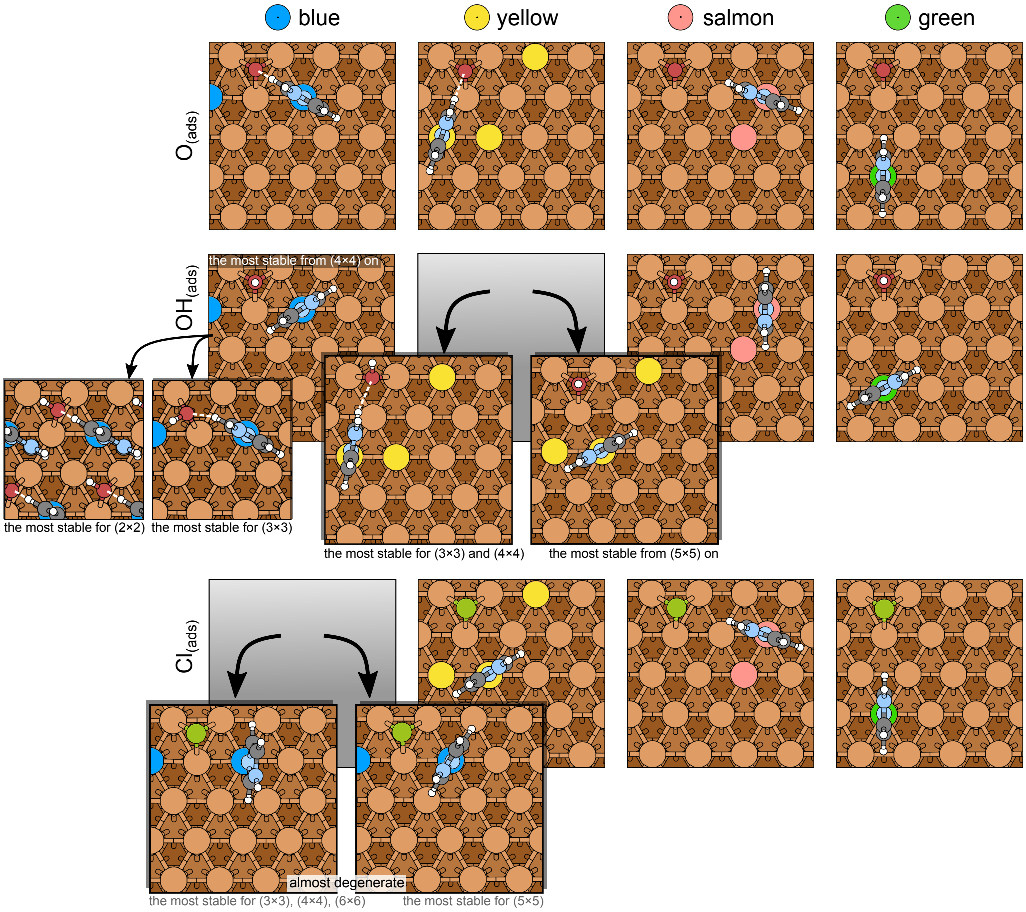

Figure 4.10: Top-view snapshots of the most stable identified structures of imidazole adsorbed (from left to right) on blue, yellow, salmon, and green top sites (from top to bottom) on O/Cu(111), OH/Cu(111), and Cl/Cu(111). In each column, the considered top sites are colored according to the designated hue. In some instances, the most stable structure varies depending on the size of the supercell, and in those instances, all stable forms are depicted.

At low $X_{(ads)}$ coverage, imidazole prefers to adsorb near $X_{(ads)}$ to either blue or yellow site, regardless of whether $X_{(ads)}$ enhances or diminishes the adsorption binding of imidazole, except in the case of $H_{(ads)}$, where imidazole binds very similarly to all non-grey sites, since $H_{(ads)}$ has almost no effect on the adsorption of imidazole. In general, irrespective of the adsorption site, the coadsorption effect of $X_{(ads)}$ diminishes as the $X_{(ads)}$ coverage increases. The sole exceptions are the (2×2)–OH and (3×3)–OH overlayers, which affect the adsorption binding energy of imidazole to a lesser extent than the lower coverage OH configurations. Our following discussion scrutinizes in greater detail the coadsorption effects of $O_{(ads)}$, $Cl_{(ads)}$, and $OH_{(ads)}$, whereas $H_{(ads)}$ is excluded from further discussion since it does not significantly affect imidazole adsorption.

4.1.2.1 Coadsorption effect of $O_{(ads)}$

Among the considered X species, $O_{(ads)}$ shows the strongest and most stabilizing effect on imidazole adsorption. Due to the formation of an H-bond between imidazole and $O_{(ads)}$, the stabilizing effect is particularly strong for the nearby yellow and blue sites (*vide infra*). When comparing all cases considered in Figure 4.9, stabilizing effect is the largest at the high coverage of 1/4 ML, corresponding to the (2 × 2) supercell, where the binding of imidazole is enhanced by about 0.5 eV, whereas at low $O_{(ads)}$ coverages the stabilization decreases to about 0.25 eV.

Experiments have also demonstrated that $O_{(ads)}$ can stabilize azole adsorption. In particular, Cho et al. [64] have shown with STM that on Cu(110) with co-existing phases of clean Cu(110) and oxygen-reconstructed Cu(110)–(2 × 1), benzotriazole preferentially adsorbs on the oxygen-reconstructed phase.

4.1.2.2 Coadsorption effect of $Cl_{(ads)}$

The (2×2)–$Cl_{(ads)}$ overlayer, corresponding to the coverage of 1/4 ML, significantly destabilizes the adsorption of imidazole, whereas at lower considered coverages, the effect changes, and $Cl_{(ads)}$ stabilizes imidazole adsorption, but to a lesser extent than $O_{(ads)}$. The reason (2 × 2)–$Cl_{(ads)}$ overlayer destabilizes adsorption of imidazole is that $Cl_{(ads)}$ is too bulky[3] to allow imidazole to come close to the copper surface (see the top-view snapshot of Figure 4.11a) and, consequently, imidazole is located nearly 4 Å above the surface Cu layer (the corresponding N–Cu distance is about 3.9 Å). The side-view snapshot of this structure (Figure 4.11a) reveals that imidazole adsorbs considerably different than in other lower coverage cases (Figure 4.11b), where it forms a direct N–Cu bond, which is about 2.1 Å long.

As for the lower Cl coverages, where the adsorption of imidazole is stabilized, the nearby sites are only marginally preferred over the distant sites because, in contrast to $O_{(ads)}$, H-bonds between imidazole and $Cl_{(ads)}$ do not form. At the nearby yellow and blue sites, imidazole orients with its H atoms away from $Cl_{(ads)}$ (see the corresponding snapshots in Figure 4.10). The salmon site is the first site where imidazole orients with its C–H bond toward $Cl_{(ads)}$, and the resulting electrostatic interaction is likely the reason that the salmon site is of very similar stability as the blue and yellow sites.

At first glance, the finding that $Cl_{(ads)}$ stabilizes the adsorption of azoles seems to contradict experimental observations that chloride ions displace adsorbed benzotriazole from a copper surface [66]. Using a series of experiments, Yang et al. [66] estimated Gibbs adsorption energies as a function of electrode potential and found that at negative potentials vs. Ag/AgCl the adsorption of benzotriazole is more exergonic than that of Cl^-, whereas at positive potentials the two energies become similar; only at potentials around 0 V vs. Ag/AgCl the adsorption of Cl^- is slightly more exergonic than that of benzotriazole. The reason for Cl^- displacing benzotriazole from the surface can thus be attributed to the concentration of the two species in solution, which is typically higher for chlorides. At a high chloride concentration (0.5 M in Ref. [66]), the tendency for Cl^- adsorption is very strong, hence an optimal saturation structure on Cu(111) is most likely formed, which is the high coverage 1/3 ML $(\sqrt{3} \times \sqrt{3})R30^\circ$–Cl/Cu(111) phase [67], [68]. According to our results, azoles cannot adsorb at such a high Cl coverage, thus corroborating experimental observations [66]; note that already the 1/4 ML (2 × 2)–Cl/Cu(111) structure sterically prevents the adsorption of imidazole (cf. Figure 4.11a).

---

[3] $Cl_{(ads)}$ is the bulkiest among the considered $X_{(ads)}$ species; the ionic radius of Cl^- is 1.81 Å, whereas the ionic radius of O^{2-} ranges from 1.21 to 1.42 Å [65].

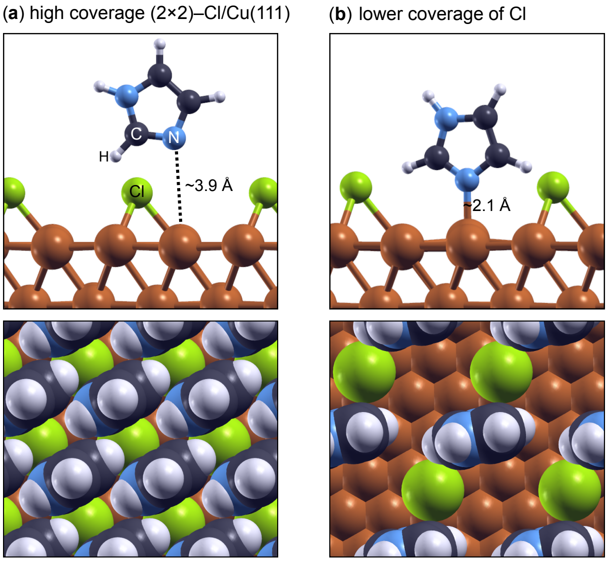

Figure 4.11: Side-view and top-view snapshots of imidazole structures at (a) a high-coverage (2 × 2)–Cl/Cu(111) and (b) a lower 1/9 ML $Cl_{(ads)}$ coverage. In the top-view snapshots, atoms are drawn with the van der Waals radii. The top-view snapshot in (a) reveals that $Cl_{(ads)}$ is too bulky to allow imidazole to come close to the copper surface in the case of the (2 × 2)–$Cl_{(ads)}$ overlayer and, consequently, the N–Cu distance is about 3.9 Å long, whereas at a lower Cl coverage imidazole forms about 2.1 Å long N–Cu bond with the surface.

A beneficial effect of chlorides on the formation of organic film on a copper surface was reported by Kozlica et al. [69] who showed that Cl^- ions act both as a promoter and a reactant for the formation of a polymerized Cu–Cl–mercaptobenzimidazole film[4] that remarkably protects the copper from corrosion, whereas in the absence of chloride ions the the film does not form. Furthermore, as a result of spectroscopic measurements, Kozlica et al. [70] reported that mercaptobenzimidazole does not even adsorb to the surface in the absence of chloride media. While this example is far from the current case of coadsorbed $Cl_{(ads)}$ and imidazole on Cu(111), it shows that chloride ions can act beneficially in specific scenarios.

4.1.2.3 Coadsorption effect of $OH_{(ads)}$

$OH_{(ads)}$ usually diminishes the adsorption binding of imidazole, particularly in the case when distant sites are considered. Only in three cases involving the nearby sites, $OH_{(ads)}$ slightly enhances the adsorption binding of imidazole, i.e., at the yellow site of (3 × 3)–OH as well as at the blue sites of (5 × 5)–OH and (6 × 6)–OH (see Figure 4.9). When imidazole adsorbs on a blue site of (2 × 2)–OH and (3 × 3)–OH as well as on the yellow site of (3 × 3)–OH and (4 × 4)–OH, the OH group displaces from the preferred fcc site to the inferior bridge site as to form CH$\cdots$OH hydrogen bond with imidazole molecule. Note that the H atom of OH must point away from imidazole for the CH$\cdots$OH hydrogen bond to form, which is possible only for tilted OH_{br} and not for perpendicular OH_{fcc}. An interesting observation about the coadsorption effect of $OH_{(ads)}$ is that when the most stable imidazole adsorption site at a given $OH_{(ads)}$ coverage is considered, $OH_{(ads)}$ has a

---

[4] Such a polymerized film formed on copper immersed into 3 wt.% NaCl solution containing 1 mM mixture of mercaptobenzimidazole and octylphosphonic acid in the molar ratio of 9:1.

negligible effect on the adsorption binding energy of imidazole as it affects it to within ±0.03 eV.

4.1.3 Electron charge density difference of ImiH @ X/Cu(111)

As tentatively explained before, one reason that $O_{(ads)}$ considerably enhances the adsorption bonding of imidazole on Cu(111) is the formation of a hydrogen bond between $O_{(ads)}$ and imidazole. Therefore, the binding enhancement induced by $Cl_{(ads)}$ is smaller than that of $O_{(ads)}$ because $Cl_{(ads)}$ does not form such hydrogen bonds. This reasoning is supported by the plots of the electron charge density difference of imidazole on bare and X-covered Cu(111) shown in Figure 4.12.

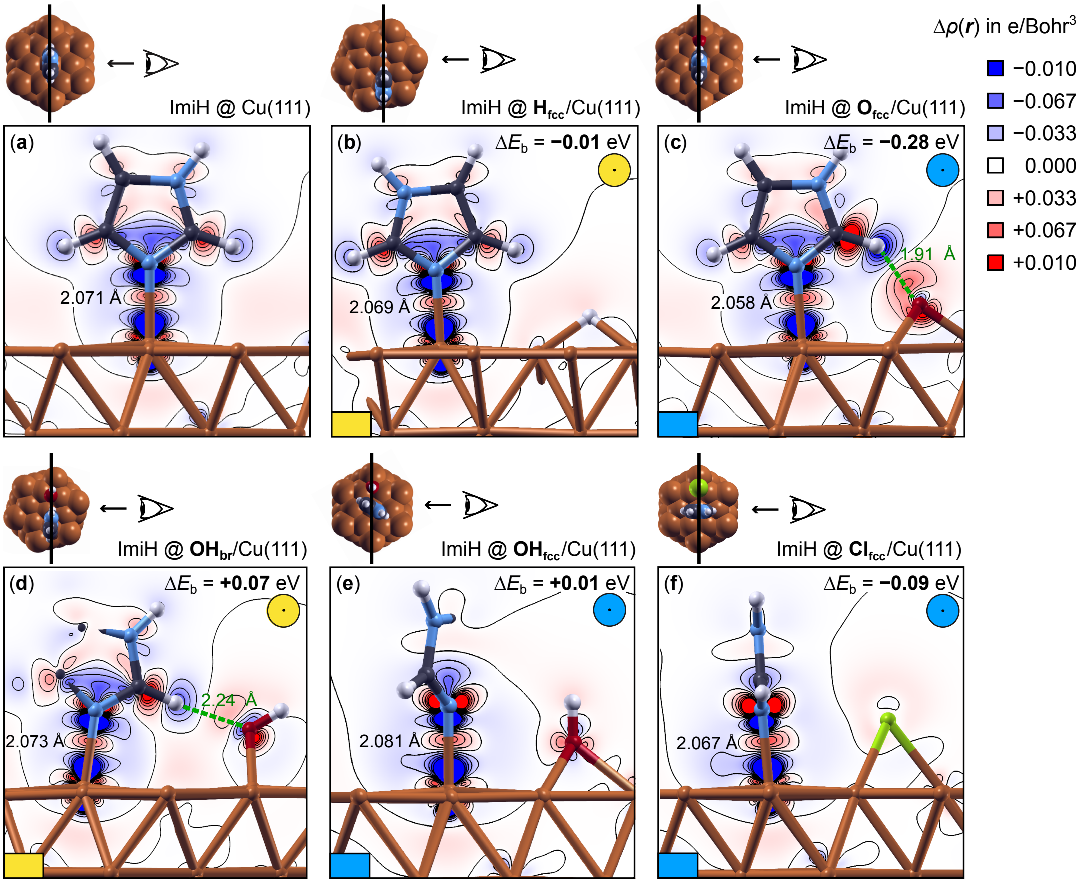

Figure 4.12: Electron charge density difference, $\Delta\rho(\mathbf{r})$ of Eq. (3.19), for imidazole adsorbed either at blue or yellow site on (4×4)–X/Cu(111), X = H, O, OH, or Cl. The $\Delta\rho(\mathbf{r})$ of imidazole on bare (4×4)–Cu(111) is also shown for comparison. Eleven contours are drawn in a linear scale from −0.01 to +0.01 e/Bohr^3 with the increment of 0.002 e/Bohr^3. Electron excess regions are colored red, and electron deficit regions are blue (i.e., electrons flow from blue to red regions). The corresponding ΔE_b values and characteristic bond lengths are also stated. Small hexagonal snapshots above the $\Delta\rho(\mathbf{r})$ plots indicate the positions of the contour planes, whereas the small colored circles at the top-right (also colored rectangles at the bottom-left) of the $\Delta\rho(\mathbf{r})$ plots indicate the type of adsorption site of imidazole.

In all cases, the formation of a direct N–Cu chemical bond is evident by the red electron accumulation lobe in the middle of the N–Cu bond. This is a clear sign of chemisorption

[71]. The figure further reveals that a CH$\cdots$O hydrogen bond forms between imidazole and $O_{(ads)}$. In contrast, such a hydrogen bond is missing in the case of $Cl_{(ads)}$ because at the nearby blue and yellow sites, imidazole orients with its H atoms away from $Cl_{(ads)}$ (see Figure 4.10); the salmon site is the first one where imidazole orients with its C–H bond toward $Cl_{(ads)}$, but the corresponding H$\cdots$Cl distance of 3.6 Å is too long for hydrogen bonding (the lack of hydrogen bonding, in this case, is evident from the $\Delta\rho(\mathbf{r})$ plot shown in the bottom right snapshot in Figure 4.13). Figure 4.12 further reveals that a weak CH$\cdots$O hydrogen bond also forms between imidazole and OH_{br}, whereas in the case of OH_{fcc} such hydrogen bond is missing and imidazole orients with its H atoms away from OH_{fcc}. The formation of such a hydrogen bond is the reason that, in some cases, OH shifts from the fcc to the bridge site, which implies that the cost of displacing OH from the stablest fcc to the inferior bridge site (cf. Table 4.1) is compensated by the formation of the hydrogen bond.

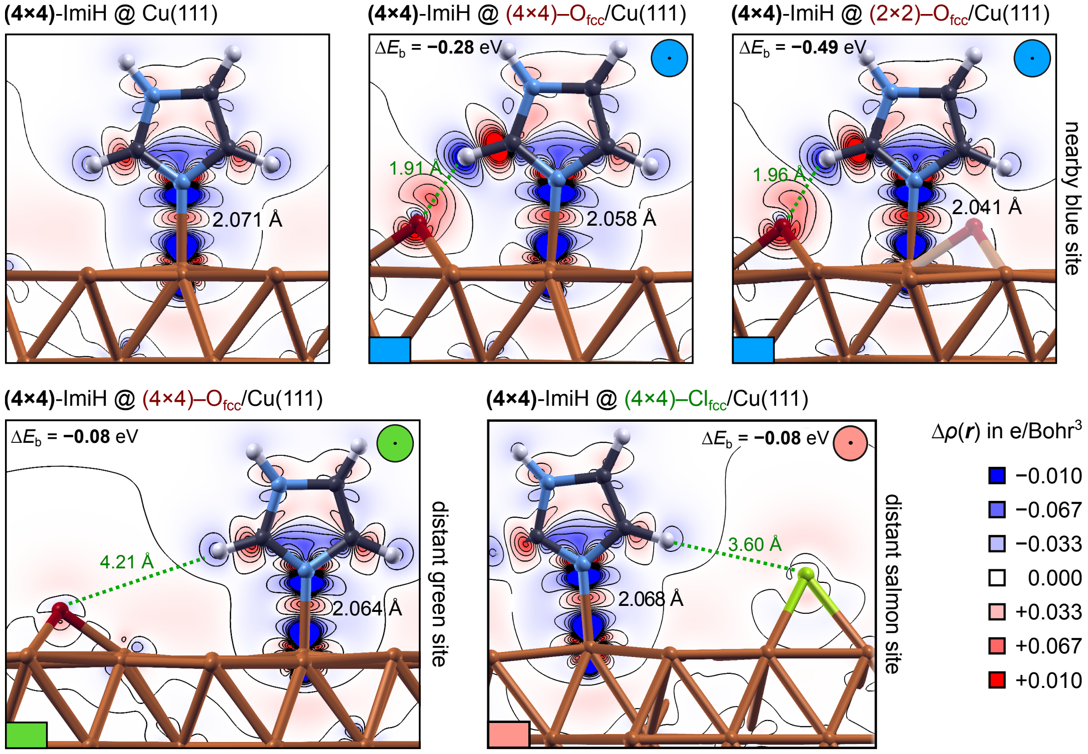

Figure 4.13: Similar to Figure 4.12, but here different $O_{(ads)}$ coverages are considered. Top (from left to right): bare Cu(111), O/Cu(111) with 1/16 ML of $O_{(ads)}$, and O/Cu(111) with 1/4 ML of $O_{(ads)}$. In the top row plots, imidazole is adsorbed at the nearby blue site of O/Cu(111), whereas in the bottom row plot, it is adsorbed on the more distant green site. In all cases, the coverage of imidazole is 1/16 ML, i.e., one imidazole molecule per (4×4)–Cu(111) supercell. The ΔE_b values and the N–Cu bond lengths are also reported. Note that for the blue sites, the electron charge accumulation in the middle of the N–Cu bond increases, and the N–Cu bond length decreases as the coverage of $O_{(ads)}$ increases. In contrast, at the green site (bottom left), this red charge accumulation lobe is very similar to the one on bare Cu(111), although the N–Cu bond is marginally shorter than on the bare Cu(111). Bottom right: Although the C–H bond of imidazole points to $Cl_{(ads)}$, the CH$\cdots$Cl distance of 3.6 Å is too long for H-bonding interactions to occur.

In addition to the hydrogen bond between $O_{(ads)}$ and imidazole, Figure 4.12 shows that the presence of $O_{(ads)}$ and $Cl_{(ads)}$ also strengthens the N–Cu bond as evidenced by the enhanced red electron accumulation lobe in the middle of the N–Cu bond and by the shortened N–Cu bond (e.g., compare Figure 4.12a with Figures 4.12c and 4.12f). In contrast, no such enhancement of the charge accumulation is evident in the case of $H_{(ads)}$ and $OH_{(ads)}$. This charge accumulation enhances as the coverage of $O_{(ads)}$ increases and the N–Cu bond concomitantly shortens, as evident from the top row plots of Figure 4.13, where the $O_{(ads)}$ coverages of 0, 1/16, and 1/4 ML are considered, while the coverage of imidazole is held constant at 1/16 ML. Note that this enhancement of charge accumulation is present only at nearby sites but not at the distant green site (see the bottom row plot in Figure 4.13). Hence, not only the coverage but also the distance from $O_{(ads)}$ matters.

4.1.4 Equivalent coverage of imidazole and $X_{(ads)}$

To summarize the contribution of the coadsorbed $X_{(ads)}$ species on the adsorption binding energy of imidazole and the dependence of E_b on the coverage, Figure 4.14 compares the imidazole E_b values of the most stable identified ImiH @ X/Cu(111) structures to those obtained on bare Cu(111) for each considered coverage. Here the data associated with Figure 4.9 are used, hence only ImiH @ X/Cu(111) systems that contain one adsorbed imidazole molecule and one coadsorbed X species per $(n \times n)$–Cu(111) supercell are considered, i.e., the coverage of imidazole and $X_{(ads)}$ is the same. This figure clearly shows that $O_{(ads)}$ (red curve) considerably enhances the adsorption bonding of imidazole, and so does $Cl_{(ads)}$ (green curve), although to a lesser extent and only to the point where there is enough space in between Cl adatoms for imidazole to adsorb unhindered. In contrast, $H_{(ads)}$ and $OH_{(ads)}$ affect the adsorption of imidazole negligibly, which is why the respective E_b values fall within the thick brownish curve (Figure 4.14) that represents the values obtained on bare Cu(111) as well as on H/Cu(111) and OH/Cu(111).

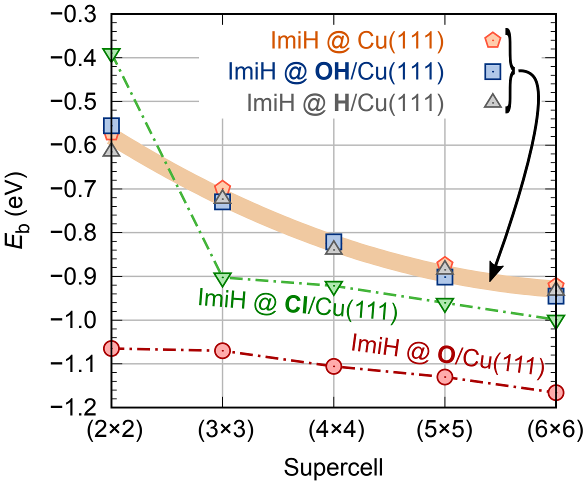

Figure 4.14: The most exothermic binding energies (E_b) of imidazole on bare Cu(111) and Cu(111) covered with the X species (X = H, O, OH, or Cl) as a function of the $(n \times n)$ supercell size. This plot is based on data from Figure 4.9, where structures with one imidazole and one X species per supercell are considered.

4.1.5 Non-equivalent coverage of imidazole and $X_{(ads)}$

Up to this point, the same coverage of $X_{(ads)}$ and imidazole was considered, i.e., one $X_{(ads)}$ species and one imidazole molecule per $(n \times n)$–Cu(111) supercell (the only exception is the rightmost $\Delta\rho(\mathbf{r})$ plot in Figure 4.13) and the results revealed that the magnitude of the coadsorption effect depends on the coverage (for example, the effect of $O_{(ads)}$ is the largest at the highest considered coverage and diminishes as the coverage of $O_{(ads)}$ decreases). However, such a setup does not provide an answer to the question of whether the effect of $X_{(ads)}$ on ΔE_b depends on the coverage of both $X_{(ads)}$ and imidazole or only on the coverage of $X_{(ads)}$. To answer this question, we performed a series of calculations, where the coverage of $O_{(ads)}$ was held constant at 1/4 ML, and the coverage of imidazole was varied from 1/4 ML to 1/36 ML. A similar strategy was also utilized for $Cl_{(ads)}$. The corresponding results, presented in Figure 4.15, reveal that the effect of $X_{(ads)}$ on ΔE_b is largely invariant to the coverage of imidazole—irrespective of the coverage of imidazole, the corresponding values of ΔE_b are -0.50 ± 0.01 eV for (2×2)–O/Cu(111), -0.34 ± 0.02 eV for (2×3)–Cl/Cu(111), and -0.19 ± 0.01 eV for (3×3)–Cl/Cu(111)—although, due to long-range dipolar interactions, the E_b values of imidazole become more exothermic as the coverage of imidazole reduces, e.g., for (2×2)–O/Cu(111) the binding of imidazole strengthens from -1.06 eV at 1/4 ML to -1.43 eV at 1/36 ML of imidazole.

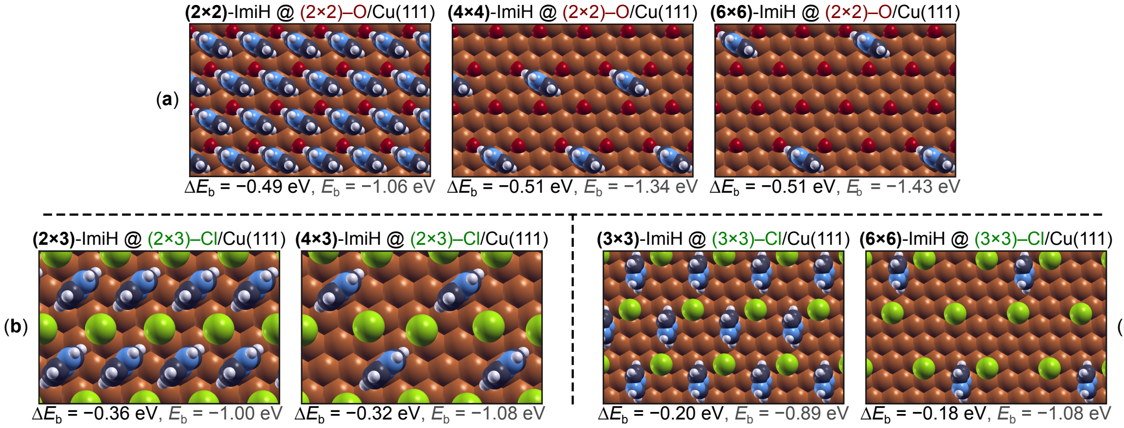

Figure 4.15: Top-view snapshots of imidazole adsorbed on (a) (2×2)–O/Cu(111), (b) (2×3)–Cl/Cu(111), and (c) (3×3)–Cl/Cu(111). In (a) the coverage of imidazole reduces from 1/4 ML (left) to 1/36 ML (right), whereas considered coverages of imidazole in (b) are 1/6 and 1/12 ML and in (c) 1/9 and 1/36 ML. The corresponding ΔE_b and E_b values of imidazole are also stated. Note that for a given $X_{(ads)}$, the ΔE_b values are to some extent invariant on the coverage of imidazole, but they depend on the coverage of $X_{(ads)}$ as evident from the comparison between (b) and (c).

Having established that ΔE_b of imidazole is largely invariant to the coverage of imidazole, we now examine how ΔE_b depends on the coverage of $X_{(ads)}$. To this end, Figure 4.16 summarizes results for $H_{(ads)}$ for imidazole adsorbed at nearest-neighbor grey site on H/Cu(111). The analysis shows that although imidazole can adsorb on grey sites, it is significantly destabilized there compared to other more distant sites or clean Cu(111). The destabilization increases with the $H_{(ads)}$ coverage for $\Theta > 1/3$ ML.

A similar analysis is also performed in Figure 4.17 plots the dependence of ΔE_b of imidazole on the coverage of $O_{(ads)}$ and $Cl_{(ads)}$; here, only the most stable adsorption structures of imidazole are considered, which involve either blue or yellow site for O/Cu(111) and Cl/Cu(111) (cf. Figure 4.9). In addition to the data from Figure 4.9, several other structures are also considered in Figure 4.17, where the coverage of imidazole is lower than the coverage of $X_{(ads)}$ (the top-view snapshots of these extra structures are also shown in Figure 4.17).

It is evident from Figure 4.17 that ΔE_b depends linearly on the coverage of $X_{(ads)}$,

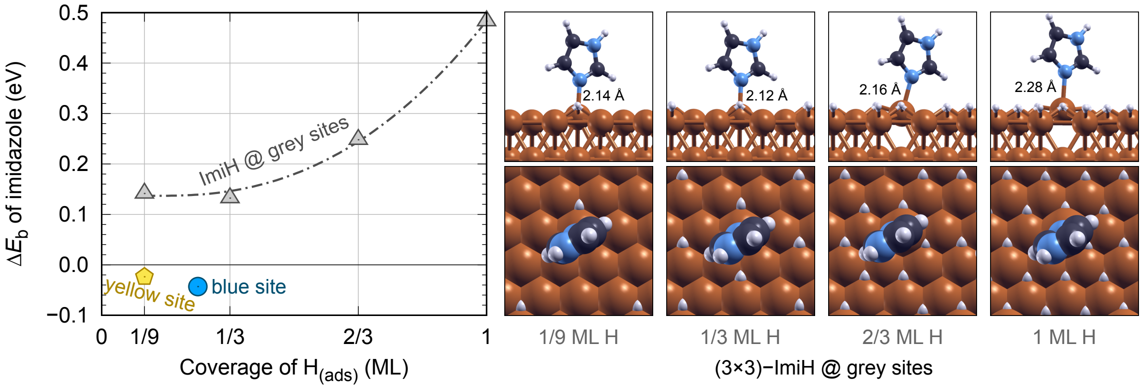

Figure 4.16: Imidazole (ImiH) adsorbed at nearest-neighbor grey site on H/Cu(111) as a function of $H_{(ads)}$ coverage (for the color naming of sites, refer to Figure 4.8). Although imidazole can adsorb at grey top site on H/Cu(111), it is destabilized there compared to other more distant sites or clean Cu(111). The snapshots of imidazole adsorbed at grey sites are shown on the right. The N–Cu bond length ranges from about 2.1 to 2.3 Å and is therefore typical for weak chemisorption.

i.e., the higher is the $X_{(ads)}$ coverage, the stronger is the ΔE_b effect, unless the coverage of $X_{(ads)}$ becomes so high as to hinder or even prevent the adsorption of imidazole due to steric reasons. For $Cl_{(ads)}$, this happens at $\Theta \gtrsim 1/4$ ML (an example of $Cl_{(ads)}$ preventing the chemisorption of imidazole already at $\Theta = 1/4$ ML is shown for (2×2)–Cl/Cu(111) in Figure 4.11a), whereas for $O_{(ads)}$ this happens somewhere in between 1/2 ML and 2/3 ML because our calculations indicate that imidazole cannot chemisorb at 2/3 ML of $O_{(ads)}$, as shown in Figure 4.18. At this coverage, all surface Cu atoms are bonded to two O adatoms, hence all top sites are grey and, consequently, imidazole adsorbs with the N3 atom facing toward the fcc hollow site with the N–Cu distances of about 3.0 Å. Surprisingly, imidazole adsorption is destabilized by only 0.1 eV with respect to clean Cu(111), i.e., $\Delta E_\mathrm{b} = 0.10$ eV.

Figure 4.17 reveals that $O_{(ads)}$ and $Cl_{(ads)}$ stabilize adsorption of imidazole up to 0.77 and 0.35 eV, respectively. There is, however, a remarkable difference between $O_{(ads)}$ and $Cl_{(ads)}$. While Cl prefers to form the high-coverage 1/3 ML $(\sqrt{3} \times \sqrt{3})R30°$–Cl/Cu(111) structure [67], [68] that, according to our results, blocks the chemisorption of imidazole, the 1/3 ML phase of $O_{(ads)}$ instead enhances the adsorption of imidazole.[5] The calculated low coverage adsorption energy of imidazole on clean Cu(111) is about −0.9 eV (Figure 4.2), hence the optimum binding energy of imidazole on O/Cu(111) can be estimated to be about −1.6 eV, which is very similar to the adsorption energy of imidazole on coordinatively unsaturated Cu site of $Cu_2O(111)$ [19], [20], [28], [74].

As explained before by means of the $\Delta\rho(\mathbf{r})$ analysis (Figure 4.12), the $O_{(ads)}$ strengthens the adsorption of imidazole due to the CH$\cdots$O hydrogen bond and due to the $O_{(ads)}$ induced strengthening of the N–Cu bond (we refer to these two effects as the "local effects"). It is obvious that hydrogen bonding is a local effect because an H-bond between imidazole and $O_{(ads)}$ forms only if imidazole is adsorbed close enough to $O_{(ads)}$. Furthermore, the strengthening of the N–Cu bond also appears to be a local effect because the $\Delta\rho(\mathbf{r})$ analysis of Figure 4.13 reveals that at the distant green site, this effect is not evident anymore. If these two effects were the only ones induced by $X_{(ads)}$, then it would be hard to understand

---

[5] Otherwise, oxygen prefers thermodynamically to form either surface or bulk cuprous oxides [72], [73], which should also be able to adsorb imidazole [19].

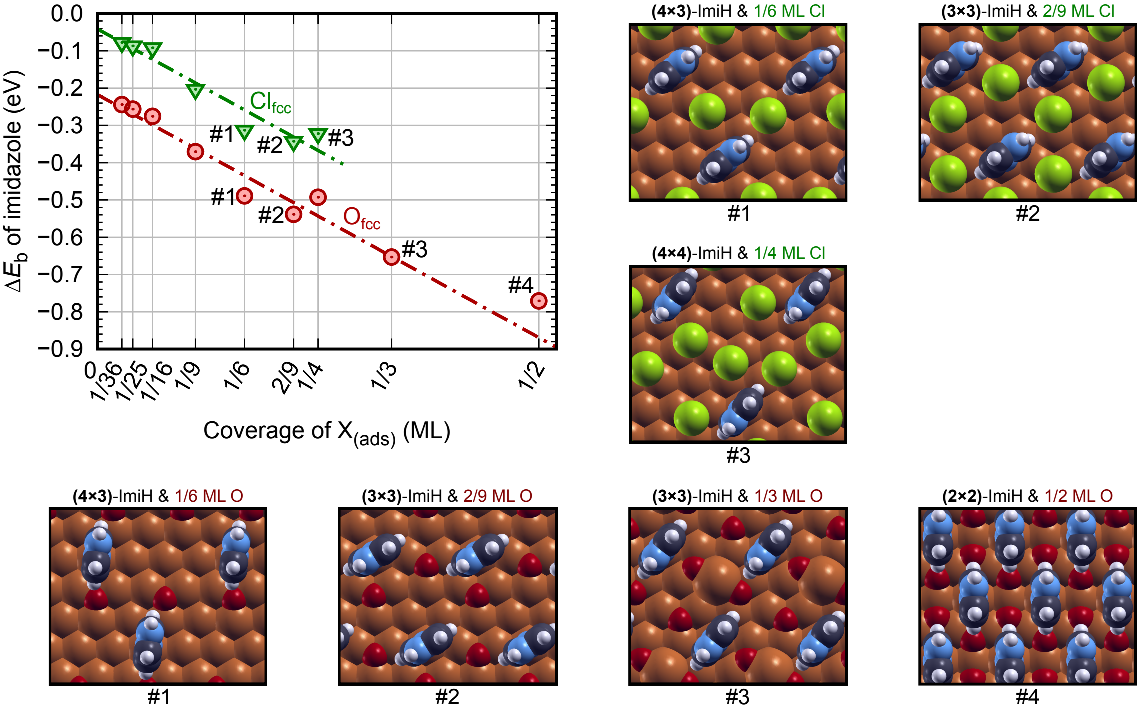

Figure 4.17: Top left: ΔE_b of imidazole on O/Cu(111) and Cl/Cu(111) as a function of the $O_{(\mathrm{ads})}$ and $Cl_{(\mathrm{ads})}$ coverage. At each $X_{(\mathrm{ads})}$ coverage, only the most stable identified imidazole structure is considered. Data are taken from Figure 4.9, except datapoints labeled #1, #2, #3, and #4 correspond to the structures shown next to the chart. The #1 and #2 structures correspond to $2X_{(\mathrm{ads})}$ per (4×3) and (3×3) supercells, respectively, the $Cl_{(\mathrm{ads})}$ #3 structure corresponds to $4Cl_{(\mathrm{ads})}$ per (4×4) supercell (two Cl are adsorbed onto off-fcc and two Cl onto off-hcp sites, where the "off" prefix indicates that Cl is displaced from the hollow toward the bridge site), the $O_{(\mathrm{ads})}$ #3 structure corresponds to $3O_{(\mathrm{ads})}$ per (3×3) supercell with one O adsorbed onto hcp and two O onto fcc sites, whereas the $O_{(\mathrm{ads})}$ #4 structure consists of $2O_{(\mathrm{ads})}$ per (2×2) supercell with one O adsorbed onto hcp and the other one onto fcc sites. The ΔE_b values are always calculated with respect to the compatible ImiH @ X/Cu(111) vs. X/Cu(111) structures, where compatibility is achieved by removing imidazole from ImiH @ X/Cu(111) and relaxing the so-obtained X/Cu(111) structure.

why ΔE_b depends linearly on the $X_{(\mathrm{ads})}$ coverage. Moreover, notice from Figure 4.9 that also distant sites are affected by the presence of $X_{(\mathrm{ads})}$, although the influence diminishes with the $X_{(\mathrm{ads})}$ coverage. Hence, there should also be some non-local or global effect by which $X_{(\mathrm{ads})}$ affects the adsorption of imidazole. We will show in the next subsection that this global effect as well as the linear dependence of ΔE_b on the $X_{(\mathrm{ads})}$ coverage (cf. Figure 4.17) is related to the $X_{(\mathrm{ads})}$ induced work-function change, which also depends linearly on the coverage (cf. Figure 4.3 and Eq. (3.23)). By extrapolating ΔE_b to zero coverage (Figure 4.17), we can deduce the local effect of $X_{(\mathrm{ads})}$ on the binding of the nearby adsorbed imidazole (note that the zero coverage corresponds to a single imidazole adsorbed near a single $X_{(\mathrm{ads})}$ in the infinitely large supercell). The $O_{(\mathrm{ads})}$ induced ΔE_b of imidazole at zero coverage is -0.22 eV. This enhancement is too strong to be solely attributed to the CH$\cdots$O hydrogen bond between imidazole and $O_{(\mathrm{ads})}$ because the strength of such H-bonds is estimated to be about 0.1 eV (see the Supplementary material of Ref. [75]).

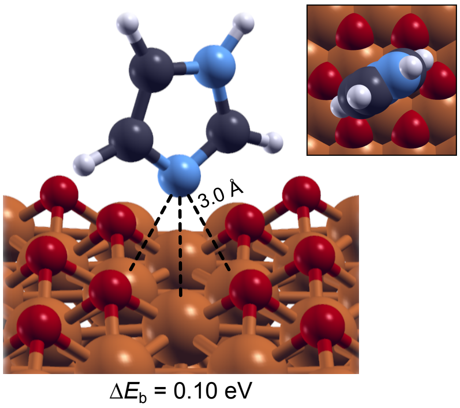

Figure 4.18: Imidazole adsorbed on 2/3 ML O/Cu(111). O adatoms are exclusively adsorbed onto the most stable fcc sites, hence only grey top sites exist at this coverage. Imidazole, therefore, cannot adsorb at a top site. Instead, it adsorbs high above the surface with its N3 atom facing toward a free fcc site, such that the N–Cu bond lengths are about 3.0 Å. Surprisingly, imidazole adsorption is destabilized by only 0.1 eV with respect to clean Cu(111), i.e., $\Delta E_\mathrm{b} = 0.10$ eV. This calculation was performed with the (3×3) supercell.

The remaining contribution thus comes from the $\mathrm{O_{(ads)}}$ induced strengthening of the N–Cu bond.[6] For $\mathrm{Cl_{(ads)}}$, the ΔE_b value at zero coverage is only -0.04 eV. Such a small magnitude can be attributed to a lack of hydrogen bonding.

4.1.6 Relation between work function and ΔE_b

It has already been stated that the ΔE_b results presented in Figure 4.9 demonstrate that the presence of $\mathrm{X_{(ads)}}$ species affects imidazole adsorption not only on nearby sites but also on distant sites. However, the effect diminishes with the coverage of $\mathrm{X_{(ads)}}$. The $\Delta\rho(\mathbf{r})$ plots of Figure 4.13 also indicate that the $\mathrm{O_{(ads)}}$ induced enhancement of the N–Cu bond diminishes as the coverage of $\mathrm{O_{(ads)}}$ decreases, although in all these cases, imidazole is adsorbed at the blue site that is nearby $\mathrm{O_{(ads)}}$. Last but not least, Figure 4.17 reveals that the ΔE_b effect depends linearly on the coverage of $\mathrm{O_{(ads)}}$ or $\mathrm{Cl_{(ads)}}$. These observations indicate that some non-local effect affects the bonding of imidazole and diminishes as the coverage of $\mathrm{X_{(ads)}}$ decreases. We propose that this effect is related to the work function or, more precisely, to the $\mathrm{X_{(ads)}}$ induced change of the work function ($\Delta\Phi$), which depends linearly on the coverage of $\mathrm{X_{(ads)}}$ (see Figure 4.3 on page 21). This proposition is not only supported by the observation that both $\Delta\Phi$ and ΔE_b depends linearly on the coverage of $\mathrm{X_{(ads)}}$ (see Figures 4.3 and 4.17) but, moreover, by the following evidence: $\mathrm{O_{(ads)}}$ and $\mathrm{Cl_{(ads)}}$ increase the work function (Figure 4.3) and also strengthen the adsorption binding of imidazole ($\Delta E_\mathrm{b} < 0$, Figures 4.9 and 4.17), whereas $\mathrm{OH_{(ads)}}$ decreases the work function and, consequently, diminishes the adsorption binding of imidazole (except for a few cases). $\mathrm{H_{(ads)}}$ has a negligible effect on the work function and therefore affects ΔE_b insignificantly.

The work-function argument is made more quantitative in Figure 4.19, which shows the dependence of ΔE_b on $\Delta\Phi$; in Figure 4.19a all sites from Figure 4.9 are considered, however,

---

[6] Although Figure 4.13 suggests that this effect reduces with the $\mathrm{O_{(ads)}}$ coverage, it seems that at zero coverage (corresponding to a single imidazole adsorbed near a single $\mathrm{O_{(ads)}}$ in the infinitely large supercell), the effect does not vanish. A possible explanation is that the electronegative $\mathrm{O_{(ads)}}$ makes nearby Cu atoms slightly more electrophilic and thus more susceptible to binding with the electronegative N3 atom of imidazole.

to disentangle the local effects from the global work-function effect, only the distant green sites are considered in Figure 4.19b, whereas Figure 4.19c instead considers only the most stable imidazole sites on O/Cu(111) and Cl/Cu(111), where the data from Figure 4.17 are utilized. The linear correlation between ΔE_b and $\Delta\Phi$ is clearly evident, particularly in Figures 4.19b and 4.19c. In contrast, the correlation in Figure 4.19a is not as good because all the sites are considered therein, but only the nearby sites are affected by the additional stabilization due to local interactions between imidazole and $\mathrm{X}_{\mathrm{(ads)}}$, such as H-bonding (this is why datapoints for the blue and yellow sites on O/Cu(111) appear below the regression line in Figure 4.19a). It is worth noting that the regression line in Figures 4.19b, which considers the distant green sites, passes very close to the $(\Delta\Phi, \Delta E_\mathrm{b}) = (0, 0)$ point. The reason is that for the distant green sites, the local interactions between imidazole and $\mathrm{X}_{\mathrm{(ads)}}$ are missing, hence only the work-function effect remains. According to the $\Delta\Phi$ hypothesis, the ΔE_b should be zero when $\Delta\Phi$ is zero, provided that local effects are missing, which is what happens precisely in Figures 4.19b. Figure 4.19 therefore provides a strong support for the work-function hypothesis.

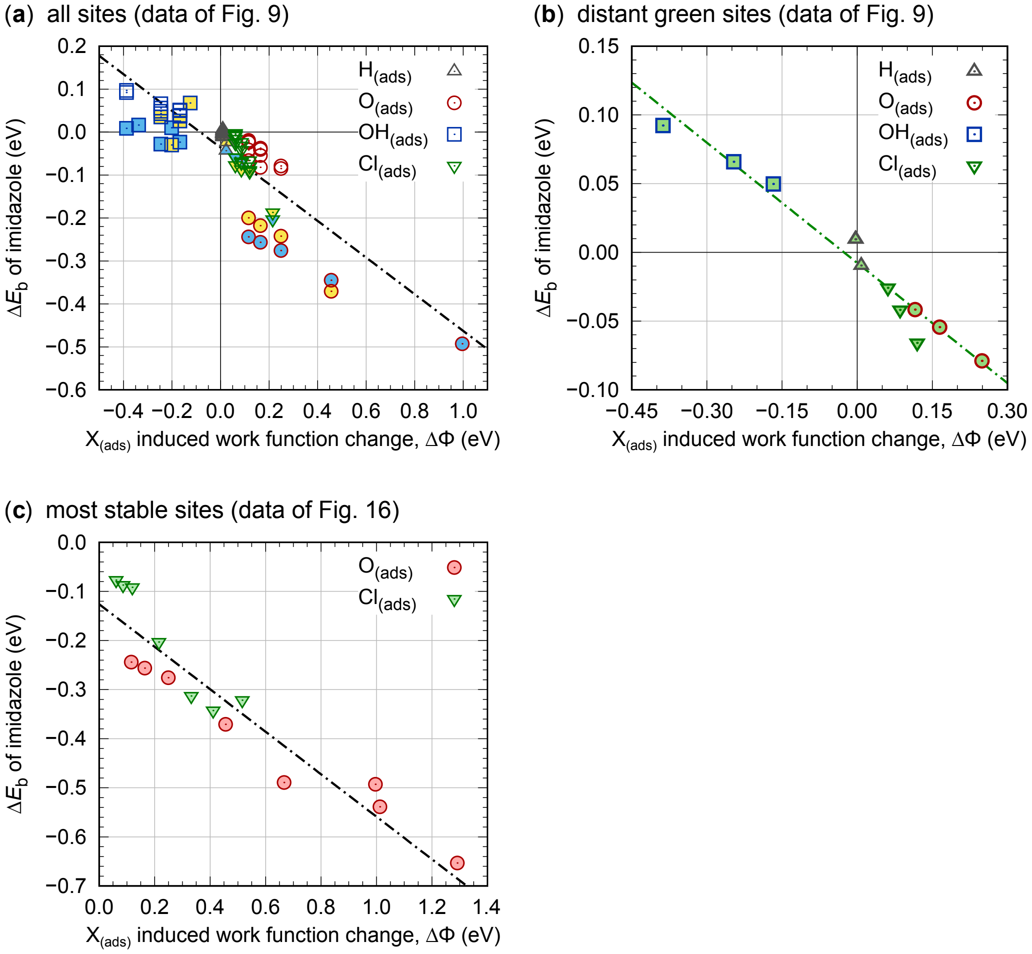

Figure 4.19: ΔE_b of imidazole versus $\mathrm{X}_{\mathrm{(ads)}}$ induced work-function change ($\Delta\Phi$). In (a), all the sites, in (b), the distant green sites, and in (c), the most stable sites at each coverage are considered. In (a) and (b), the ΔE_b values correspond to those in Figure 4.9, whereas in (c), the data from Figure 4.17 are used. In (a), the datapoints corresponding to the nearby blue and yellow sites are shown with blue and yellow background colors, whereas in (b), datapoints are colored with a green background to indicate that they correspond to green sites.

Why $\Delta\Phi$ of $X_{(ads)}$ affects ΔE_b of imidazole? One way to rationalize the relation between $\Delta\Phi$ and ΔE_b is by means of the electron charge-transfer parameter (ΔN) of the HSAB (Hard and Soft Acids and Bases) principle [76]. The rationalization is based on the premise that the adsorption binding energy is proportional to the charge transfer between the adsorbed molecule and the surface. This premise has been established for atomic and molecular adsorbates on transition metal surfaces [61], [77], [78]. Instead of the explicitly calculated charge of the adsorbed molecule, we utilize the ΔN parameter, firstly because it is physically easy to understand and secondly because it has been shown that it linearly correlates with the DFT calculated charge of adsorbed atoms [77], [78] and molecules [18], [61], [77]. According to ΔN, the electron charge transfer between two fragments is proportional to their electronegativity difference and is opposed by the sum of their chemical hardnesses, i.e., electron charge transfer is promoted by a large difference in electronegativity and is opposed by a high chemical hardness. For the interaction between a molecule and a metal surface, the ΔN parameter is given by [77]:

$$\Delta N = \frac{\chi_{\text{surf}} - \chi_{\text{mol}}}{2(\eta_{\text{surf}} + \eta_{\text{mol}})} = \frac{\Phi - \chi_{\text{mol}}}{2\eta_{\text{mol}}}, \tag{4.2}$$

where χ and η stands for the Mulliken electronegativity and the chemical hardness, respectively, and the subscripts "surf" and "mol" stand for the surface and molecule, respectively. The electronegativity of the metal surface is given by its work function [77], while its chemical hardness is related to the inverse of the density of states at Fermi energy [79], which is an exceedingly small number for bulk metals, hence $\eta_{\text{surf}} = 0$ is an excellent approximation for metal surfaces that is utilized in Eq. (4.2).

For imidazole adsorbed on bare Cu(111), ΔN is given by:

$$\Delta N = \frac{\Phi_{\text{Cu(111)}} - \chi_{\text{ImiH}}}{2\eta_{\text{ImiH}}}, \tag{4.3}$$

whereas for imidazole adsorbed on X/Cu(111), it is given by:

$$\Delta N' = \frac{\Phi_{\text{X/Cu(111)}} - \chi_{\text{ImiH}}}{2\eta_{\text{ImiH}}}. \tag{4.4}$$

By utilizing the $E_b \propto -|\Delta N|$ premise[7] together with Eqs. (3.1)–(3.3), (4.3), and (4.4), the relation between ΔE_b and $\Delta\Phi$ is straightforwardly established:

$$\begin{aligned}\Delta E_b = E_b' - E_b &\propto -(|\Delta N'| - |\Delta N|)\\ &\propto -\left(\frac{\Phi_{\text{X/Cu(111)}} - \chi_{\text{ImiH}}}{2\eta_{\text{ImiH}}} - \frac{\Phi_{\text{Cu(111)}} - \chi_{\text{ImiH}}}{2\eta_{\text{ImiH}}}\right)\\ &\propto -\frac{\Phi_{\text{X/Cu(111)}} - \Phi_{\text{Cu(111)}}}{2\eta_{\text{ImiH}}}\\ &\propto -\Delta\Phi, \end{aligned} \tag{4.5}$$

where

$$\Delta\Phi = \Phi_{\text{X/Cu(111)}} - \Phi_{\text{Cu(111)}}. \tag{4.6}$$

---

[7] According to this premise, the higher the magnitude of the electron charge transfer between the adsorbate and the surface is, the more exothermic is the binding energy. This can be written as $E_b \propto -|\Delta N|$, which implies that only the magnitude and not the direction of the electron charge transfer matters.

In the derivation of Eq. (4.5) the following relations were used:

$$\Phi_{\mathrm{X/Cu(111)}} - \chi_{\mathrm{ImiH}} > 0 \quad \text{and} \quad \Phi_{\mathrm{Cu(111)}} - \chi_{\mathrm{ImiH}} > 0. \tag{4.7}$$

Indeed, imidazole is less electronegative than Cu(111), i.e., the PBE calculated values are $\chi_{\mathrm{ImiH}} = 4.32$ eV [18] and $\Phi_{\mathrm{Cu(111)}} = 4.83$ eV [77]. X/Cu(111) surfaces are also more electronegative than imidazole (cf. Figure 4.3 on page 21), the only exception is $\mathrm{OH_{fcc}}$/Cu(111) at 1/9 and 1/4 ML coverage. However, at such high coverage OH shifts to bridge site upon adsorption of imidazole and $\mathrm{OH_{br}}$/Cu(111) is always more electronegative than imidazole because $\Delta\Phi_{\mathrm{OH_{br}}} > -0.5$ eV (cf. Figure 4.3), where -0.5 eV corresponds to $\chi_{\mathrm{ImiH}} - \Phi_{\mathrm{Cu(111)}}$.

The $\Delta E_{\mathrm{b}} \propto -\Delta\Phi$ relation of Eq. (4.5) therefore provides a simple explanation of the trend observed in Figure 4.19 and explains why $\mathrm{O_{(ads)}}$ and $\mathrm{Cl_{(ads)}}$ strengthen the bonding of imidazole on Cu(111), $\mathrm{H_{(ads)}}$ has no effect, and $\mathrm{OH_{(ads)}}$ diminishes the bonding of imidazole (except for a few cases).

4.2 $\mathrm{O_{(ads)}}$ and $\mathrm{OH_{(ads)}}$ Induced Dissociative Adsorption of Imidazole and Benzotriazole

To this end, we have addressed how adsorbed corrosion relevant species such as H, O, OH, and Cl affect the non-dissociative adsorption of imidazole on copper surfaces, where imidazole was used as a toy model of azole corrosion inhibitors. We have shown in the preceding section that O and OH can form stabilizing hydrogen bonds with the adsorbed imidazole molecule. In this section, we concentrate on the aftermath of such hydrogen bond formation. Once a strong intramolecular interaction between $\mathrm{X_{(ads)}}$ and imidazole is formed, a molecule can be further stabilized by deprotonation that involves a hydrogen shift from the molecule to a near chemisorbed coadsorbate. Some of the results presented in this section have been published in a companion article to this thesis, entitled *Dissociative adsorption of azoles on Cu(111) promoted by chemisorbed O and OH* [60].

The dissociative effect was observed on Cu(111) covered with either $\mathrm{O_{(ads)}}$ or $\mathrm{OH_{(ads)}}$ in the case of imidazole and was studied also for benzotriazole. The skeletal structures of both molecules are shown in Figure 4.20.

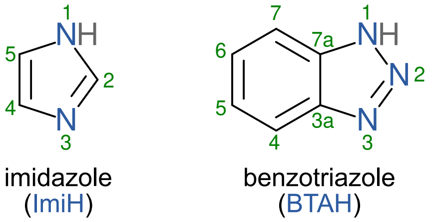

Figure 4.20: Skeletal structures of imidazole and benzotriazole molecules. Atom numbers and molecular abbreviations are also indicated.

Despite the fact that imidazole is not commonly used as a corrosion inhibitor [80], it can be seen as an archetypal model of imidazole-based corrosion inhibitors. Contrary to this, benzotriazole is an outstanding and widely used corrosion inhibitor for copper [23].

While DFT methods have been extensively used to study imidazole and benzotriazole adsorption on copper surfaces [14]–[16], [18], [62], [81]–[89], the issue of $\mathrm{X_{(ads)}}$ induced deprotonation has not yet been thoroughly addressed.

These two molecules were selected based on the following considerations. Deprotonation of benzotriazole involves the cleavage of the N1–H bond [90], whereas deprotonation of adsorbed imidazole can also involve the cleavage of the C2–H bond [20]. These two molecules therefore cover two qualitatively different cases: deprotonation of an azole molecule either at a heteroatom or at the carbon atom.

$X_{(ads)}$ species do not only affect the non-dissociative adsorption of azole molecules, as discussed in a previous section, but in some cases they also promote a bond-breaking, such as molecular deprotonation, leading to further stabilization of adsorbed molecules [12], [19], [20]. In this section, we discuss the following two types of molecular deprotonation:

$$\mathrm{MolH}_{(ads)} + \mathrm{O}_{(ads)} \rightarrow \mathrm{Mol}_{(ads)} + \mathrm{OH}_{(ads)}, \tag{4.8}$$

$$\mathrm{MolH}_{(ads)} + \mathrm{OH}_{(ads)} \rightarrow \mathrm{Mol}_{(ads)} + \mathrm{H_2O}_{(ads)}. \tag{4.9}$$

It is noteworthy that both $O_{(ads)}$ and $OH_{(ads)}$ reactants are consumed in these two reactions. For this reason, from now on, the coverage of $O_{(ads)}$ and $OH_{(ads)}$ always corresponds to the coverage of reactant $O_{(ads)}$ and $OH_{(ads)}$. The corresponding deprotonation reaction energies ($\Delta E_{\mathrm{deprot}}$) are calculated as:

$$\Delta E_{\mathrm{deprot}} = E_{\mathrm{FS}} - E_{\mathrm{IS}}, \tag{4.10}$$

where E_{IS} and E_{FS} stand for total energies of initial (reactants) and final (products) states in reaction (4.8) or (4.9).

The total stabilization of molecular adsorption ($\Delta E_{\mathrm{stab}}^{\mathrm{tot}}$) induced by $X_{(ads)}$ is given by the sum of ΔE_{b}, $\Delta E_{\mathrm{shift}}$, and $\Delta E_{\mathrm{deprot}}$:

$$\Delta E_{\mathrm{stab}}^{\mathrm{tot}} = \Delta E_{\mathrm{b}} + \Delta E_{\mathrm{shift}} + \Delta E_{\mathrm{deprot}}, \tag{4.11}$$

where ΔE_{b} corresponds to the $X_{(ads)}$ induced enhancement of the MolH adsorption bonding, $\Delta E_{\mathrm{shift}}$ is the energy required for the $X_{(ads)}$ and MolH to rearrange to a structure, which is the most convenient for deprotonation, and $\Delta E_{\mathrm{deprot}}$ represents the additional stabilization caused by the deprotonation reaction.

4.2.1 Dissociative adsorption on bare Cu(111)

In order to better understand the role of $O_{(ads)}$ and $OH_{(ads)}$ in molecular deprotonation reactions on copper surfaces, let us first consider dissociation reactions involving the Mol–H cleavage on bare surface:

$$\mathrm{MolH}_{(ads)} \rightarrow \mathrm{Mol}_{(ads)} + \mathrm{H}_{(ads)}. \tag{4.12}$$

However, on Cu(111), this reaction would be more appropriately referred to as H-abstraction rather than deprotonation, because H adsorbed to the bare Cu(111) is negatively charged, as reported in Figure 4.4; its Bader charge is −0.32, hence it is hydride- and not proton-like. Also on Cu_2O surfaces, H is negatively charged if adsorbed to Cu ions, but it is proton-like if adsorbed to O ions [19].

Figure 4.21 presents the PBE+D" calculated H-abstraction reaction energies for ImiH and BTAH adsorbed on bare Cu(111) along with the corresponding initial- and final-state structures (these calculations were performed with one molecule per (4×4)–Cu(111) supercell).

Although it seems chemically intuitive that deprotonation of imidazole should proceed via the cleavage of the N1–H bond, Kokalj et al. [20] found that on Cu_2O surfaces (and likewise on Fe(100) [91]), the cleavage of the C2–H bond is thermodynamically preferred over the N1–H bond breaking. Results connected to this thesis also show this to be the case on bare Cu(111), where the reaction energy for the C2–H cleavage of 0.2 eV is substantially smaller (less endothermic) than that for the cleavage of the N1–H bond of about 0.8 eV, as reported by Kokalj et al. [60]. In ref. [60] other adsorption forms, like physisorption, are also disscused but were not investigated in the scope of the thesis.

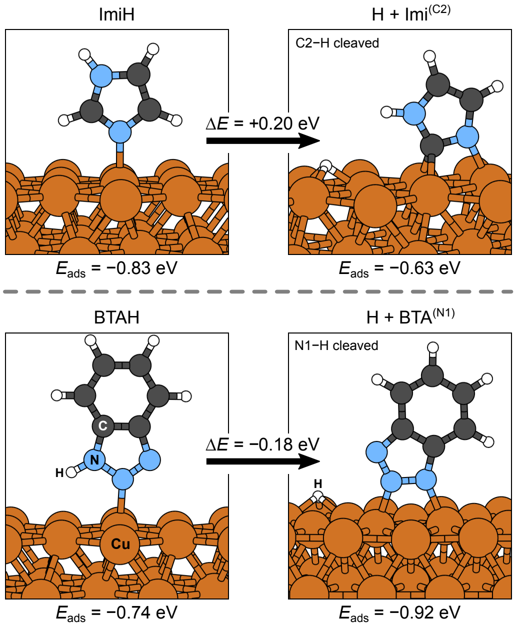

Figure 4.21: H-abstractions from ImiH [top] and BTAH [bottom] adsorbed on bare (4×4)–Cu(111). The PBE+D"-calculated reaction energies (ΔE) are given. E_{ads} stands for the adsorption energy of a molecule on to the surface. The superscript in the $\mathrm{Imi}^{(\mathrm{C2})}$ label indicates that H-abstraction involves the cleavage of the C2–H bond and similarly for the $\mathrm{BTA}^{(\mathrm{N1})}$, where the N1–H bond is cleaved.

In contrast to ImiH, H-abstraction of BTAH involves the N1–H bond cleavage, and the reaction energy is slightly exothermic, $\Delta E = -0.18$ eV at 1/16 ML,[8] whereas the activation barrier was calculated in a study by Kokalj et al. [90] to be about 1 eV.

4.2.2 Dissociative adsorption on X/Cu(111)

Calculated reaction energies along with the initial and final-state structures for deprotonation reactions (4.8) and (4.9) on X/Cu(111) are shown in Figure 4.22 for C2–H bond cleavage of ImiH and in Figure 4.23 for BTAH N1–H bond cleavage. The reactions summarized in both figures were modeled at a molecular coverage of 1/16 ML using the (4×4)–MolH @ X/Cu(111) systems, i.e., the (4×4) supercell containing one X species and one MolH.

4.2.2.1 C2–H bond cleavage of imidazole

Table 4.2 presents PBE+D" calculated reaction energies for the C2–H bond cleavage reactions on $(n\times n)$–X/Cu(111), where $n = 3, 4, 5, 6$. For imidazole, different supercells were used in order to evaluate the impact of the coverage on the deprotonation reactions. From the calculated results, it can be concluded that for $\mathrm{O}_{(\mathrm{ads})}$, thermodynamic contributions do not depend strongly on the supercell size. $\Delta E^{\mathrm{tot}}_{\mathrm{stab}}$ ranges from -0.7 eV to -0.4 eV from the smallest to the largest supercell. In the case of $\mathrm{OH}_{(\mathrm{ads})}$, $\Delta E^{\mathrm{tot}}_{\mathrm{stab}}$ depends on the size of the supercell to a more significant extent. $\Delta E^{\mathrm{tot}}_{\mathrm{stab}}$ exponantely incerases from -0.22 to -0.03 eV with the increasing supercell size from (3×3)– to (6×6)–OH/Cu(111). Reaction paths for C2–H bond cleavage of imidazole (ImiH) are depicted in Figure 4.22.

---

[8] This value of ΔE is more exothermic than the value of about 0.1 eV reported by Kokalj et al. [90]. The reason is that in ref. [90] the value corresponds to BTA and H coadsorbed to adjacent nearest-neighbor sites where they experience some lateral repulsion.

Table 4.2: Summary of energies contributing to the dissociative adsorption of ImiH on O/Cu(111) and OH/Cu(111). Calculations were performed using $(n \times n)$ supercell ($n = 3, 4, 5, 6$) with one coadsorbate and one molecule adsorbed per supercell. ΔE_{b} is the difference between a given non-dissociative E_{ads} on X/Cu(111) and that on bare Cu(111), $\Delta E_{\mathrm{shift}}$ is the energy needed to convert the most stable ImiH–$(n \times n)$–X/Cu(111) structure to the corresponding convenient initial-state structure for H-abstraction, and $\Delta E_{\mathrm{deprot}}$ is the deprotonation reaction energy. $\Delta E^{\mathrm{tot}}_{\mathrm{stab}}$ is a sum of the three (cf. Eq. 4.11).

	O/Cu(111)				OH/Cu(111)			
super-cell	ΔE_{b} (eV)	$\Delta E_{\mathrm{shift}}$ (eV)	$\Delta E_{\mathrm{deprot}}$ (eV)	$\Delta E^{\mathrm{tot}}_{\mathrm{stab}}$ (eV)	ΔE_{b} (eV)	$\Delta E_{\mathrm{shift}}$ (eV)	$\Delta E_{\mathrm{deprot}}$ (eV)	$\Delta E^{\mathrm{tot}}_{\mathrm{stab}}$ (eV)
(3×3)	−0.37	/	−0.28	−0.65	−0.03	/	−0.19	−0.22
(4×4)	−0.26	0.03	−0.23	−0.46	0.01	0.06	−0.18	−0.11
(5×5)	−0.25	0.04	−0.24	−0.45	−0.03	0.06	−0.09	−0.06
(6×6)	−0.24	0.04	−0.23	−0.43	−0.02	0.05	−0.06	−0.03

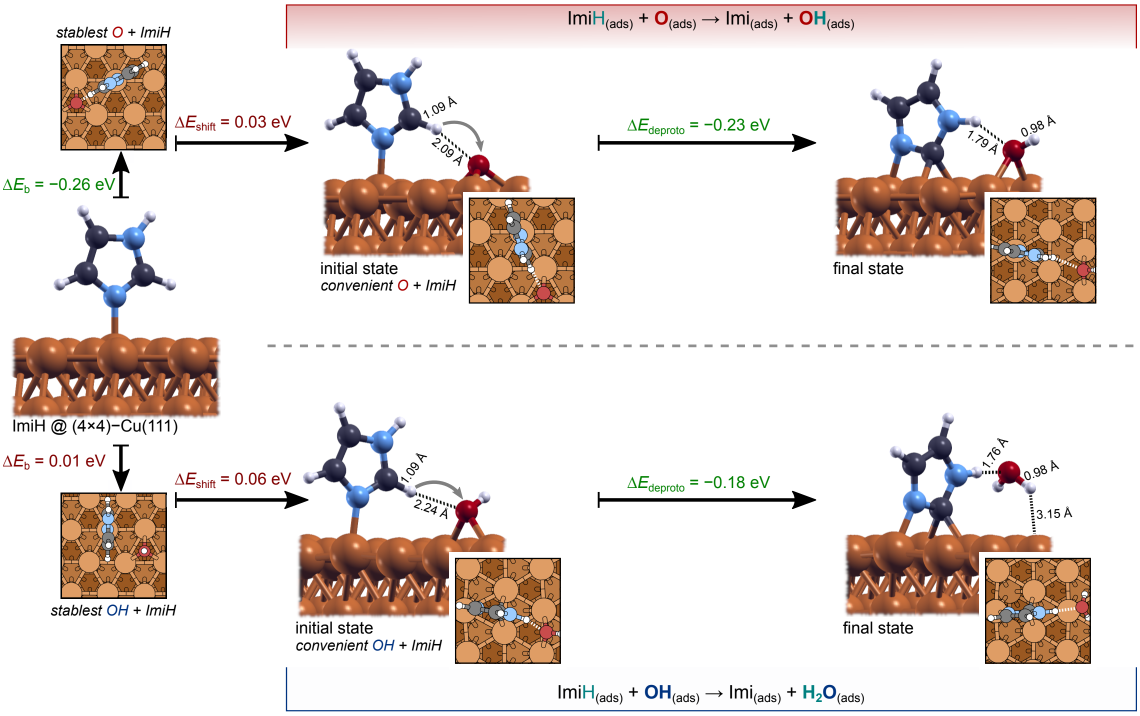

Figure 4.22: Reaction paths for C2–H bond cleavage of imidazole (ImiH). On the far left, ImiH @ (4×4)–Cu(111) and the stablest identified ImiH structures on (4×4)–O/Cu(111) [top] and (4×4)–OH/Cu(111) [bottom] are shown, followed by (from left to right) the reaction initial- and final-state structures. Corresponding PBE+D" calculated characteristic energies and bond lengths are also depicted. ΔE_{b} measures the stabilization of the adsorbed molecule induced by the coadsorbed $X_{(ads)}$ $\Delta E_{\mathrm{shift}}$ is the energy cost required to rearrange the most stable ImiH + $X_{(ads)}$ structure to the one convenient for deprotonation. $\Delta E_{\mathrm{deprot}}$ corresponds to the energy released in the deprotonation.

4.2.2.2 N1–H bond cleavage of benzotriazole

Figure 4.23 reveals that at 1/16 ML coverage, $O_{(ads)}$ and $OH_{(ads)}$ stabilize an intact adsorbed BTAH by 0.65 and 0.27 eV, respectively, which can be attributed to the three effects explained in section 4.1.2. $BTAH_{(ads)}$ forms a strong NH$\cdots$O hydrogen bond with $O_{(ads)}$ and $OH_{(ads)}$. The strength of this hydrogen bond is estimated to be about 0.3 ± 0.1 eV [75]. Therefore, the formed hydrogen bond almost entirely explains the $OH_{(ads)}$ induced stabilization of adsorbed BTAH. In contrast, $O_{(ads)}$ also enhances the N–Cu bond between the nearby adsorbed azole and the surface [59], which is why the $O_{(ads)}$ induced stabilization of intact adsorbed BTAH ($\Delta E_b = -0.65$ eV) is much stronger than the one induced by $OH_{(ads)}$ ($\Delta E_b = -0.27$ eV).

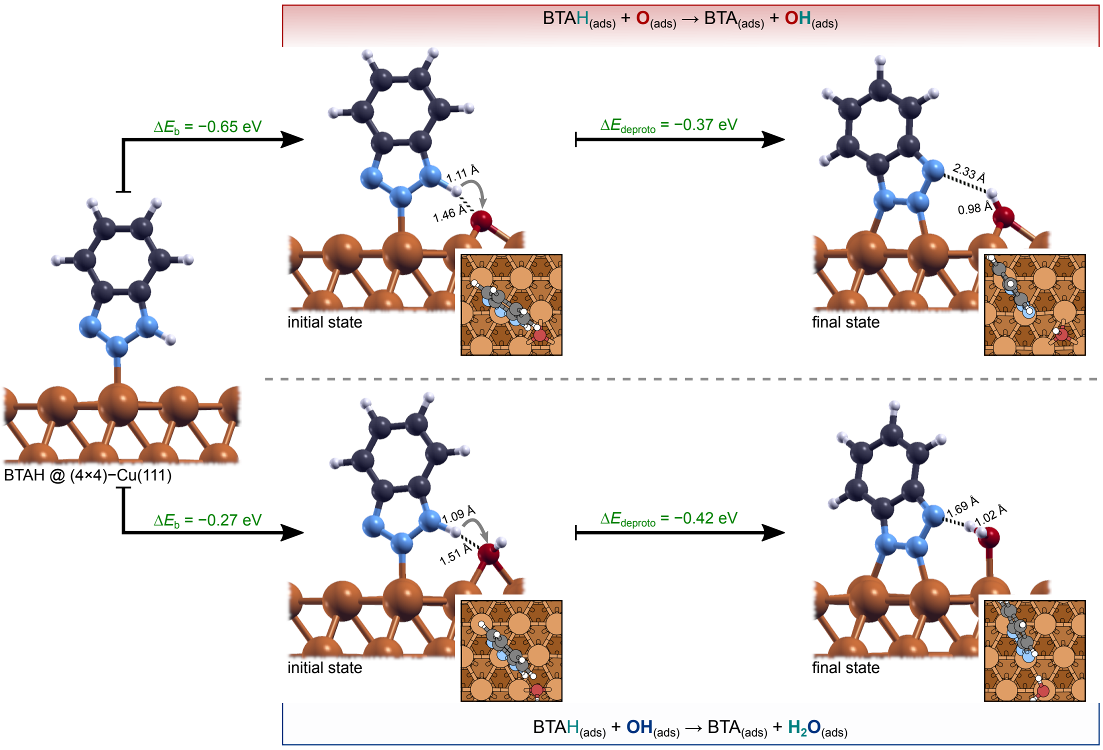

Figure 4.23: Deprotonation reaction path for the N1–H bond cleavage of benzotriazole (BTAH) on Cu(111) induced by $O_{(ads)}$ [top] and $OH_{(ads)}$ [bottom] at 1/16 ML. From left to right: BTAH @ (4×4)–Cu(111), BTAH adsorbed near $O_{(ads)}$ and $OH_{(ads)}$ thereon (labeled as the initial state), and deprotonated BTA (final state) with the corresponding co-product of deprotonation.

Adsorbed BTAH can further stabilize by about 0.4 eV by proton transfer from its N1 atom to either $O_{(ads)}$ or $OH_{(ads)}$. The calculated reaction energies of deprotonation reactions (4.8) and (4.9) at 1/16 ML are -0.37 and -0.42 eV, respectively.

The total thermodynamic stabilization (ΔE_{stab}^{tot}) of adsorbed benzotriazole induced by $O_{(ads)}$ and $OH_{(ads)}$ at 1/16 ML is -1.02 and -0.69 eV, respectively (cf. Figure 4.23). Although these values depend on the $X_{(ads)}$ coverage, as shown in the supplementing article [60], they are sizable enough to conclude that both $O_{(ads)}$ and $OH_{(ads)}$ significantly stabilize adsorbed benzotriazole and induce its deprotonation, resulting in $BTA_{(ads)}$ on the copper surface.

In summary, Figure 4.22 shows that the calculated reaction energies for the C2–H bond cleavage are less exothermic ($\Delta E_{deprot} \gtrsim -0.2$ eV) when compared with N1–H bond cleavage of benzotriazole ($\Delta E_{\mathrm{deprot}} \approx -0.4$ eV) as depicted in Figure 4.23. Furthermore, $\mathrm{ImiH}_{(ads)}$ is stabilized considerably less than $\mathrm{BTAH}_{(ads)}$ by $O_{(ads)}$ and $OH_{(ads)}$ because the formed CH$\cdots$O hydrogen bond between imidazole and $X_{(ads)}$ is considerably weaker than the NH$\cdots$O hydrogen bond [75] between $\mathrm{BTAH}_{(ads)}$ and $X_{(ads)}$. These aspects contribute to the finding that $O_{(ads)}$ and $OH_{(ads)}$ stabilize imidazole considerably less than benzotriazole. In particular, at 1/16 ML coverage of $X_{(ads)}$, the total stabilization energy ($\Delta E^{\mathrm{tot}}_{\mathrm{stab}}$) (Eq. 4.11) of adsorbed imidazole induced by $O_{(ads)}$ and $OH_{(ads)}$ is -0.46 and -0.11 eV, respectively, whereas the corresponding values for benzotriazole are -1.02 and -0.69 eV. All these values can be deduced from Figures 4.22 and 4.23.

4.2.3 Adsorption energies and persistence of adsorbed molecules

The discussion so far has focused on the $O_{(ads)}$ and $OH_{(ads)}$ induced stabilization of molecular adsorption via the ΔE_{b} and $\Delta E_{\mathrm{deprot}}$ contributions. The remainder of this discussion will be devoted to the adsorption energies described in Table 4.3. On bare Cu(111) at molecular coverage of 1/16 ML, the PBE+D" calculated non-dissociative adsorption energies of ImiH and BTAH are -0.83 eV and -0.74 eV, respectively. It is worth commenting that the adsorption energies of azoles depend on the coverage due to long-ranged lateral intermolecular interactions, which result from sizable permanent dipole moments of azole molecules [13], [61], [92].

Table 4.3: PBE+D" calculated adsorption energies of non-dissociative and dissociative adsorption of ImiH and BTAH on bare Cu(111), O/Cu(111), and OH/Cu(111). Calculations were performed at a molecular and coadsorbate coverage of 1/16 ML using the (4×4)–Cu(111) supercell. ΔE_{b} is the difference between a given non-dissociative E_{ads} on X/Cu(111) and that on bare Cu(111), whereas $\Delta E^{\mathrm{tot}}_{\mathrm{stab}}$ is the difference between a given dissociative $E^{\mathrm{diss}}_{\mathrm{ads}}$ on X/Cu(111) and non-dissociative E_{ads} on bare Cu(111).

Surface	Adsorption mode	E_{ads} (eV)	ΔE_{b} (eV)	Adsorption mode	$E^{\mathrm{diss}}_{\mathrm{ads}}$ (eV)	$\Delta E^{\mathrm{tot}}_{\mathrm{stab}}$ (eV)
	non-dissociative ImiH			disociative $\mathrm{Imi}^{(C2)}+$ H		
Cu(111)		-0.83	/		-0.63	0.20
O/Cu(111)		-1.09	-0.26		-1.29	-0.46
OH/Cu(111)		-0.82	0.01		-0.92	-0.11
	non-dissociative BTAH			disociative $\mathrm{BTA}^{(N1)}+$ H		
Cu(111)		-0.74	/		-0.92	-0.18
O/Cu(111)		-1.39	-0.65		-1.76	-1.02
OH/Cu(111)		-1.01	-0.27		-1.43	-0.69

Table 4.3 summarizes the effect of $O_{(ads)}$ and $OH_{(ads)}$ on the stabilzation of adsorbed molecules. Under the premise that a molecule must adsorb to the surface to become a corrosion inhibitor, it is important to estimate the residence time of a molecule on a surface. Inhibitors should adsorb strong enough, or else they would quickly desorb. $O_{(ads)}$ and $OH_{(ads)}$ enhancement of adsorption energy has important consequences as it exponentially increases molecular residence time on a surface. A typical residence time (τ) can be estimated from the inverted Arrhenius equation:

$$\tau = \nu^{-1} \exp(E_{\mathrm{des}}/k_{\mathrm{B}}T), \tag{4.13}$$

where ν is the frequency prefactor, k_B is the Boltzmann constant and T is temperature. E_{des} is the desorption energy, which can be estimated by the magnitude of the adsorption energy ($E_{des} = |E_{ads}|$). A typical residence time of investigated adsorbed molecules was calculated using $\nu = 10^{16}$ s^{-1}, which is a typical value for the frequency prefactor of desorption [93]–[95].

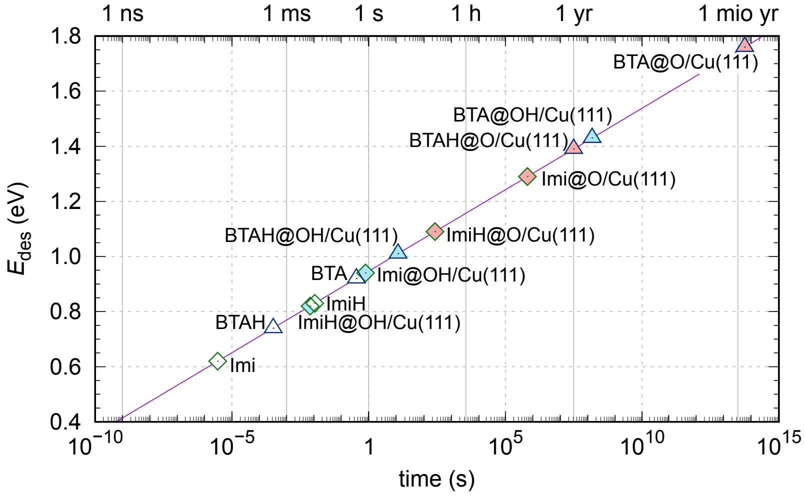

Figure 4.24: A typical residence time (τ) of imidazole (diamond symbols) and benzotriazole (triangles) on bare Cu(111) [open symbols], O/Cu(111) [red-colored symbols], and OH/Cu(111) [blue-colored symbols] as a result of non-dissociative and dissociative adsorption. The residence times were calculated with Eq. 4.13 at room temperature.

In Figure 4.24, typical residence times for investigated adsorbed molecules are given for the 1/16 ML coverage of $X_{(ads)}$ and bare Cu(111) utilizing (4 × 4) supercell.

For ImiH, the typical residence time of non-dissociatively adsorbed ImiH on (4 × 4)-Cu(111) is about 10 milliseconds ($E_{ads} = -0.83$ eV). On (4 × 4)–O/Cu(111), it is about 10 days (E_{ads} of -1.09 eV), and on (4 × 4)-OH/Cu(111), it is about 7 milliseconds (E_{ads} of -0.82 eV). In the case of dissociative adsorption, the residence time of Imi on bare copper surface reduces by about three orders of magnitude compared to ImiH ($E_{ads} = -0.63$ eV). For dissociative adsorption of ImiH on O/Cu(111) and OH/Cu(111), the estimated typical residence times at room temperature range from about one second (E_{ads}^{diss} of -0.92 eV) to one week (E_{ads}^{diss} of -1.29 eV).

For BTAH, the $O_{(ads)}$ and $OH_{(ads)}$ induced ΔE_{stab}^{tot} stabilization reaches the value of -1.02 and -0.69 eV, respectively. Hence, the corresponding dissociative adsorption energies are sizable, around -1.43 to -1.76 eV. A typical residence time of BTAH on Cu(111) ($E_{ads} = -0.74$ eV) and OH/Cu(111) ($E_{ads} = -1.01$ eV) at room temperature is estimated to be 0.3 millisecond and about 10 seconds, respectively. In contrast, the residence times of BTAH on O/Cu(111) are considerably longer (for $E_{ads} = -1.39$ eV, the residence time is about 1 year). According to results for dissociative adsorption plotted in Figure 4.24, BTA has a typical residence time of 5 years and up to 2 million years for OH/Cu(111) and O/Cu(111) at 1/16 ML $X_{(ads)}$ coverage, respectively. Thus, from the human perception of time, BTAH desorption is rapid on bare Cu(111), almost negligible on OH/Cu(111), and irreversible for the dissociatively adsorbed benzotriazole on O/Cu(111).

It should be noted that the above surface residence times for deprotonated molecules were estimated by assuming recombinative two-step desorption. The first step in this two-step desorption is protonation of $Mol_{(ads)}$ and the second step is desorption of MolH. For both steps, a frequency prefactor of 10^{16} s^{-1} was assumed.

Chapter 5

Calculations of Hydrated Coordination Complexes

The complexation of molecules with metal cations is relevant in the context of corrosion inhibition and can be viewed as contrasting to adsorption. Namely, if molecular adsorption can be assumed to inhibit corrosion, then by similar reasoning, the formation of stable soluble complexes should accelerate corrosion.

As noted in the introductory section of the thesis, the computational studies in the literature primarily concentrate on the adsorption of inhibitor molecules on surfaces, while their interaction with metal cations in aqueous solutions is rarely discussed. In this context, the formation of complexes between azole-type inhibitor molecules, and Cu(I) or Cu(II) ions was studied. To this end, 19 N-heterocyclic molecules, presented in Figure 3.4, are considered. These 19 molecules are taken from the Kokalj et al. dataset [54], which were previously regarded as corrosion inhibitors for copper in sodium chloride solution.

5.1 Copper–Water Coordination Complexes

Structures of solvated Cu(I) and Cu(II) in water solvent have already been thoroughly explored computationally by means of a cluster/continuum approach, which considers several water molecules explicitly and the rest of the solvent implicitly [57], [58], [96]–[98]. To this end, solvated Cu(I) and Cu(II) ions are considered as $[Cu(H_2O)_n]^{x+}$ complexes solvated in an implicit water solvent. To evaluate the structure and stability of Cu–water complexes in the implicit solvent, we first studied different coordination modes. All Cu(I) complexes were treated as closed-shell systems because the Cu(I) cation has a $3d^{10}$ electron configuration. In contrast, Cu(II) has an open shell $3d^9$ electron configuration and was treated as spin-polarized. It is known that the first water solvation shell around Cu(I) and Cu(II) cations is linear and square-planar, respectively [57], [58], [98]. Hence, the corresponding complexes can be written as $[Cu(H_2O)_2]^+$ and $[Cu(H_2O)_4]^{2+}$. Our calculations reproduce these findings. Optimized geometries of investigated Cu–water complexes and solvation Gibbs energies are depicted in Figure 5.1, whereas formation energies of coordination complexes and also solvation Gibbs energies are summarized in Table 5.1.

According to our calculated formation energies of coordination complexes, square-planar rearrangement of four water molecules with additional two water molecules in the second shell is by 0.3 eV more stable compared to the distorted octahedral orientation of six water ligands in the first solvation shell around Cu(II).

Implicit solvent models often provide inaccurate estimations of the Gibbs energy of solvation for charged species. For example, our calculated G_{solv} for solvated Cu(I) and Cu(II) are -5.5 and -20.5 eV, to be compared with the experimental values of -6.1 and

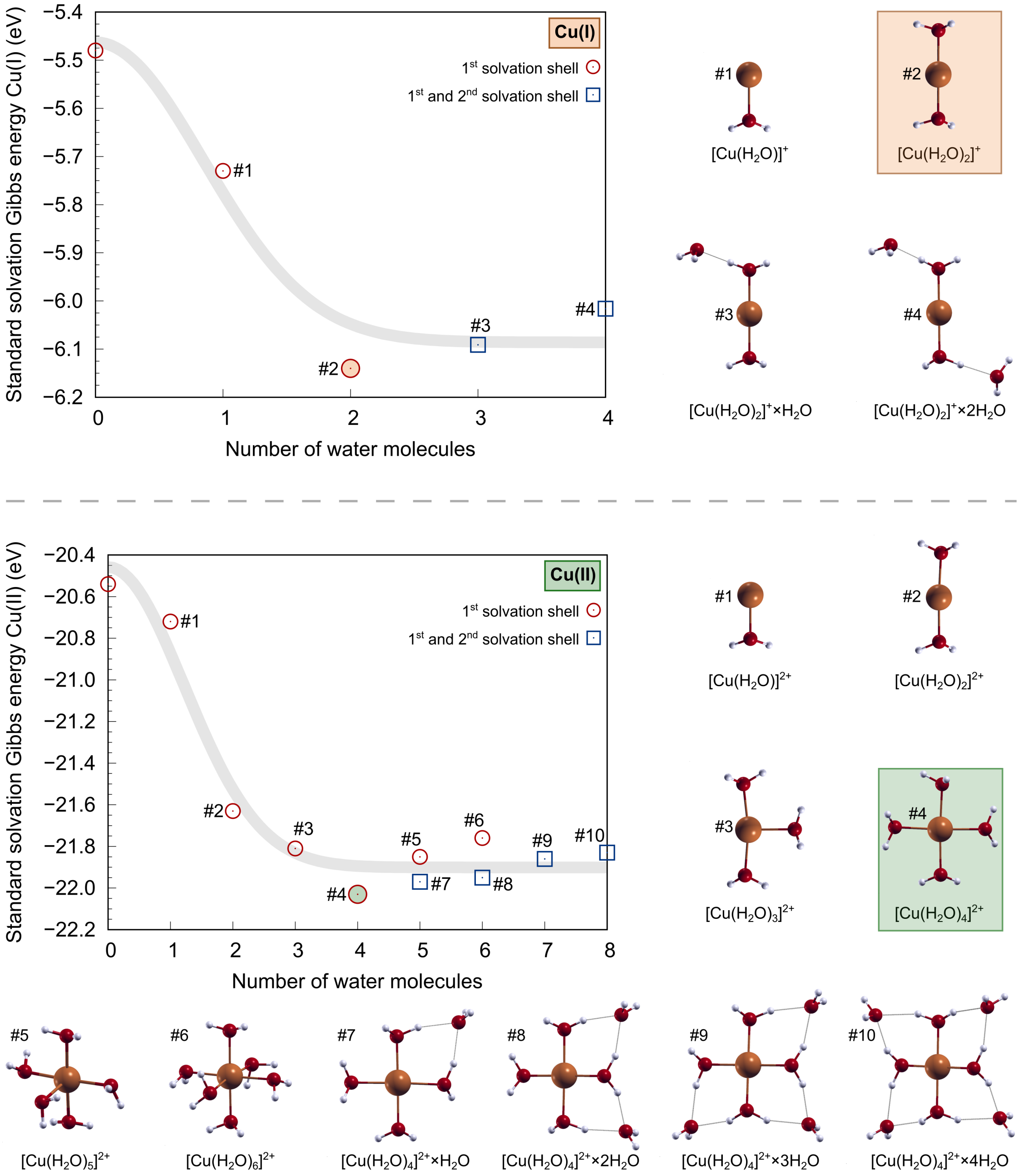

Figure 5.1: Standard solvation Gibbs energy of Cu(I) [above] and Cu(II) [below] as a function of the number of water molecules coordinated around central ions, forming first and second solvation shells. Images correspond to calculations performed in the SMD implicit solvent. Structures outlined with squares were chosen for further investigation of the formation of complexes with L ligands. The pale thick curves are drawn to guide the eye.

−22.0 eV [97], respectively. Hence, the SMD model underestimates the G_{solv} magnitude by 0.6 eV for solvated Cu(I) and 1.5 eV for solvated Cu(II) compared to experimental results. Thus, a cluster/continuum model was employed, where a limited number of water molecules are treated explicitly, while all other water molecules are accounted for implicitly

Table 5.1: The $[\mathrm{Cu(H_2O)}_n]^{x+}$ formation energies (E_{form}) for $x = 1$ and 2, and the solvation Gibbs energies (G_{solv}) of Cu^{x+}. The coordination number (n) corresponds to a total number of coordinated water molecules in the first solvation shell. The $[\mathrm{Cu(H_2O)}_n]^{x+} \cdot w\mathrm{H_2O}$ notation represents square-planar 4-coordinated Cu(II)-complex with explicitly treated w water molecules in the second solvation shell.

	E_{form} (eV)		G_{solv} (eV)	
molecular formula	Cu(I)	Cu(II)	Cu(I)	Cu(II)
Cu^{x+}	/	/	−5.48	−20.54
$[\mathrm{Cu(H_2O)}]^{x+}$	−0.47	−0.45	−5.73	−20.72
$\mathbf{[Cu(H_2O)_2]^{x+}}$	**−1.18**	−1.62	**−6.14**	−21.63
$[\mathrm{Cu(H_2O)_3}]^{x+}$	/	−2.13	/	−21.81
$[\mathrm{Cu(H_2O)_2 \cdot H_2O}]^{x+}$	−1.14	/	−6.09	/
$\mathbf{[Cu(H_2O)_4]^{x+}}$	/	**−2.67**	/	**−22.03**
$[\mathrm{Cu(H_2O)_2 \cdot 2H_2O}]^{x+}$	−1.43	/	−6.02	/
$[\mathrm{Cu(H_2O)_5}]^{x+}$	/	−2.85	/	−21.85
$[\mathrm{Cu(H_2O)_4 \cdot H_2O}]^{x+}$	/	−3.03	/	−21.97
$[\mathrm{Cu(H_2O)_6}]^{x+}$	/	−3.04	/	−21.76
$[\mathrm{Cu(H_2O)_4 \cdot 2H_2O}]^{x+}$	/	−3.35	/	−21.95
$[\mathrm{Cu(H_2O)_4 \cdot 3H_2O}]^{x+}$	/	−3.66	/	−21.86
$[\mathrm{Cu(H_2O)_4 \cdot 4H_2O}]^{x+}$	/	−3.96	/	−21.83

with the SMD model. To obtain a more precise estimation of the solvation Gibbs energy, G_{solv}, for Cu(I) and, particularly, Cu(II) ion, we utilized the following reaction:

$$\mathrm{Cu(H_2O)}_n]^{x+} \cdot w\mathrm{H_2O}_{\mathrm{(aq)}} \leftrightharpoons \mathrm{Cu}^{x+}_{\mathrm{(aq)}} + (n+w)\mathrm{H_2O}_{\mathrm{(aq)}}, \tag{5.1}$$

where both parts of the reaction describe the same system but expressed with different models. The left side corresponds to the cluster/continum model and the right side to the implicit model. n represents a number of water ligands bound directly to the central ion, and w stands for water molecules from the second solvation shell. From reaction (5.1), an improved estimation of the solvation Gibbs energy of copper ions ($x = 1$ or 2) can be obtained. The following relation can be written:

$$G^{\mathrm{1M,(aq)}}([\mathrm{Cu(H_2O)}_n]^{x+} \cdot w\mathrm{H_2O}) = G^{\mathrm{1M,(aq)}}(\mathrm{Cu}^{x+}) + (n+w)G^{\mathrm{55M,(aq)}}(\mathrm{H_2O}), \tag{5.2}$$

where the $G^{\mathrm{1M,(aq)}}(\mathrm{Cu}^{x+})$ term is given by:

$$G^{\mathrm{1M,(aq)}}(\mathrm{Cu}^{x+}) = G^{\mathrm{1atm,(g)}}(\mathrm{Cu}^{x+}) + k_{\mathrm{B}}T \ln\left(\frac{\text{“1M”}}{\text{“1atm”}}\right) + G_{\mathrm{solv}}(\mathrm{Cu}^{x+}). \tag{5.3}$$

From Eqs. 5.2 and 5.3, the solvation Gibbs energy of Cu^{x+} can be expressed as:

$$\begin{aligned} G_{\mathrm{solv}}(\mathrm{Cu}^{x+}) = {} & G^{\mathrm{1M,(aq)}}([\mathrm{Cu(H_2O)}_n]^{x+} \cdot w\mathrm{H_2O}) \\ & - G^{\mathrm{1atm,(g)}}(\mathrm{Cu}^{x+}) - k_{\mathrm{B}}T \ln\left(\frac{\text{“1M”}}{\text{“1atm”}}\right) \\ & - (n+w)G^{\mathrm{55M,(aq)}}(\mathrm{H_2O}), \end{aligned} \tag{5.4}$$

where all contributions to the Gibbs energy were considered as depicted in Figure 3.6.

It can be seen from Figure 5.1 that adding explicit water molecules increases the exergonicity of G_{solv} up to a given point and then saturates. Based on these results, we chose $[\mathrm{Cu(H_2O)_2}]^+$ and $[\mathrm{Cu(H_2O)_4}]^{2+}$ as the most appropriate cluster/continuum models. The $G_{\mathrm{solv}}(\mathrm{Cu^+})$ value derived from the $[\mathrm{Cu(H_2O)_2}]^+$ model is -6.1 eV, and the $G_{\mathrm{solv}}(\mathrm{Cu^{2+}})$ value derived from the $[\mathrm{Cu(H_2O)_4}]^{2+}$ model is -22.0 eV. Both values are in excellent agreement with experiments (-6.1 and -22.0 eV, respectively [97]).

5.2 Copper–Chloride Coordination Complexes

In order to elucidate the stability of Cu–L complexes, where L stands for a ligand, it is elucidating to establish a reference system utilizing some well-known corrosion activator. Hence, $\mathrm{Cl^-}$ was used, which is a typical corrosion activator. Corrosion activators, such as $\mathrm{Cl^-}$ accelerate metal anodic dissolution, which is a driving force behind metal degradation. Therefore, copper electrodissolution in chloride media has been widely investigated [70], [99]–[103]. It proceeds through a dissolution of metal following the electrochemical reactions among which the first step is:

$$\mathrm{Cu_{(s)}} + \mathrm{Cl^-_{(aq)}} \leftrightharpoons \mathrm{CuCl_{(s)}} + e^-, \tag{5.5}$$

where insoluble CuCl is formed near the copper surface. In the subsequent step, a soluble $[\mathrm{CuCl_2}]^-$ complex is formed in excess chloride medium:

$$\mathrm{CuCl_{(s)}} + \mathrm{Cl^-_{(aq)}} \leftrightharpoons [\mathrm{CuCl_2}]^-_{(\mathrm{aq})}. \tag{5.6}$$

The so-formed soluble $[\mathrm{CuCl_2}]^-$ complex diffuses through the extended layer into a bulk solution. Overtime, the formed complex can further oxidize to cupric ion according to the electrochemical reaction depicted below:

$$[\mathrm{CuCl_2}]^-_{(\mathrm{aq})} \leftrightharpoons \mathrm{Cu^{2+}_{(aq)}} + 2\mathrm{Cl^-_{(aq)}} + e^-. \tag{5.7}$$

Formed Cu(II) interacts with chlorides in the bulk solution through to the following chemical process:

$$\mathrm{Cu^{2+}_{(aq)}} + n\mathrm{Cl^-_{(aq)}} \leftrightharpoons [\mathrm{CuCl}_n]^{(n-2)-}_{(\mathrm{aq})}. \tag{5.8}$$

According to the reaction above, many soluble cupric-chloride complexes can form in the aqueous solvent. The stability of different Cu–chloride complexes has been confirmed experimentally [103] and computationally [104]. Among them, soluble $[\mathrm{CuCl_4}]^{2-}$ is a well-known product of the accelerated corrosion in aqueous media containing chloride ions.

Figure 5.2 shows a formation of $[\mathrm{CuCl_2}]^-$ and $[\mathrm{CuCl_4}]^{2-}$ complexes from $[\mathrm{Cu(H_2O)_2}]^+$ and $[\mathrm{Cu(H_2O)_4}]^{2+}$, respectively. $[\mathrm{CuCl_2}]^-$ is known to be present near copper surface in chloride media [105], whereas $[\mathrm{CuCl_4}]^{2-}$ is present in the bulk solution. In the reaction path shown in Figure 5.2, water bonded to the central metal ion via O atom is substituted with a negatively charged chloride ion. Cu(I) ion can form stable Cu–Cl coordinate covalent bonds resulting in a linearly coordinated complex, while Cu(II) cation can interact with up to four $\mathrm{Cl^-}$ ions, yielding a square-planar coordination complex, similar to $[\mathrm{Cu(H_2O)_4}]^{2+}$ complex shown in Figure 5.1. The standard Gibbs energy of formation of $[\mathrm{CuCl_2}]^-$ and $[\mathrm{CuCl_4}]^{2-}$ is exergonic by -1.35 and -1.80 eV, respectively.

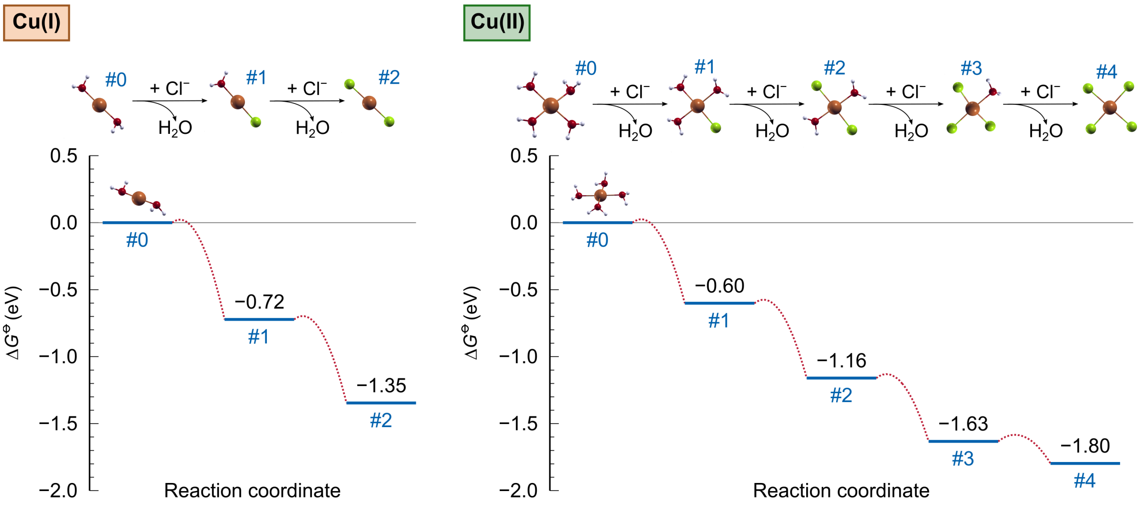

Figure 5.2: Standard reaction Gibbs energy profiles ($\Delta G^{\ominus}$) for transformation of $[Cu(H_2O)_2]^+$ into $[CuCl_2]^-$ [left] and $[Cu(H_2O)_4]^{2+}$+ into $[CuCl_4]^{2-}$ [right]. The snapshots of reactants, intermediates, and products are shown above the graphs.

5.3 Copper–Ligand Coordination Complexes

The following section discusses how the 19 N-heterocyclic molecules form coordination complexes with Cu(I) or Cu(II) central ions. A schematic representation of coordination compounds formation is shown in Figure 5.3, whereas Figures 5.4–5.9 show the most stable reaction path profiles with structures and standard Gibbs energies of formation of 2- or 4-coordinated complexes from $[Cu(H_2O)_2]^+$ and $[Cu(H_2O)_4]^{2+}$, respectively. Cu(I) complexes display linear geometry, while Cu(II) preferably takes a square-planar arrangement of ligands. In the following, we present structures and reaction paths of coordination complexes for all investigated heterocyclic molecules, where each subsection is titled according to the group of considered ligands.

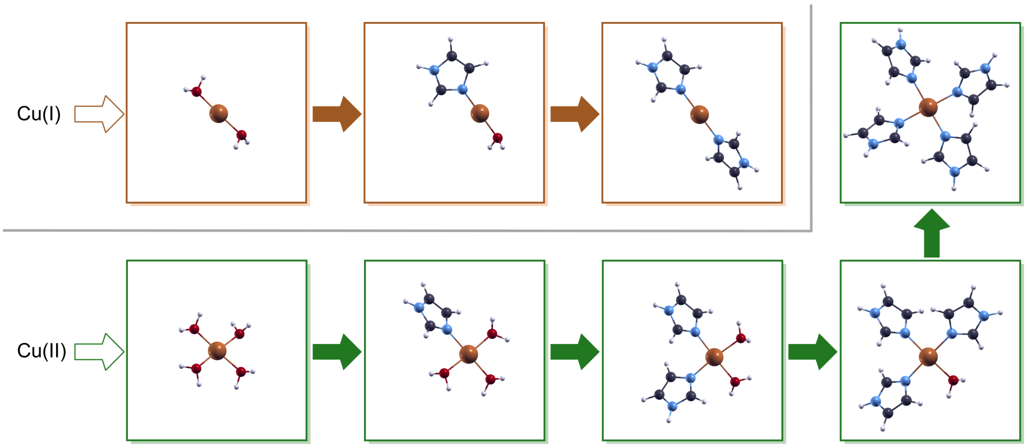

Figure 5.3: Schematic representation of stepwise substitution of water ligands with L ligands. Imidazole is used as a representative ligand because it is the smallest among the considered N-heterocyclic molecules. The Cu(I) complexes display a linear geometry, whereas Cu(II) complexes have a square-planar rearrangement of ligands.

5.3.1 Mercapto-azoles

Figure 5.4 shows standard reaction Gibbs energy ($\Delta G^{\ominus}$) profiles for the formation of $[Cu(L)_2]^+$ coordination complexes from $[Cu(H_2O)_2]^+$, whereas Figure 5.5 presents the analogous results for the formation of $[Cu(L)_4]^{2+}$ from $[Cu(H_2O)_4]^{2+}$.

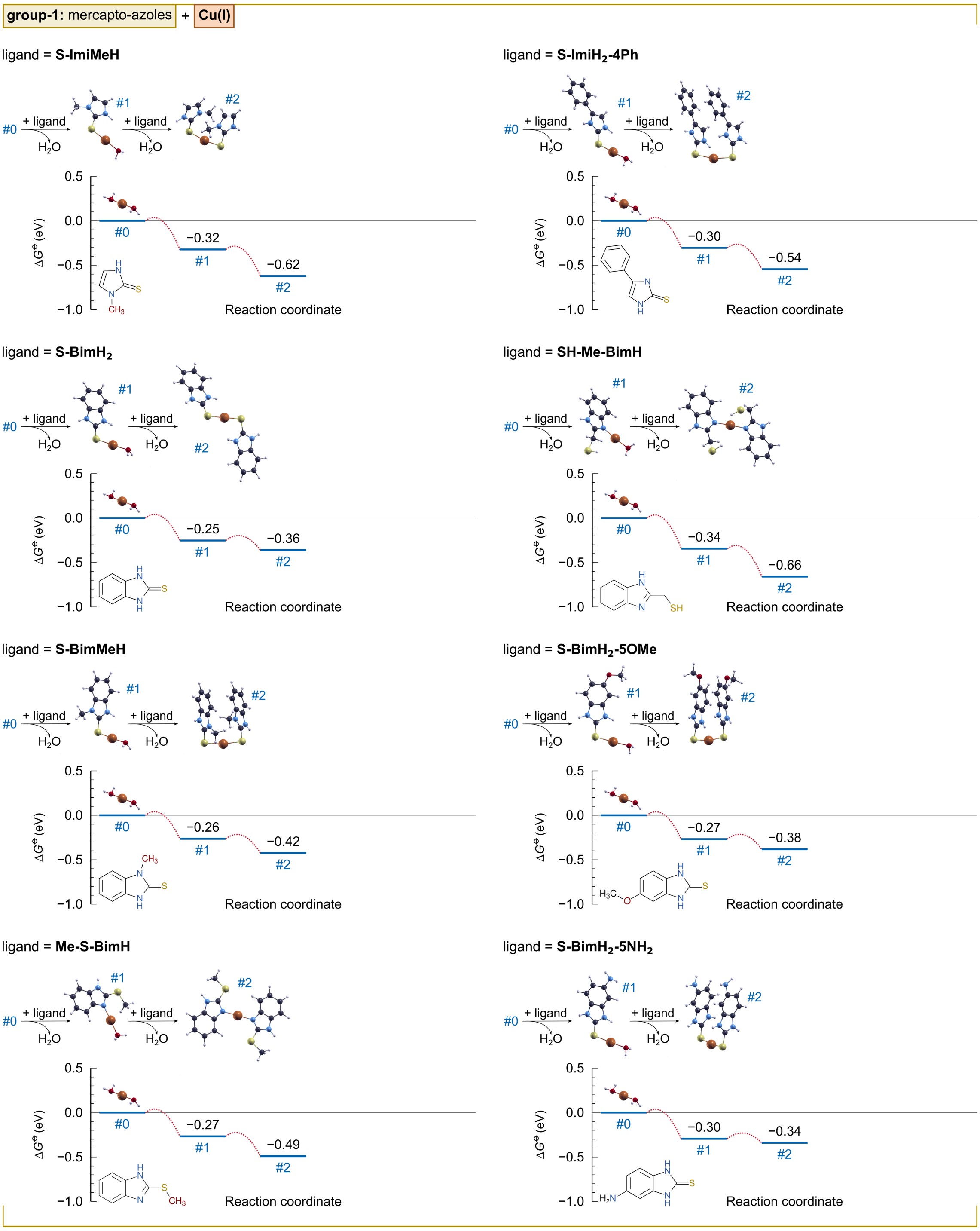

Figure 5.4: Standard reaction Gibbs energy ($\Delta G^{\ominus}$) profiles for the formation of $[Cu(L)_2]^+$ complexes from hydrated Cu(I) for investigated mercapto-azole ligands.

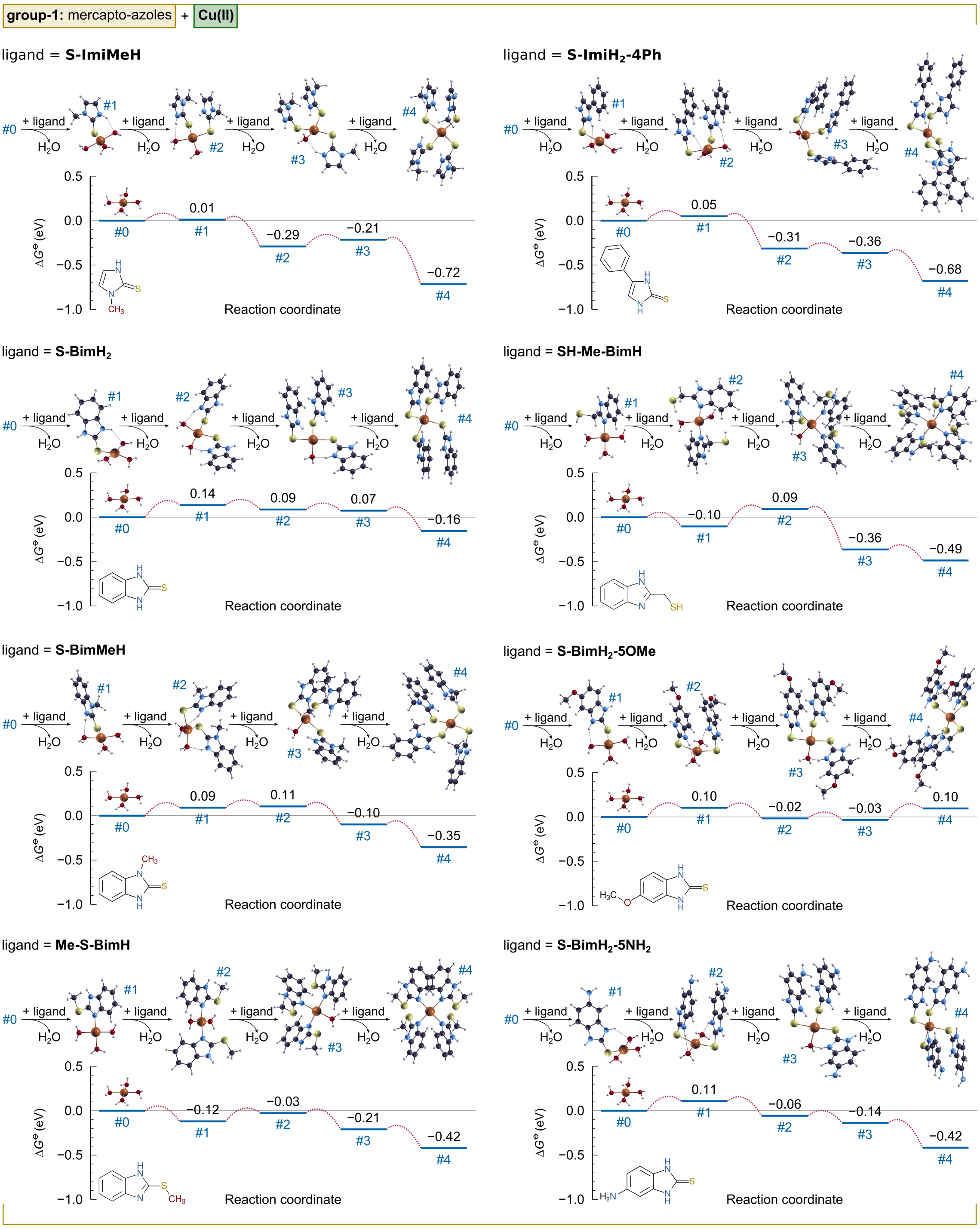

Figure 5.5: Standard reaction Gibbs energy ($\Delta G^{\ominus}$) profiles for the formation of $[Cu(L)_4]^{2+}$ complexes from hydrated Cu(II) for investigated mercapto-azole ligands.

Mecapto-azole ligands with thione functional groups will preferably form coordinate bonds via S atom. Ligands that do not contain the thione group (Me-S-BimH and SH-Me-BimH), bind to the central ion via the pyridine-type N atom from the heterocycle. All L-containing Cu(I) complexes are thermodynamically more stable compared to the hydrated Cu(I) with $\Delta G^{\ominus}$ ranging from −0.7 to −0.3 eV. In contrast, the formation of

Cu(II) complexes with four L ligands is more evolved. The standard reaction Gibbs energy for the formation of $[Cu(L)_4]^{2+}$ complexes is exergonic with $\Delta G^{\ominus} \in (-0.6, -0.4)$ eV for all but the S-BimH$_2$-5OMe ligand, for which $\Delta G^{\ominus}$ is 0.1 eV. Nevertheless, for every ligand, the reaction path from hydrated Cu(II) to $[Cu(L)_4]^{2+}$ involves one or more endergonic elementary steps.

While the majority of considered mercapto-azoles bond to Cu ions as monodentates via S atoms, S-BimH$_2$-5NH$_2$ is able to complexate copper ions either with the S atom from the thione group or the N atom from the amino group. According to our results, the ligand bonding to Cu(I) with the S atom is 0.17 eV more stable than that of the N atom (see Figure C.1 in Appendix C). As for the bonding of S-BimH$_2$-5NH$_2$ to Cu(II), the $[Cu(L)_4]^{2+}$ complex is only marginally more stable than the hydrated Cu(II) when the ligands bind via the N atom (Figure C.3). Mixed via-S and via-N bonding is also possible but it is thermodynamically inferior to the complexation via the S atom by 0.04 eV and 0.31 eV for Cu(I) and Cu(II), respectively (cf. Figures C.1 and C.3).

5.3.2 Hydoxy-heterocycles

Figure 5.6 shows standard reaction Gibbs energies and structures of the most stable identified coordination complexes with Cu(I), while Figure 5.7 summarizes the results for Cu(II).

O-BimH$_2$ ligand forms a coordinate bond with the O atom and forms coordination complexes with Cu(I) and Cu(II) that are inferior to $[Cu(H_2O)_2]^+$ and $[Cu(H_2O)_4]^{2+}$, respectively, i.e., $\Delta G^{\ominus} > 0$. In contrast, the complexes with OH-Me-BimH, coordinated to Cu ions via the pyridine-type N atom, are by −0.6 and −0.8 eV more exergonic compared to hydrated Cu(I) and Cu(II) ions, respectively. Quin-8OH forms a stable $[Cu(L)_2]^+$ complex that is by −0.2 eV more exergonic relative to $[Cu(H_2O)_2]^+$.

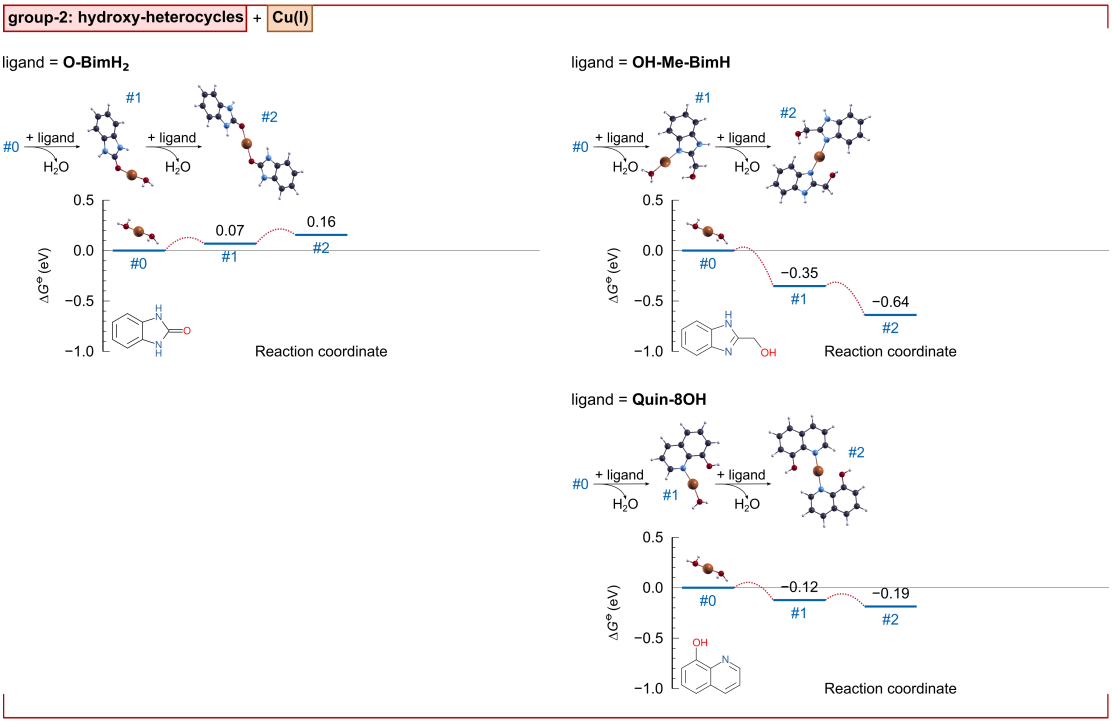

Figure 5.6: Standard reaction Gibbs energy ($\Delta G^{\ominus}$) profiles for the formation of $[Cu(L)_2]^+$ complexes from hydrated Cu(I) for investigated hydoxy-heterocycle ligands.

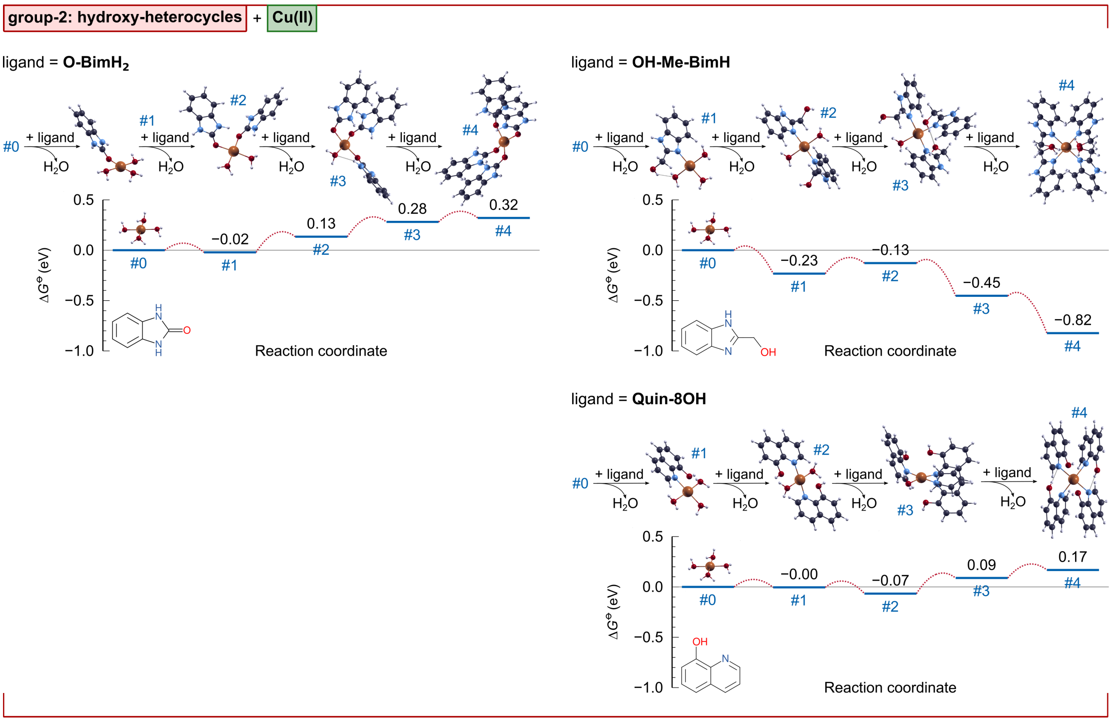

Figure 5.7: Standard reaction Gibbs energy ($\Delta G^{\ominus}$) profiles for the formation of $[Cu(L)_4]^{2+}$ complexes from hydrated Cu(II) for investigated hydoxy-heterocycle ligands.

Futhermore, there are two ways in which Quin-OH can interact with Cu(II) ion: either as a monodentate ligand bonding with the N atom, or as a bidentate ligand complexating via the N and O atoms as shown in Figure C.4. For monodentate binding, the formation of $[Cu(L)_4]^{2+}$ is slightly endergonic ($\Delta G^{\ominus} = 0.2$ eV), whereas the formation of bidentate $[Cu(L)_2]^{2+}$ is slightly exergonic ($\Delta G^{\ominus} = -0.1$ eV).

Results in Figure C.4 summarize the bidentate nature of Quin-OH ligand and point toward similar stability of monodentate $[Cu(Quin\text{-}8OH)_4]^{2+}$ and bidentate $[Cu(Quin\text{-}8OH)_2]^{2+}$, indicating that both forms can coexist. With $\Delta G^{\ominus} = -0.1$ eV both formed complexes represent the stablest local minima in the reaction path. In the stablest identified complexes with Cu(I) and Cu(II), Quin-OH coordinates the central ion with O and N atoms, acting as a bidentate ligand.

5.3.3 Benzazoles and imidazole

The structures and standard reaction Gibbs energies involved in the formation of benzazole ligand-containing coordination compounds are depicted in Figure 5.8 for the Cu(I) and in Figure 5.9 for the Cu(II).

The formation of $[Cu(InzH)_2]^{+}$ is exergonic by −0.2 eV, while the formation of the compound $[Cu(InzH)_4]^{2+}$ is endergonic by 0.2 eV relative to the hydrated Cu ion. BTAMe displays a similar $\Delta G^{\ominus}$ trend, i.e., the formation of $[Cu(L)_2]^{+}$ is exergonic by −0.3 eV, whereas the formation of $[Cu(L)_4]^{2+}$ is endergonic by 0.1 eV.

Such a trend is also observed in the case of BTAH, where the formation of $[Cu(L)_2]^{+}$ is exergonic by −0.2 eV, whereas the formation of $[Cu(L)_4]^{2+}$ is endergonic by 0.2 eV. For the other considered benzazole molecules, the formation of $[Cu(L)_2]^{+}$ and $[Cu(L)_4]^{2+}$ is exergonic; $\Delta G^{\ominus}$values for the formation of $[Cu(L)_2]^{+}$ range from −0.20 to −0.50 eV and that for $[Cu(L)_4]^{2+}$ from −0.06 to −0.81 eV. BTAH-6COOH is the only investigated

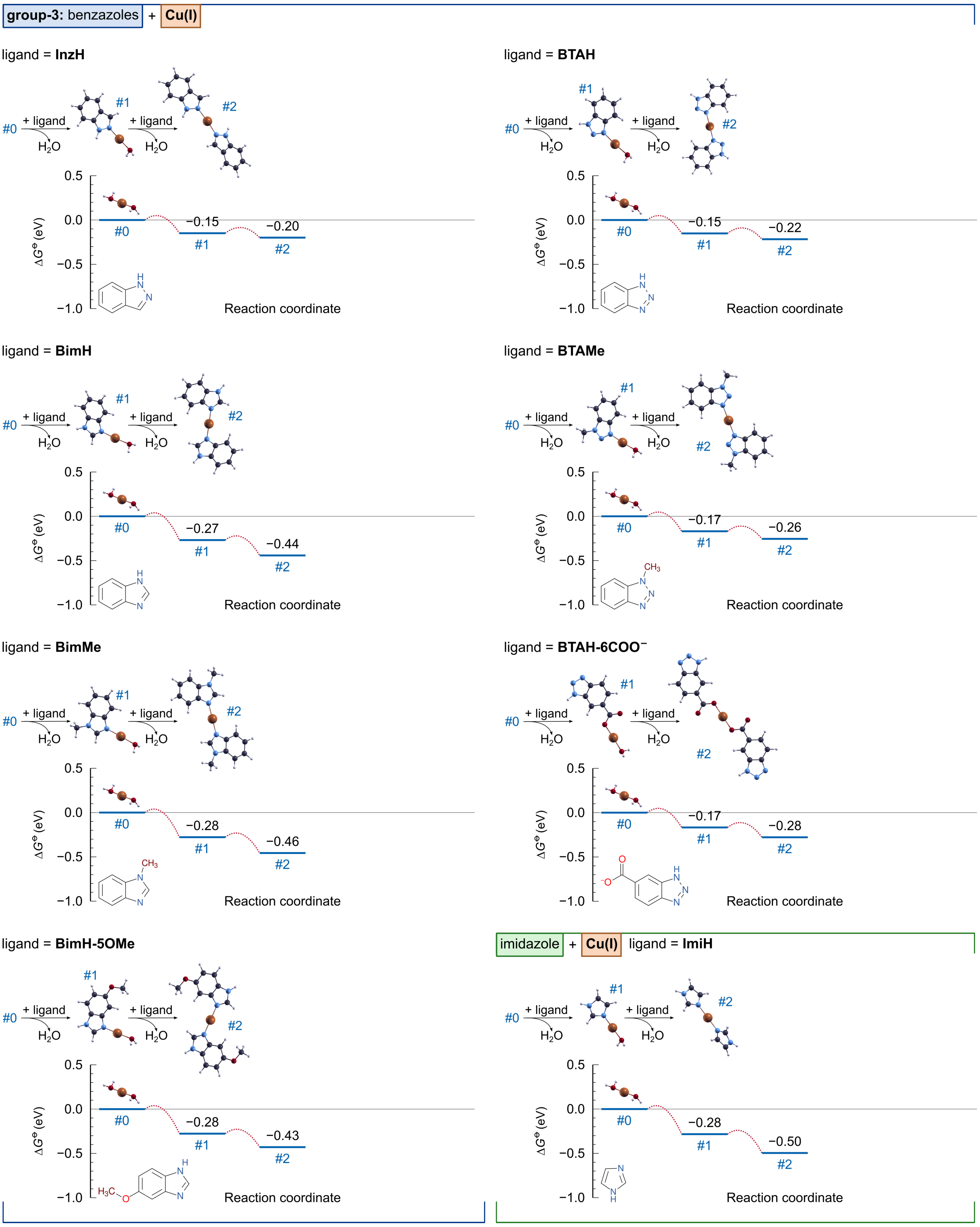

Figure 5.8: Standard reaction Gibbs energy ($\Delta G^{\ominus}$) profiles for the formation of $[\mathrm{Cu(L)_2}]^+$ ($[\mathrm{Cu(L)_2}]$ in the case of BTAH-6COO$^-$ ligand) complexes from hydrated Cu(I) for investigated benzazoles and imidazole ligands.

molecule that is not the stablest in the neutral form at pH = 7 in aqueous solutions, where BTAH-6COO$^-$ is instead the stablest. The BTAH-6COO$^-$ ligand is also able to complexate Cu ions via heterocyclic N3 atom (for enumeration of atoms see Figure 4.20) and the O atom from the carboxylate group. From the results shown in Figure C.2,

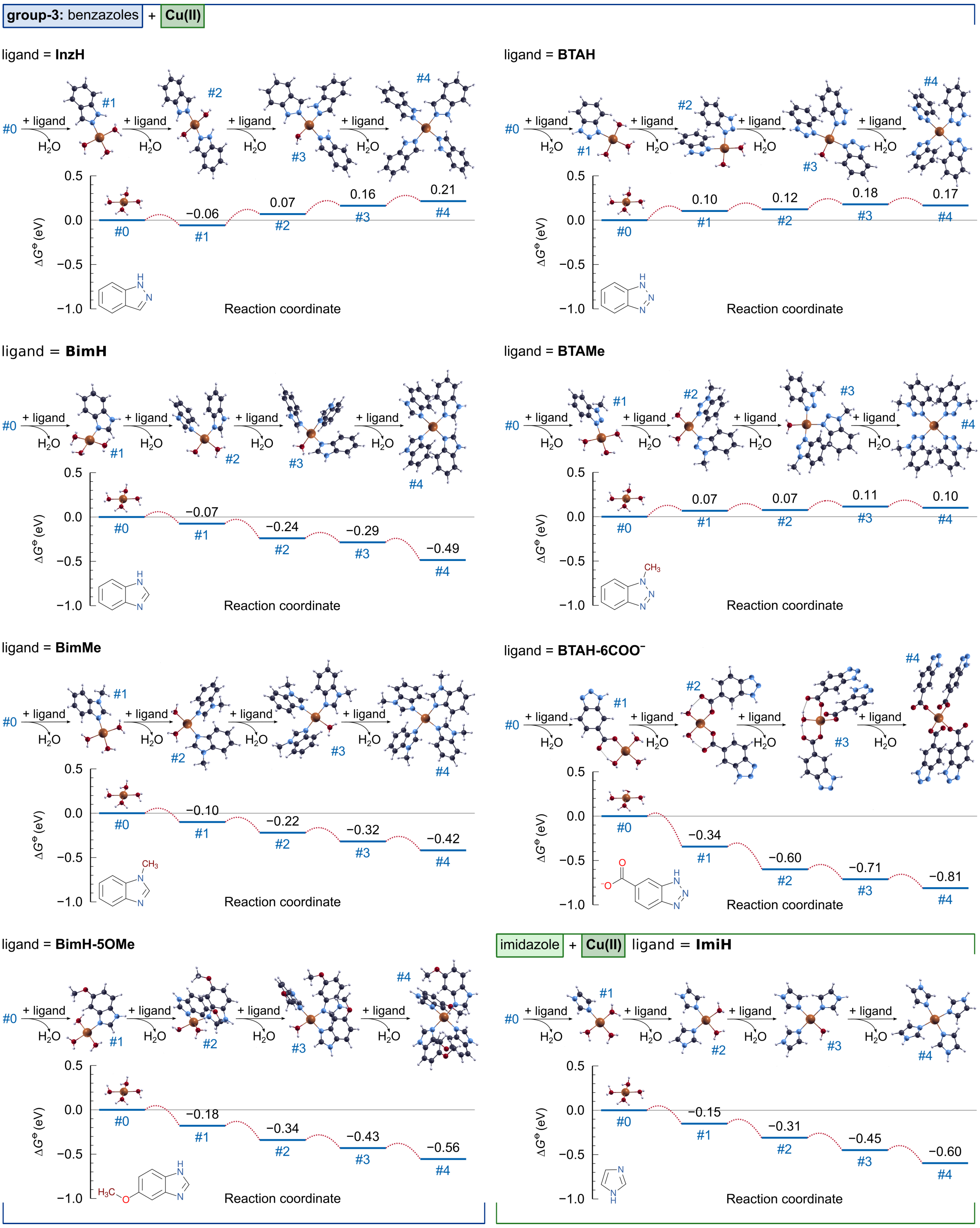

Figure 5.9: Standard reaction Gibbs energy ($\Delta G^{\ominus}$) profiles for the formation of $[\mathrm{Cu(L)_4}]^{2+}$ ($[\mathrm{Cu(L)_4}]^{2-}$ in the case of BTAH-6COO$^-$ ligand) complex formation for investigated benzazoles and imidazole ligands.

it can be concluded that the formation of Cu(I) coordination complexes is exergonic by about 0.3 eV regardless of the atom involved in the Cu–L bond. Among the considered N-heterocyclic ligands, BTAH-6COO$^-$ forms the most stable complexes with Cu(II); the $\Delta G^{\ominus}$ value for the formation of $[\mathrm{Cu(L)_4}]^{2+}$ from hydrated Cu(II) is −0.8 eV. Based on this value, the Boltzmann distribution[1] of $[Cu(H_2O)_4]^{2+}$ vs. $[Cu(BTAH\text{-}COO)_4]^{2-}$ is 1 vs. $5 \cdot 10^{13}$, indicating a complete transformation of hydrated Cu(II) into $[Cu(BTAH\text{-}6COO)_4]^{2-}$. In contrast, the $[Cu(BTAH\text{-}6COO)_4]^{2-}$ complex, where the BTAH-6COO$^-$ ligand bonds to Cu(II) with the N atom is 0.95 eV less stable compared to the O-bonded complex (cf. Figure C.5). Further, BTAH-COO$^-$ can also act as a bidentate ligand (Figure C.6), substituting two water molecules and forming two dative Cu–O bonds. The standard reaction Gibbs energy for the formation of the $[Cu(BTAH\text{-}6COO)_2]$ chelate from hydrated Cu(II) is −0.6 eV, implying that the monodentate $[Cu(BTAH\text{-}COO)_4]^{2-}$ complex is by 0.25 eV more stable.

Finally, structures and $\Delta G^{\ominus}$ reaction profiles for the complex formation with ImiH via pyridine-type N atom are shown in Figure 5.8 and Figure 5.9 for Cu(I) and Cu(II) central ions, respectively. Our results show ImiH can substitute water molecules from the first solvation shell of hydrated Cu(I) and Cu(II) and can form the $[Cu(ImiH)_2]^+$ and $[Cu(ImiH)_4]^{2+}$ coordination complexes. The standard reaction Gibbs energies for the formation of the two complexes from hydrated Cu(I) and Cu(II) are −0.5 and −0.6 eV, respectively.

5.4 Scrutinizing the $\Delta G^{\ominus}$ Trends

The correlation between standard reaction Gibbs energies for the formation of $[Cu(L)_2]^+$ and $[Cu(L)_4]^{2+}$ complexes from the hydrated Cu(I) and Cu(II) ions is shown in Figure 5.10 for all considered molecular ligands and Cl$^-$. There is a moderate correlation between the $\Delta G^{\ominus}$ values for Cu(I) and Cu(II) complexes, with the coefficient of determination (R^2) of 0.88, implying that a strong interaction of a ligand with Cu(I) likely also results in strong interaction with Cu(II) and vice-versa.

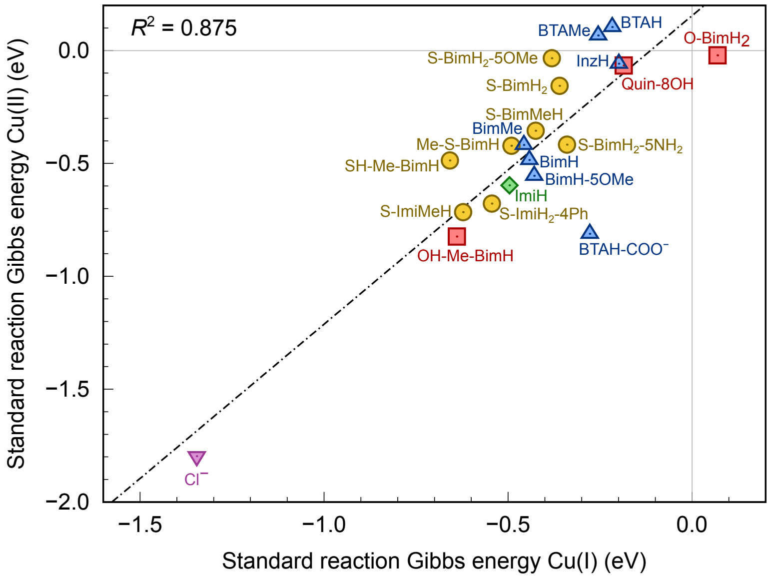

Figure 5.10: For all examined ligands (N-heterocyclic molecules and Cl$^-$ ion), a linear relationship with the coefficient of determination $R^2 = 0.875$ is observed between the standard complexation Gibbs energies for the complexation with the Cu(I) and Cu(II) central ions.

---

[1] The Boltzmann distribution between two species at a given temperature is calculated as $N_i/N_j = \exp[(G_j - G_i)/k_\mathrm{B}T]$, where G_j and G_j are the Gibbs energies of the two species, whereas $k_\mathrm{B}T$ is 26 meV at room temperature.

The prediction of inhibition efficiency of corrosion inhibitors using machine learning approaches is gaining popularity. A prerequisite for building a predictive and robust model is to use (i) a sufficient set of data and (ii) a sound selection of molecular descriptors to train the underlying machine-learning models. The latter attracted our attention, hence we wanted to investigate if there is any correlation between the calculated ΔG° values and the measured inhibition efficiency of our set of molecules. The calculated ΔG° could account for a more sophistically composed descriptor, taking into account not only the intrinsic properties of a molecule but also its interaction with the metal ions.

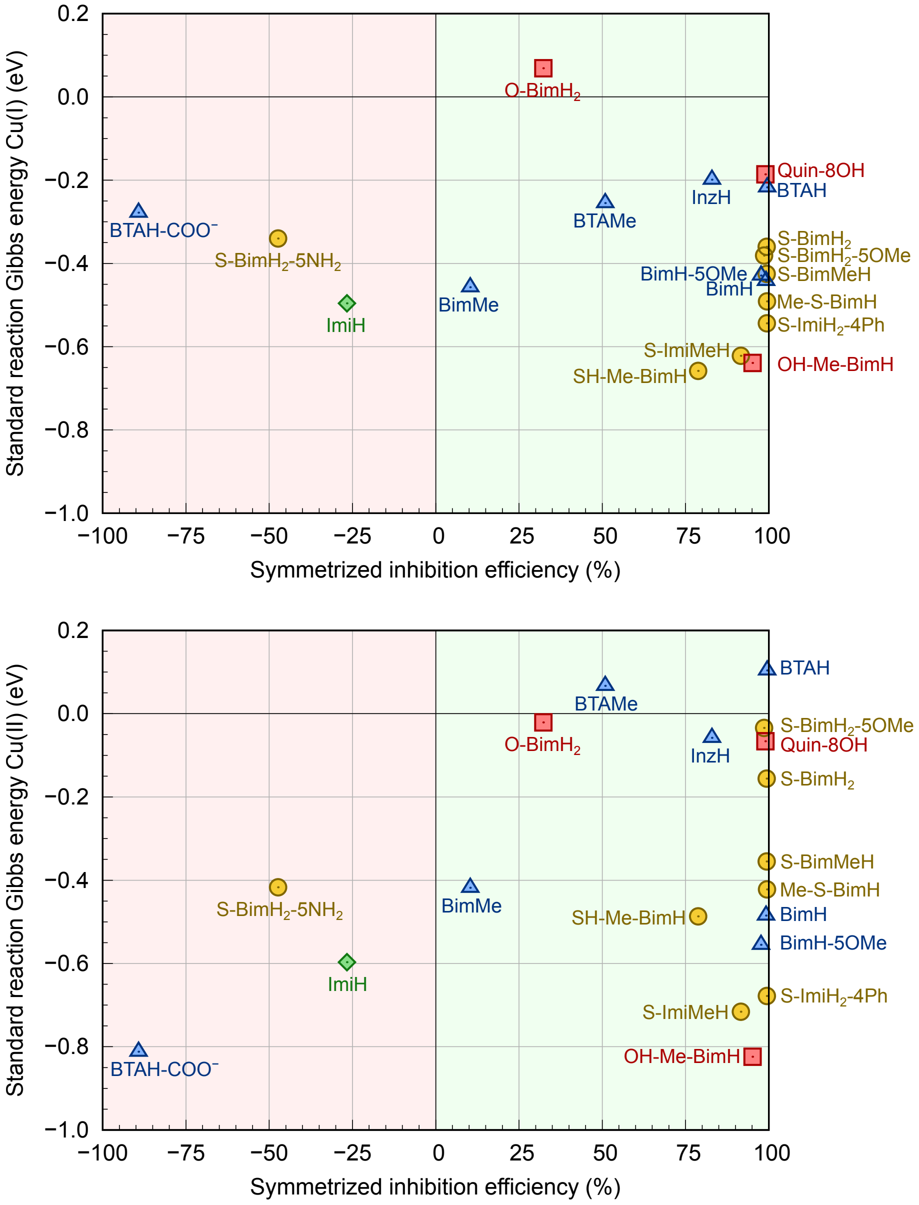

Figure 5.11: Correlations (or a lack thereof) between the symmetrized inhibition efficiency and the standard reaction Gibbs energy for the formation of Cu(I) [top] and Cu(II) [bottom] coordination complexes. A wide vertical distribution of data around the 100% inhibition efficiency can be observed. This implies that a good corrosion inhibitor can have practically any value of the standard reaction Gibbs energy of the complex formation with Cu ions. The experimental inhibition efficiency data are taken from Ref. [54].

In Figure 5.11, the symmetrized inhibition effciency ($\mathrm{IE}_{\mathrm{sym}}$) is used, which is defined as [106]:

$$\mathrm{IE}_{\mathrm{sym}}(\mathrm{IE}) = \begin{cases} \dfrac{100 \cdot \mathrm{IE}}{100 - \mathrm{IE}} & \text{for IE} \in (-\infty, 0) \\ \mathrm{IE} & \text{for IE} \in [0, 100], \end{cases} \tag{5.9}$$

where IE is the usual inhibition efficiency. Figure 5.11 reveals neither $\Delta G^{\ominus}(\mathrm{Cu(I)})$ nor $\Delta G^{\ominus}(\mathrm{Cu(II)})$ display any noticeable correlation with $\mathrm{IE}_{\mathrm{sym}}$. A large scattering of data is observed in lieu of desired correlation. Nevertheless, considering the observed computational data and known inhibition efficiency measurements, let us look at two most notable examples from the bottom chart of Figure 5.11:

BTAH vs. BTAH-6COO$^-$: BTAH with its inhibition efficiency of 99.5%, is an excellent corrosion inhibitor for copper. According to our calculations, neutral BTAH does not form stable complexes with either Cu(I) or Cu(II). At room temperature, the latter is around 16,000-times more likely to be present as hydrated Cu(II) than $[\mathrm{Cu(BTAH)_4}]^{2+}$. Therefore, neutral BTAH prefers to interact directly with copper surfaces, thereby protecting them rather than forming a complex with solvated Cu(II) ions in the solution.

On the other hand, its derivative, BTAH-6COO$^-$ with $\mathrm{IE}_{\mathrm{sym}}$ of −89.2% shows the opposite effect—it accelerates the corrosion of copper, acting similarly to Cl$^-$. Relying on the results for the $[\mathrm{CuCl_4}]^{2-}$ complex ($\Delta G^{\ominus} = -1.8$ eV) and the premise that corrosion accelerators form stable soluble complexes with metal ions, one could argue the formation of a highly stable soluble $[\mathrm{Cu(BTAH\text{-}6COO)_4}]^{2-}$ complex ($\Delta G^{\ominus} = -0.8$ eV) is the reason for BTAH-6COOH accelerating the corrosion.

S-BimH$_2$ vs. S-BimH-NH$_2$: Mercapto-azoles usually exist in thione tautomer form, allowing them to form complexes with Cu(I) and Cu(II) via bonding with the S atom. Many mercapto-azoles are used as corrosion inhibitors for copper. In particular, S-BimH$_2$ is a good inhibitor with inhibition efficiency 99.3%, whereas its derivative with amino group attached to a benzene ring, S-BimH$_2$-5NH$_2$ gives $\mathrm{IE}_{\mathrm{sym}} = -47.3\%$. While the formation of $[\mathrm{Cu(L)_4}]^{2+}$ complexes is exergonic for both molecules, the value for S-BimH$_2$ of −0.2 eV is significantly less exergonic than the value of −0.4 eV for S-BimH$_2$-5NH$_2$. Hence, at room temperature, S-BimH$_2$-5NH$_2$ is around 22,000-times more likely to form solvated complexes with Cu(II).

These cherry-picked examples suggest corrosion activators display a higher affinity to form soluble complexes than corrosion inhibitors. However, one must be careful with this inference because Figure 5.11 shows no correlation between the standard reaction Gibbs energy of coordination-complex formation and inhibition efficiency.

Chapter 6

Conclusions

In this thesis, molecular modeling approach using density-functional theory methods was utilized to perform adsorption calculations on Cu(111) in vacuum and for investigating the stability of the coordination complexes between inhibitor molecules and copper ions in the aqueous medium using the cluster/continuum model where aqueous solvent was described by a few explicit water molecules and the surrounding water treated implicitly using the SMD imlicit solvent model.

The effect of chemisorbed H, O, OH, and Cl on the adsorption of imidazole on Cu(111) was scrutinized considering the role of the coverage, the type of $X_{(ads)}$ species, and the distance between imidazole and $X_{(ads)}$. The analysis of the obtained results indicate that with respect to the lateral intersite distance between X adsorbed onto an fcc site and imidazole adsorbed on a top site at the copper surface, imidazole top sites can be classified into three regions:

(i) Pauli repulsion region, consisting of the nearest-neighbor top-sites, where imidazole either cannot adsorb (for X = O, OH, and Cl) or is significantly hindered (for H);

(ii) local region, consisting of the second and third nearest-neighbor top-sites, where H-bonds between $X_{(ads)}$ and imidazole are possible; and

(iii) distant region consisting of sites that are further away and are therefore too far for hydrogen bonds to form.

The effect of $X_{(ads)}$ on adsorption of imidazole usually diminishes with the increasing imidazole–$X_{(ads)}$ distance and with the decreasing coverage of $X_{(ads)}$. Among the considered $X_{(ads)}$ species, $O_{(ads)}$ displays the strongest and the most stabilizing effect on the adsorption of imidazole (at high $O_{(ads)}$ coverage of about 1/2 ML, adsorbed imidazole can be stabilized by about 0.7 eV). $Cl_{(ads)}$ also stabilizes adsorption of imidazole but only up to about 0.3 eV, provided that the Cl coverage is not too high. In contrast, $H_{(ads)}$ has almost no effect, and $OH_{(ads)}$ usually diminishes the adsorption bonding of imidazole, except for the most stable cases where it displays a negligible effect. Among the four considered $X_{(ads)}$ species, the non-dissociatice adsorption of imidazole is, therefore, the most affected by $O_{(ads)}$ and $Cl_{(ads)}$. While both can enhance the adsorption bonding of imidazole, there is nevertheless a remarkable difference between the two. In particular, the critical $X_{(ads)}$ coverage where the chemisorption of imidazole is blocked is much lower for $Cl_{(ads)}$ than for $O_{(ads)}$, i.e., about 1/3 ML for $Cl_{(ads)}$ and about 2/3 ML for $O_{(ads)}$. While Cl prefers to form the high-coverage 1/3 ML $(\sqrt{3} \times \sqrt{3})R30°$–Cl/Cu(111) structure that, according to our results, blocks the chemisorption of imidazole, oxygen is prone to form either 1/4 ML or 1/3 ML O/Cu(111) chemisorbed phases that both enhance the adsorption of imidazole.

These considerations suggest that under real circumstances, the probability of enhancing the adsorption of imidazole is much higher for $O_{(ads)}$ than for $Cl_{(ads)}$. Our findings confirm our first hypothesis, that chemisorbed species such as H, O, OH, and Cl influence the adsorption bonding of imidazole on Cu(111).

The second hypothesis, which focuses on the nature and extent of co-adsorbed species on the adsorbed inhibitor molecules, was also confirmed. Moreover, we demonstrated that $X_{(ads)}$ species affect the adsorption of imidazole in three different ways:

(i) Via modification of the surface work function, which consequently affects the molecule–surface bonding. This is a global effect that depends linearly on the coverage of $X_{(ads)}$ and can either stabilize or destabilize the adsorbed azole molecule.

(ii) Chemisorbed species, such as O and OH, can form stabilizing hydrogen bonds with adsorbed azole molecules.

(iii) Chemisorbed O and Cl induce an enhancement of the N–Cu bond between adsorbed imidazole and the surface, provided that imidazole is adsorbed close enough to $X_{(ads)}$. This effect decreases with decreasing coverage of $X_{(ads)}$, but does not vanish at zero coverage, i.e., it persists even when imidazole is adsorbed near a single adsorbed $X_{(ads)}$.

As an aftermath of the effect (ii), i.e., once the hydrogen bond between adsorbed azole and nearby $O_{(ads)}$ or $OH_{(ads)}$ is formed, the adsorbed molecule can be further stabilized by deprotonation that involves a proton shift from the molecule to chemisorbed O or OH. We thus scrutinized how chemisorbed O and OH help deprotonating benzotriazole and imidazole on Cu(111). We found that the O and OH induced stabilization of molecular adsorption is twofold:

(i) $X_{(ads)}$ can enhance adsorption bonding of intact azole molecules (the ΔE_b contribution); for both imidazole and benzotriazole, $O_{(ads)}$ displays more stabilizing ΔE_b than $OH_{(ads)}$.

(ii) The adsorbed molecules are further stabilized by deprotonation (the ΔE_{deprot} contribution) that involves a proton shift from the molecule to the nearby $O_{(ads)}$ or $OH_{(ads)}$.

We confirmed our deduction from the third hypothesis that chemisorbed O and OH promote the dissociative adsorption of imidazole and benzotriazole. Furthermore, we demonstrated that the investigated O and OH promote the dissociative adsorption of imidazole and benzotriazole, leading to a stronger bonding of the inhibitor molecule. Deprotonation of adsorbed benzotriazole investigated herein proceeds via the N–H bond cleavage. The $O_{(ads)}$ or $OH_{(ads)}$ induced total stabilization ($\Delta E_b + \Delta E_{deprot}$) is stronger for BTAH than for ImiH. It reaches the magnitude of about 1.0 eV for benzotriazole on Cu(111) covered with either O or OH, and about 0.4 and 0.1 eV for imidazole on O/Cu(111) and OH/Cu(111), respectively. The increased stability of adsorbed molecules exponentially increases their persistence on surfaces. This observation is relevant in the context of corrosion inhibition because inhibitor molecules must persist on the surface to inhibit corrosion. For BTAH, dissociative adsorption energies reach the value of about -1.8 eV on O/Cu(111) and OH/Cu(111), which is a value strong enough to make the adsorption of BTAH irreversible (within the human time-frame) at room temperature.

The formation of coordination complexes in aqueous solutions and their thermodynamic stability was scrutinized. Based on our findings we can confirm our fourth hypothesis, which states that most of the 19 investigated N-heterocyclic molecules can form stable complexes with Cu(I) or Cu(II) ions. The structures of these complexes differ based on the central ion incorporated in the structure. Cu(I) coordinates with two ligands forming a linear complex, whereas the Cu(II) coordinate with four ligands in a square planar geometry. Generally, from a thermodynamic perspective, at least one elementary reaction step for all considered molecules in the substitution of water molecules from the first solvation shell around copper ions with the investigated ligands is exergonic, which makes the coordination complexes plausible. In the case of Cu(I), all reaction steps for all ligands are exergonic, except for O-BimH$_2$, where both elementary steps are endergonic. This indicates that the ketone group is unlikely to form coordination complexes with Cu(I). A similar observation was made when the O-BimH$_2$ ligand interacted with the Cu(II) ion. The formation of Cu(II)-complexes is more perplexing in nature. Although most of the investigated inhibitor molecules can form stable 4-coordinated complexes with at least one non-water ligand, BTAH and BTAMe are not thermodynamically likely to form coordinative bonds with the Cu(II) ion. For molecules which do not form soluble coordination complexes, one would expect that they would be efficient corrosion inhibitors. However, this deduction cannot be substantiated with the data presented in this thesis due to a lack of correlation between the calculated standard reaction Gibbs energies for the formation of coordination complexes and the experimentally measured inhibition efficiencies.

The presented thesis lays the groundwork for further research activities. In particular, the coadsorption study presented herein is—to the best of our knowledge—the first that systematically investigates coadsorption effects between $X_{(ads)}$ species and corrosion inhibitors. Consequently, *in vacuo* calculations were performed for simplicity. However, in the context of corrosion, the effects of the aqueous solvent are essential. Therefore, the description of the aqueous solvent is among the first extensions of the current study that will give more relevant insight into the interfacial behavior of inhibitors at the solid/solvent interfaces.

Our calculations show that inhibitors can deprotonate upon adsorption, thus significantly altering their molecular fingerprint descriptors. Likewise, the calculated standard Gibbs energies of formation for coordination complexes can be used as descriptors in machine-learning models. Although these standard Gibbs energies of formation do not directly correlate with experimentally determined inhibition efficiency, they can be usable in combination with other descriptors. Therefore, the approaches presented in this thesis have the potential to provide valuable descriptors for machine-learning models because they describe not only intrinsic inhibitor molecular properties but also characteristics of the metallic material to be protected.

In conclusion, the presented thesis emphasizes the importance of molecular modeling to tackle the challenges associated with corrosion inhibitors. It provides new fundamental knowledge and a deeper understanding of aspects that are relevant in finding better corrosion inhibitors.

Appendix A

Species Distribution Charts

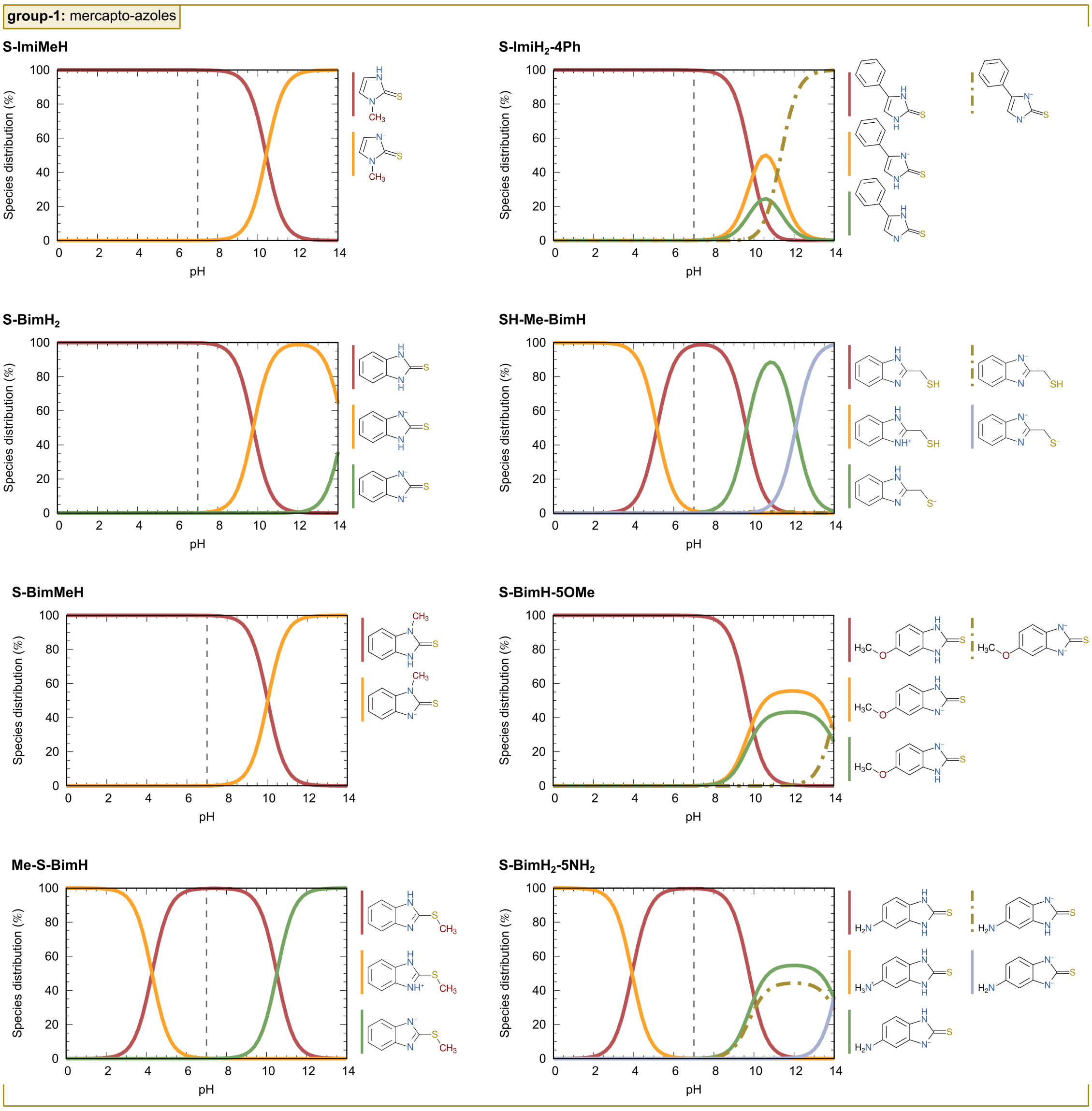

Figure A.1: Species distribution charts calculated with the MavinSketch program. Eight different molecules containing mercapto group (Group 1) are considered.

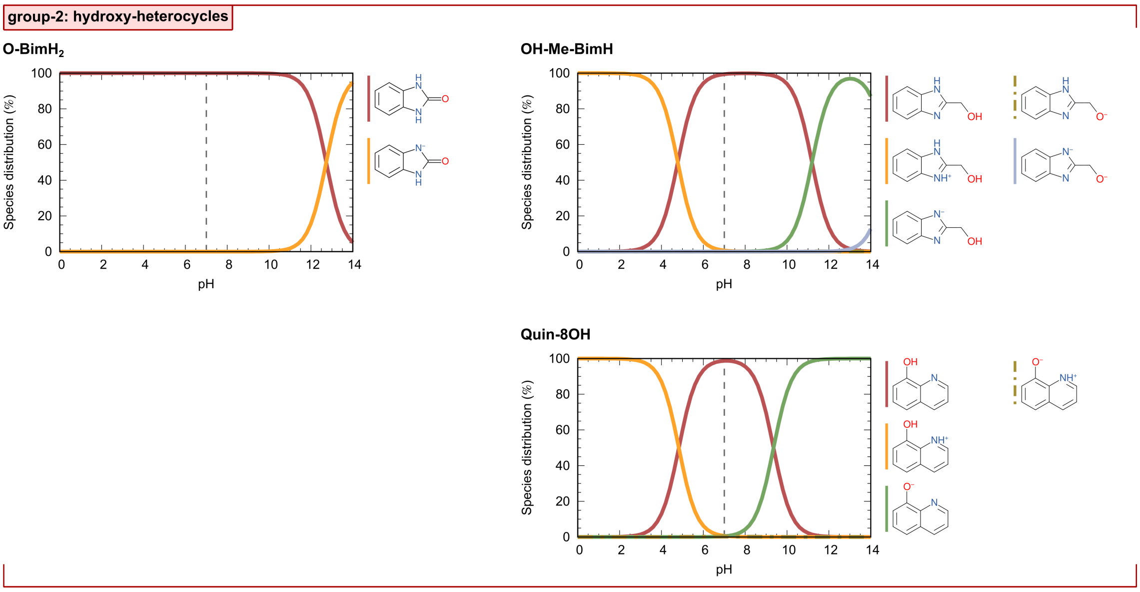

Figure A.2: Species distribution charts calculated with the MavinSketch program. Three different molecules containing hydroxyl group (Group 2) are considered.

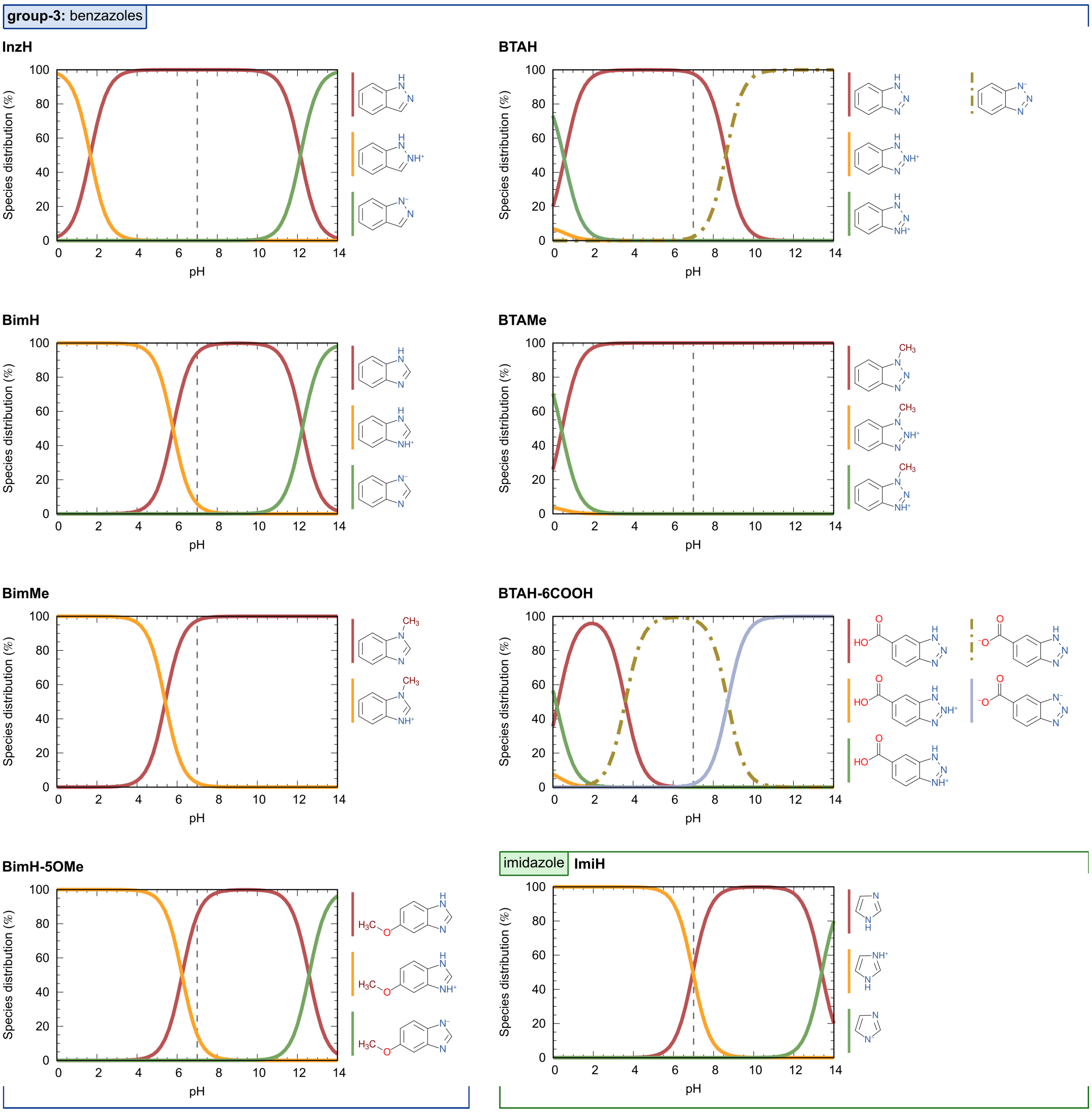

Figure A.3: Species distribution charts calculated with the MavinSketch program. Seven different benzazoles (Group 3) are considered. Species distribution chart for imidazole is also shown.

Appendix B

Snapshots of Different Configurations

In the following appendix, 87 snapshots of different configurations for evaluating the effect of coadsorption for all considered $X_{(ads)}$ are presented for illustrative purposes. Depicted structures correspond to (4×4)–Cu(111) with one $ImiH_{(ads)}$ and one $X_{(ads)}$ per supercell. Similar configurations were investigated also on other considered supercells, but are not shown herein.

B.1 ImiH @ (4×4)–H/Cu(111) Configurations

`Cu111-4x4-ImiH-Hfcc-blue-1-4L`

optimized structure

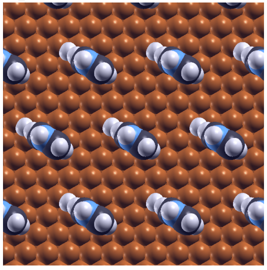

E_{tot}=−5688.209994 ryd

`Cu111-4x4-ImiH-Hfcc-blue-2-4L`

optimized structure

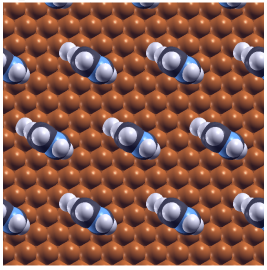

E_{tot}=−5688.210484 ryd

`Cu111-4x4-ImiH-Hfcc-blue-3-4L`

optimized structure

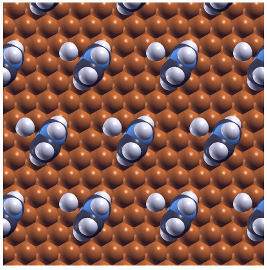

E_{tot}=−5688.209865 ryd

`Cu111-4x4-ImiH-Hfcc-blue-4-4L`

optimized structure

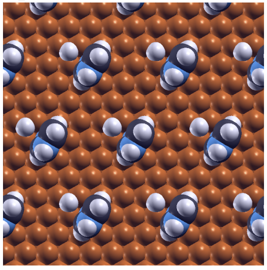

E_{tot}=−5688.209865 ryd

`Cu111-4x4-ImiH-Hfcc-yellow-1-4L`

optimized structure

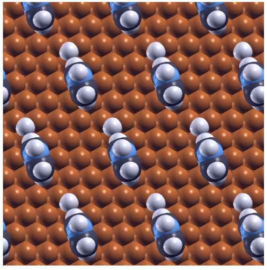

E_{tot}=−5688.210331 ryd

`Cu111-4x4-ImiH-Hfcc-yellow-2-4L`

optimized structure

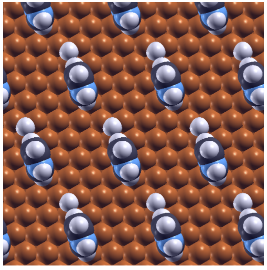

E_{tot}=−5688.210607 ryd

`Cu111-4x4-ImiH-Hfcc-yellow-3-4L`

optimized structure

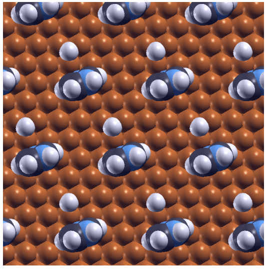

E_{tot}=−5688.210686 ryd

`Cu111-4x4-ImiH-Hfcc-yellow-4-4L`

optimized structure

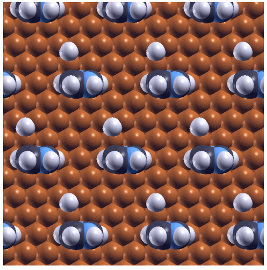

E_{tot}=−5719.185078 ryd

`Cu111-4x4-ImiH-Hfcc-yellow-5-4L`

optimized structure

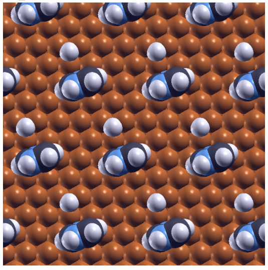

$E_{\text{tot}}=-5688.210193$ ryd

`Cu111-4x4-ImiH-Hfcc-yellow-6-4L`

optimized structure

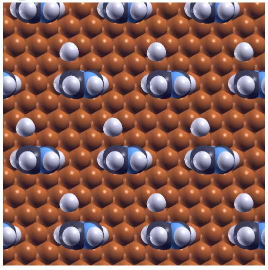

$E_{\text{tot}}=-5688.209745$ ryd

`Cu111-4x4-ImiH-Hfcc-green-1-4L`

optimized structure

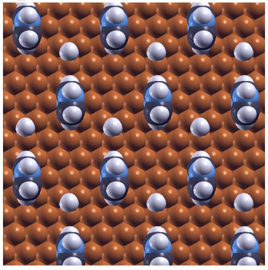

$E_{\text{tot}}=-5688.210556$ ryd

`Cu111-4x4-ImiH-Hfcc-green-2-4L`

optimized structure

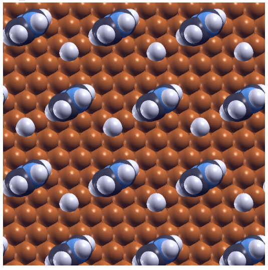

$E_{\text{tot}}=-5688.210957$ ryd

`Cu111-4x4-ImiH-Hfcc-green-3-4L`

optimized structure

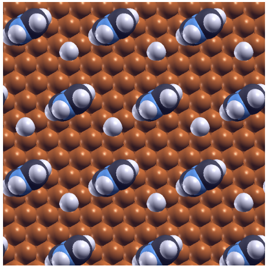

$E_{\text{tot}}=-5688.210556$ ryd

`Cu111-4x4-ImiH-Hfcc-green-4-4L`

optimized structure

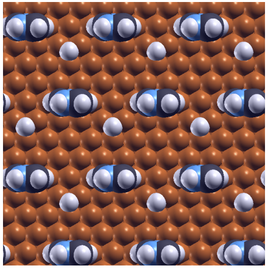

$E_{\text{tot}}=-5688.209522$ ryd

`Cu111-4x4-ImiH-Hfcc-green-5-4L`

optimized structure

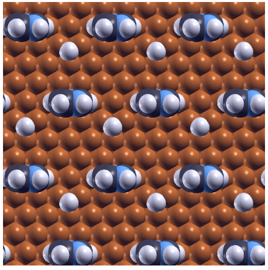

$E_{\text{tot}}=-5688.209941$ ryd

`Cu111-4x4-ImiH-Hfcc-salmon-1-4L`

optimized structure

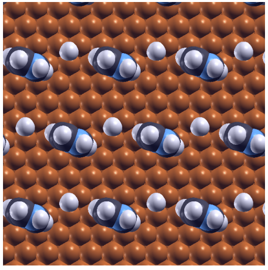

$E_{\text{tot}}=-5688.210362$ ryd

`Cu111-4x4-ImiH-Hfcc-salmon-2-4L`

optimized structure

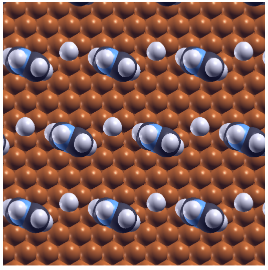

$E_{\text{tot}}=-5688.209801$ ryd

`Cu111-4x4-ImiH-Hfcc-salmon-3-4L`

optimized structure

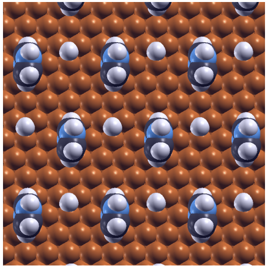

$E_{\text{tot}}=-5688.210278$ ryd

`Cu111-4x4-ImiH-Hfcc-salmon-4-4L`

optimized structure

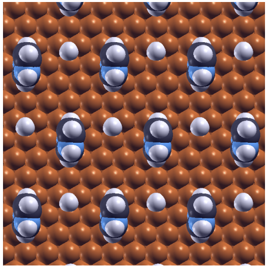

$E_{\text{tot}}=-5688.210491$ ryd

B.2 ImiH @ (4×4)–OH/Cu(111) Configurations

`Cu111-4x4-ImiH-OHfcc-blue-1-4L`

optimized structure

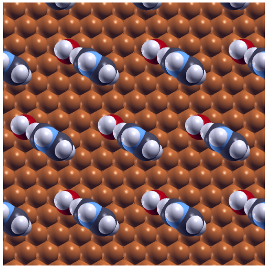

$E_{\text{tot}}=-5720.120427$ ryd

`Cu111-4x4-ImiH-OHfcc-blue-2-4L`

optimized structure

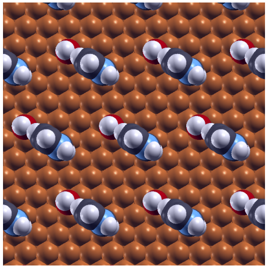

$E_{\text{tot}}=-5720.122171$ ryd

`Cu111-4x4-ImiH-OHfcc-blue-3-4L`

optimized structure

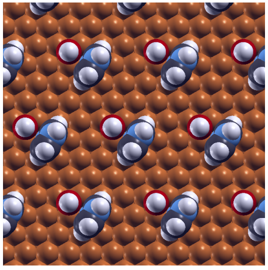

$E_{\text{tot}}=-5720.131334$ ryd

`Cu111-4x4-ImiH-OHfcc-blue-4-4L`

optimized structure

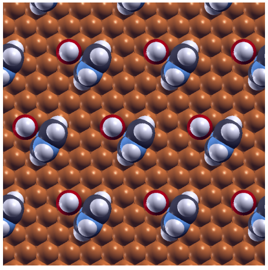

$E_{\text{tot}}=-5720.131273$ ryd

`Cu111-4x4-ImiH-OHfcc-blue-5-4L`

optimized structure

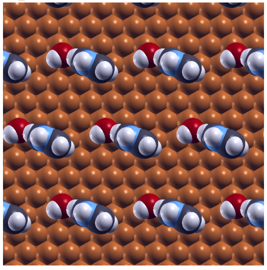

$E_{\text{tot}}=-5720.129380$ ryd

`Cu111-4x4-ImiH-OHfcc-blue-6-4L`

optimized structure

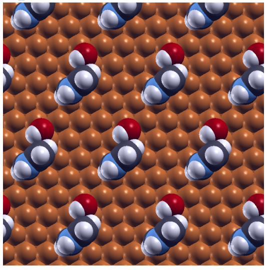

$E_{\text{tot}}=-5720.122441$ ryd

`Cu111-4x4-ImiH-OHfcc-blue-7-4L`

optimized structure

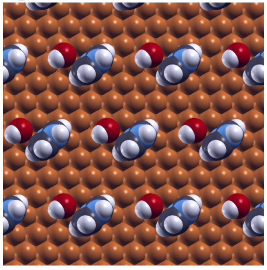

$E_{\text{tot}}=-5720.121385$ ryd

`Cu111-4x4-ImiH-OHfcc-blue-8-4L`

optimized structure

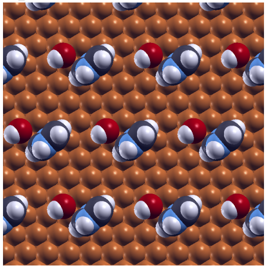

$E_{\text{tot}}=-5720.121944$ ryd

`Cu111-4x4-ImiH-OHfcc-blue-9-4L`

optimized structure

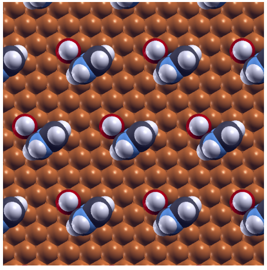

$E_{\text{tot}}=-5720.131545$ ryd

`Cu111-4x4-ImiH-OHfcc-blue-10-4L`

optimized structure

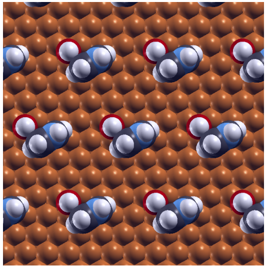

$E_{\text{tot}}=-5720.132538$ ryd

`Cu111-4x4-ImiH-OHfcc-yellow-1-4L`

optimized structure

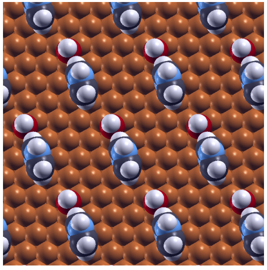

$E_{\text{tot}}=-5720.125806$ ryd

`Cu111-4x4-ImiH-OHfcc-yellow-2-4L`

optimized structure

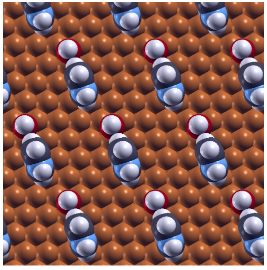

$E_{\text{tot}}=-5720.125120$ ryd

`Cu111-4x4-ImiH-OHfcc-yellow-3-4L`

optimized structure

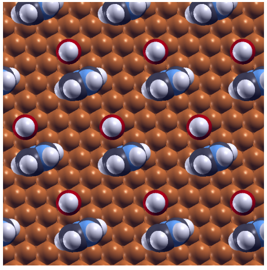

$E_{\text{tot}}=-5720.127866$ ryd

`Cu111-4x4-ImiH-OHfcc-yellow-4-4L`

optimized structure

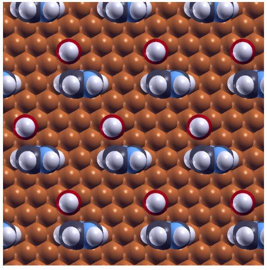

$E_{\text{tot}}=-5720.127060$ ryd

`Cu111-4x4-ImiH-OHfcc-yellow-5-4L`

optimized structure

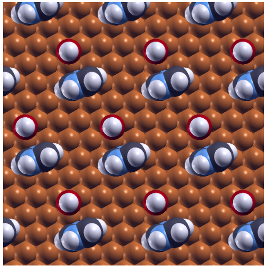

$E_{\text{tot}}=-5720.127378$ ryd

`Cu111-4x4-ImiH-OHfcc-yellow-6-4L`

optimized structure

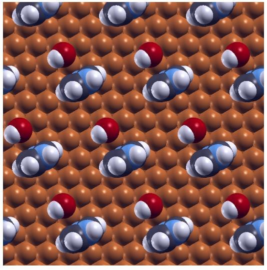

$E_{\text{tot}}=-5720.120389$ ryd

`Cu111-4x4-ImiH-OHfcc-yellow-7-4L`

optimized structure

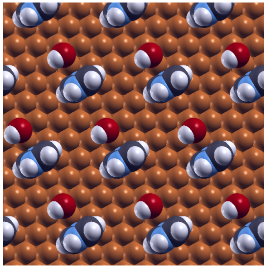

$E_{\text{tot}}=-5720.119631$ ryd

`Cu111-4x4-ImiH-OHfcc-yellow-8-4L`

optimized structure

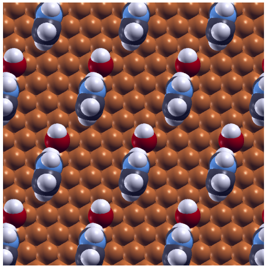

$E_{\text{tot}}=-5720.128207$ ryd

`Cu111-4x4-ImiH-OHfcc-salmon-1-4L`

optimized structure

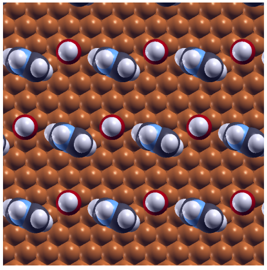

$E_{\text{tot}}=-5720.124562$ ryd

`Cu111-4x4-ImiH-OHfcc-salmon-2-4L`

optimized structure

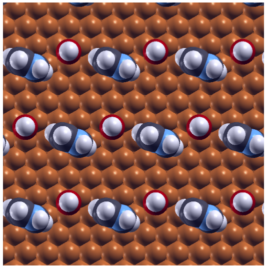

$E_{\text{tot}}=-5720.125202$ ryd

`Cu111-4x4-ImiH-OHfcc-salmon-3-4L`

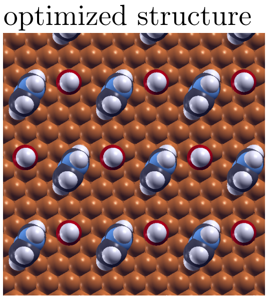

$E_{\text{tot}}=-5720.125850$ ryd

`Cu111-4x4-ImiH-OHfcc-salmon-4-4L`

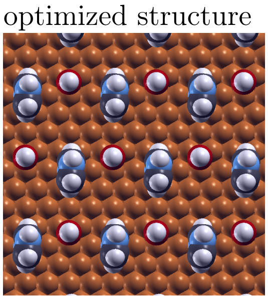

$E_{\text{tot}}=-5720.126052$ ryd

`Cu111-4x4-ImiH-OHfcc-green-1-4L`

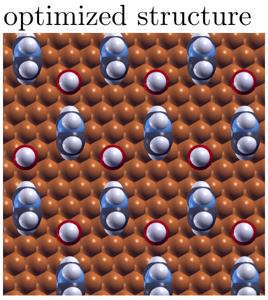

$E_{\text{tot}}=-5720.125907$ ryd

`Cu111-4x4-ImiH-OHfcc-green-2-4L`

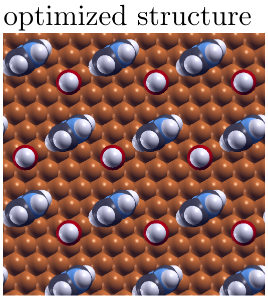

$E_{\text{tot}}=-5720.126399$ ryd

`Cu111-4x4-ImiH-OHfcc-green-3-4L`

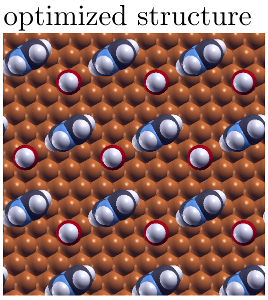

$E_{\text{tot}}=-5720.125957$ ryd

`Cu111-4x4-ImiH-OHfcc-green-4-4L`

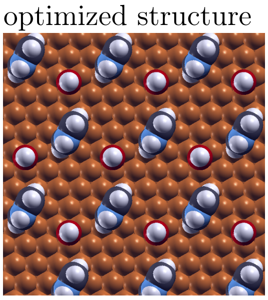

$E_{\text{tot}}=-5720.125420$ ryd

`Cu111-4x4-ImiH-OHfcc-green-5-4L`

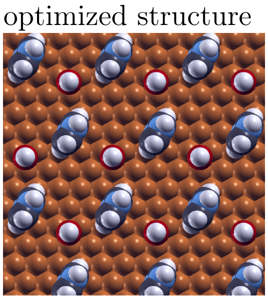

$E_{\text{tot}}=-5720.125520$ ryd

B.3 ImiH @ (4×4)–Cl/Cu(111) Configurations

`Cu111-4x4-ImiH-Clfcc-blue-1-4L`

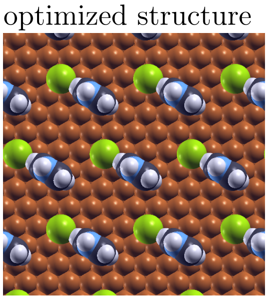

$E_{\text{tot}}=-5719.172443$ ryd

`Cu111-4x4-ImiH-Clfcc-blue-2-4L`

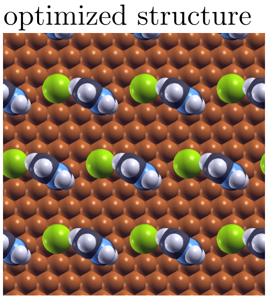

$E_{\text{tot}}=-5719.184609$ ryd

`Cu111-4x4-ImiH-Clfcc-blue-3-4L`

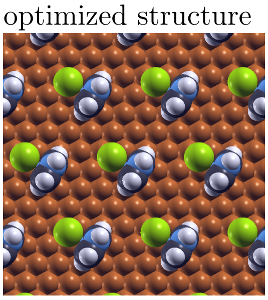

$E_{\text{tot}}=-5719.186248$ ryd

`Cu111-4x4-ImiH-Clfcc-blue-4-4L`

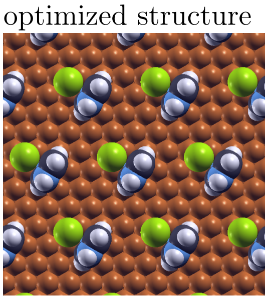

$E_{\text{tot}}=-5719.186241$ ryd

`Cu111-4x4-ImiH-Clfcc-blue-5-4L`

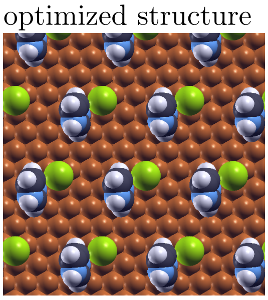

$E_{\text{tot}}=-5719.186834$ ryd

`Cu111-4x4-ImiH-Clfcc-yellow-1-4L`

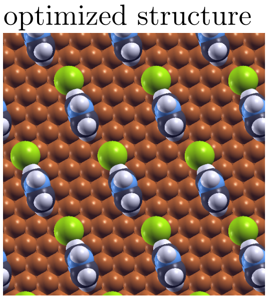

$E_{\text{tot}}=-5719.185766$ ryd

`Cu111-4x4-ImiH-Clfcc-yellow-2-4L`

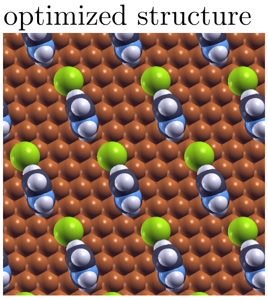

$E_{\text{tot}}=-5719.185134$ ryd

`Cu111-4x4-ImiH-Clfcc-yellow-3-4L`

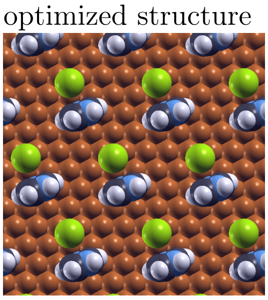

$E_{\text{tot}}=-5719.185539$ ryd

`Cu111-4x4-ImiH-Clfcc-yellow-4-4L`

optimized structure

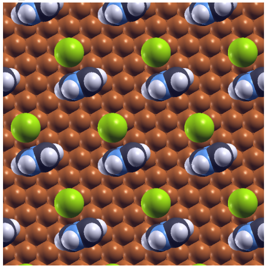

$E_{\mathrm{tot}} = -5719.185579$ ryd

`Cu111-4x4-ImiH-Clfcc-yellow-5-4L`

optimized structure

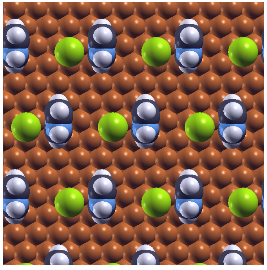

$E_{\mathrm{tot}} = -5719.186602$ ryd

`Cu111-4x4-ImiH-Clfcc-salmon-1-4L`

optimized structure

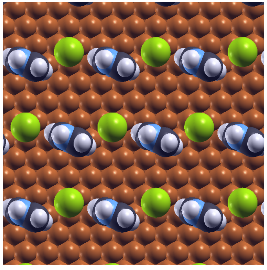

$E_{\mathrm{tot}} = -5719.185154$ ryd

`Cu111-4x4-ImiH-Clfcc-salmon-2-4L`

optimized structure

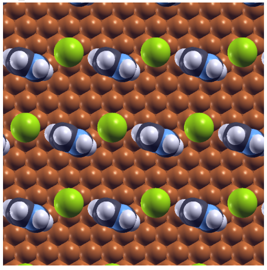

$E_{\mathrm{tot}} = -5719.185966$ ryd

`Cu111-4x4-ImiH-Clfcc-salmon-3-4L`

optimized structure

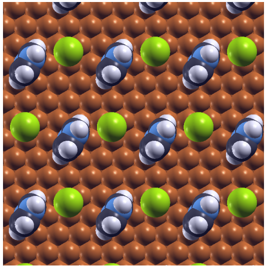

$E_{\mathrm{tot}} = -5719.184446$ ryd

`Cu111-4x4-ImiH-Clfcc-salmon-4-4L`

optimized structure

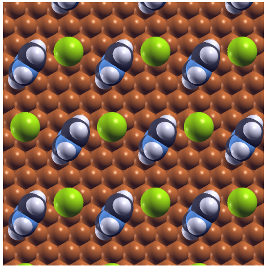

$E_{\mathrm{tot}} = -5719.183708$ ryd

`Cu111-4x4-ImiH-Clfcc-salmon-5-4L`

optimized structure

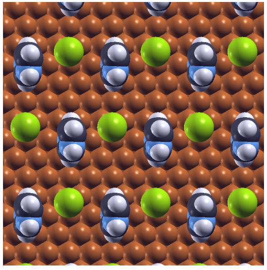

$E_{\mathrm{tot}} = -5719.183660$ ryd

`Cu111-4x4-ImiH-Clfcc-salmon-6-4L`

optimized structure

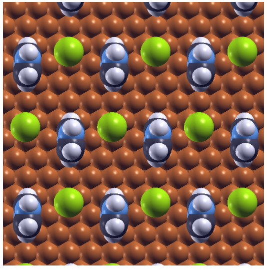

$E_{\mathrm{tot}} = -5719.183714$ ryd

`Cu111-4x4-ImiH-Clfcc-green-1-4L`

optimized structure

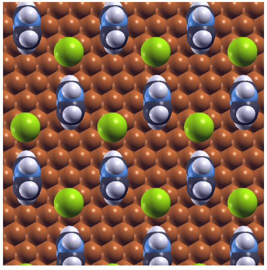

$E_{\mathrm{tot}} = -5719.184730$ ryd

`Cu111-4x4-ImiH-Clfcc-green-2-4L`

optimized structure

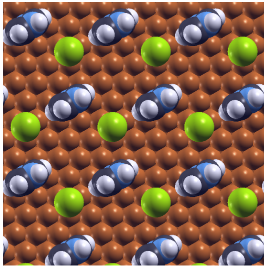

$E_{\mathrm{tot}} = -5719.184932$ ryd

`Cu111-4x4-ImiH-Clfcc-green-3-4L`

optimized structure

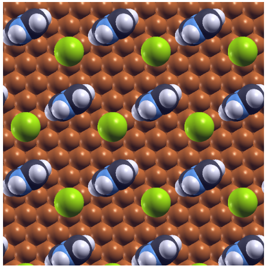

$E_{\mathrm{tot}} = -5719.184774$ ryd

`Cu111-4x4-ImiH-Clfcc-green-4-4L`

optimized structure

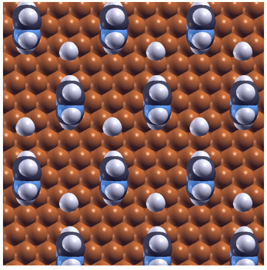

$E_{\mathrm{tot}} = -5688.210931$ ryd

`Cu111-4x4-ImiH-Clfcc-green-5-4L`

optimized structure

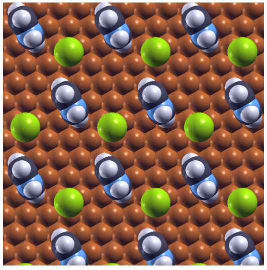

$E_{\mathrm{tot}} = -5719.183950$ ryd

`Cu111-4x4-ImiH-Clfcc-green-7-4L`

optimized structure

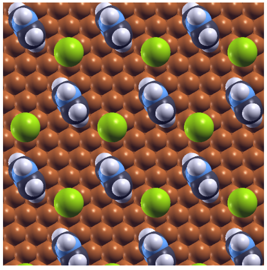

$E_{\mathrm{tot}} = -5719.183660$ ryd

B.4 ImiH @ (4×4)–O/Cu(111) Configurations

`Cu111-4x4-ImiH-Ofcc-blue-1-4L`

optimized structure

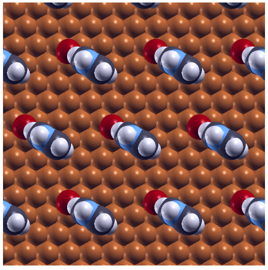

$E_{\text{tot}}=-5718.920980$ ryd

`Cu111-4x4-ImiH-Ofcc-blue-2-4L`

optimized structure

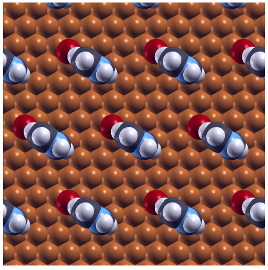

$E_{\text{tot}}=-5718.917207$ ryd

`Cu111-4x4-ImiH-Ofcc-blue-3-4L`

optimized structure

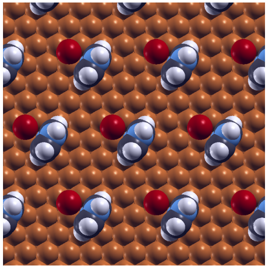

$E_{\text{tot}}=-5718.909780$ ryd

`Cu111-4x4-ImiH-Ofcc-blue-4-4L`

optimized structure

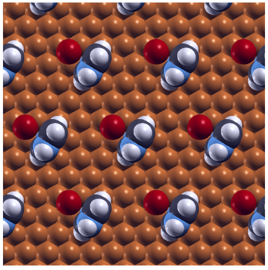

$E_{\text{tot}}=-5718.909791$ ryd

`Cu111-4x4-ImiH-Ofcc-yellow-1-4L`

optimized structure

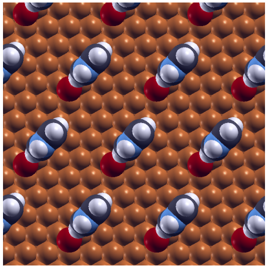

$E_{\text{tot}}=-5718.918082$ ryd

`Cu111-4x4-ImiH-Ofcc-yellow-2-4L`

optimized structure

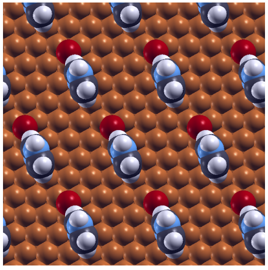

$E_{\text{tot}}=-5718.918528$ ryd

`Cu111-4x4-ImiH-Ofcc-yellow-3-4L`

optimized structure

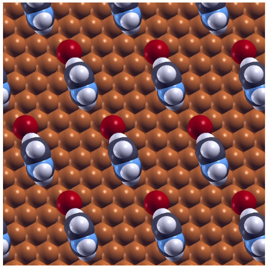

$E_{\text{tot}}=-5718.912828$ ryd

`Cu111-4x4-ImiH-Ofcc-yellow-4-4L`

optimized structure

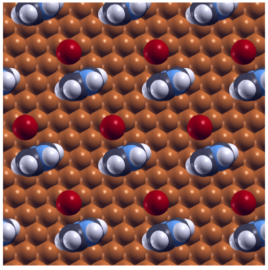

$E_{\text{tot}}=-5718.906304$ ryd

`Cu111-4x4-ImiH-Ofcc-yellow-5-4L`

optimized structure

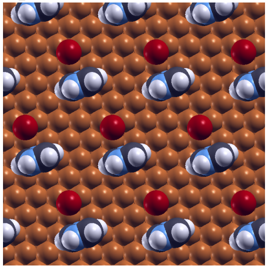

$E_{\text{tot}}=-5718.905943$ ryd

`Cu111-4x4-ImiH-Ofcc-yellow-6-4L`

optimized structure

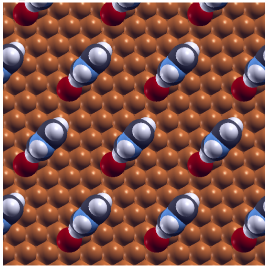

$E_{\text{tot}}=-5718.918082$ ryd

`Cu111-4x4-ImiH-Ofcc-salmon-1-4L`

optimized structure

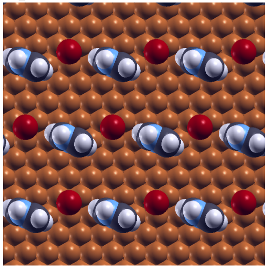

$E_{\text{tot}}=-5718.906212$ ryd

`Cu111-4x4-ImiH-Ofcc-salmon-2-4L`

optimized structure

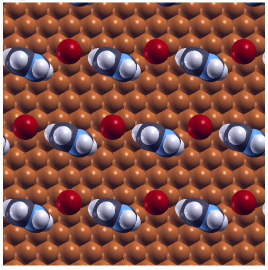

$E_{\text{tot}}=-5718.906950$ ryd

`Cu111-4x4-ImiH-Ofcc-green-1-4L`

optimized structure

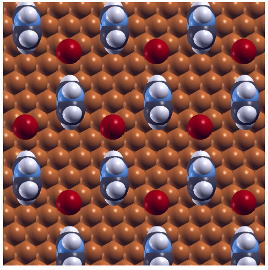

$E_{\text{tot}}=-5718.906066$ ryd

`Cu111-4x4-ImiH-Ofcc-green-2-4L`

optimized structure

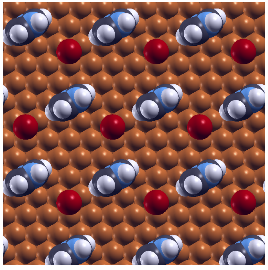

$E_{\text{tot}}=-5718.906521$ ryd

`Cu111-4x4-ImiH-Ofcc-green-3-4L`

optimized structure

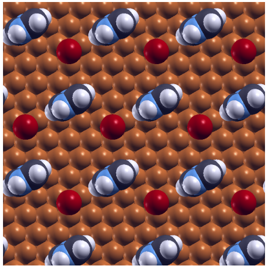

$E_{\text{tot}}=-5718.906068$ ryd

`Cu111-4x4-ImiH-Ofcc-green-4-4L`

optimized structure

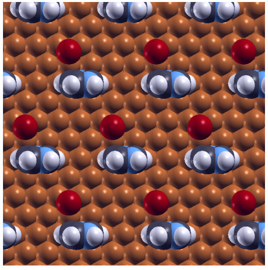

$E_{\text{tot}}=-5718.905554$ ryd

`Cu111-4x4-ImiH-Ofcc-green-5-4L` optimized structure 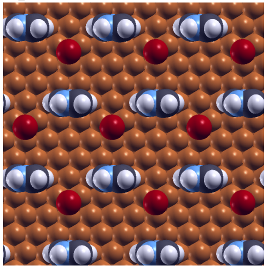 E_{tot}=−5718.904982 ryd	`Cu111-4x4-ImiH-Ofcc-green-6-4L` optimized structure 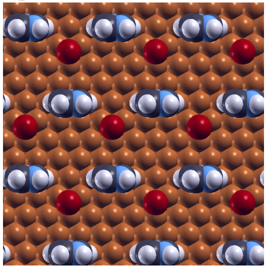 E_{tot}=−5718.905477 ryd	`Cu111-4x4-ImiH-Ofcc-green-7-4L` optimized structure 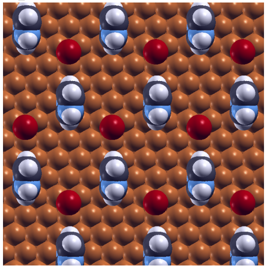 E_{tot}=−5718.906510 ryd	

Appendix C

Additional Cu–L Coordination Complexes

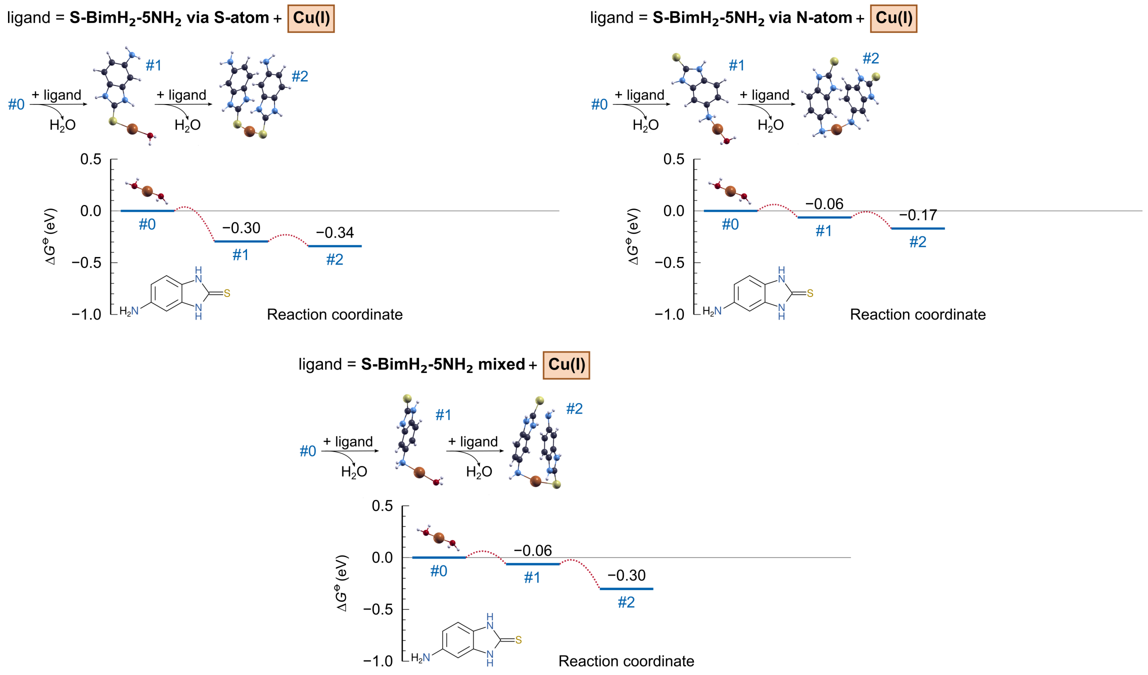

Figure C.1: Standard Gibbs energy ($\Delta G^{\ominus}$) reaction profiles for the formation of coordination complexes between the S-BimH_2-5NH_2 ligand and the Cu(I) ion. Different ligand bonding is considered, i.e., via S atom, N atom, and mixed.

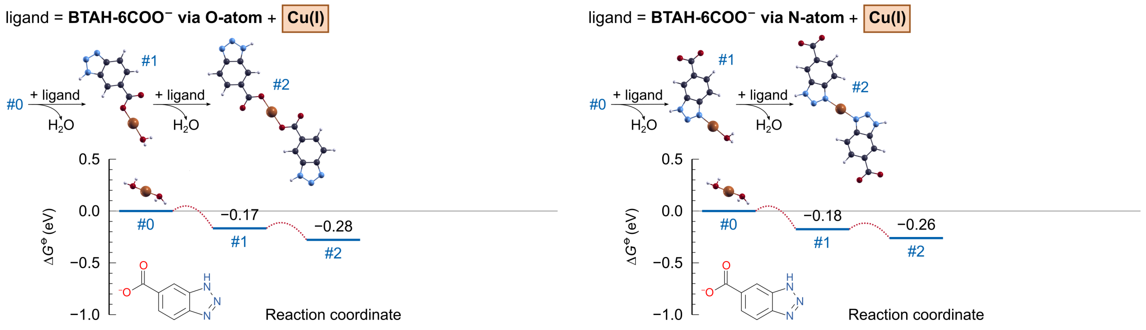

Figure C.2: Standard Gibbs energy ($\Delta G^\ominus$) reaction profiles for the formation of coordination complexes between the BTAH-6COO$^-$ ligand and the Cu(I) ion. Monodentate ligand bonding via O and N atoms is considered.

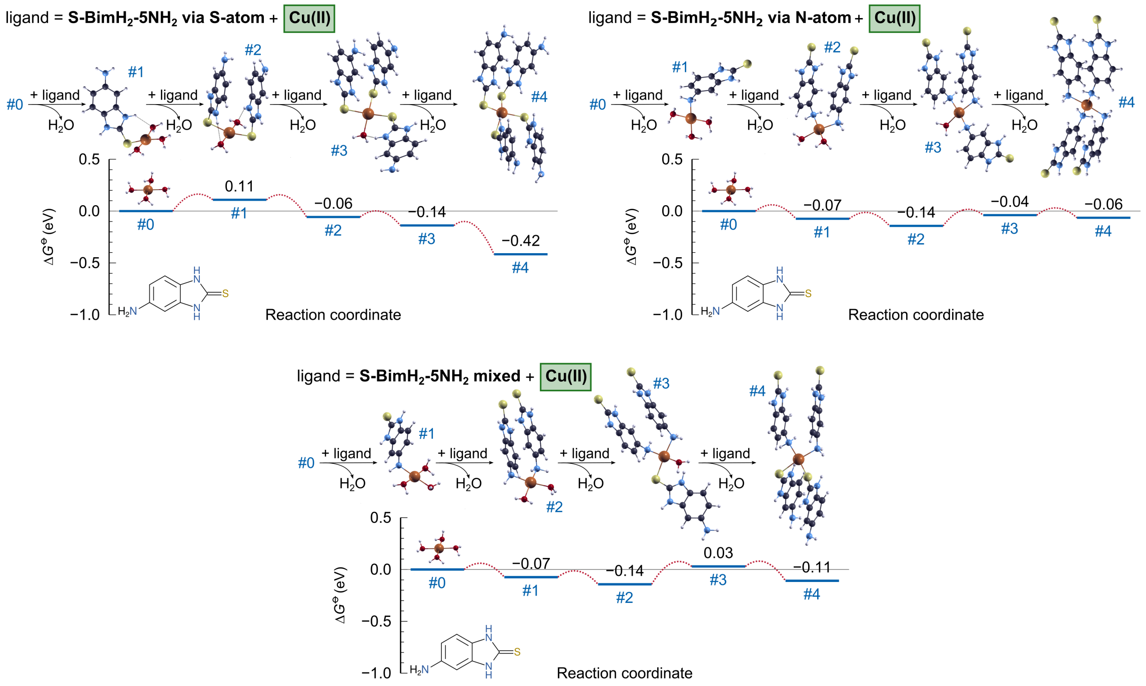

Figure C.3: Standard Gibbs energy ($\Delta G^\ominus$) reaction profiles for the formation of coordination complexes between the S-BimH$_2$-5NH$_2$ ligand and the Cu(II) ion. Different ligand bonding is considered, i.e., via S atom, N atom, and mixed.

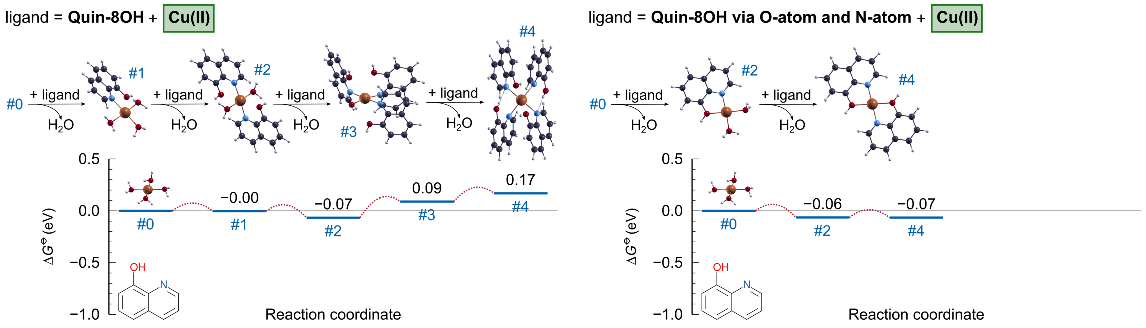

Figure C.4: Standard Gibbs energy ($\Delta G^{\ominus}$) reaction profiles for the formation of coordination complexes between the Quin-8OH ligand and the Cu(II) ion. Both monodentate and bidentate coordination is considered.

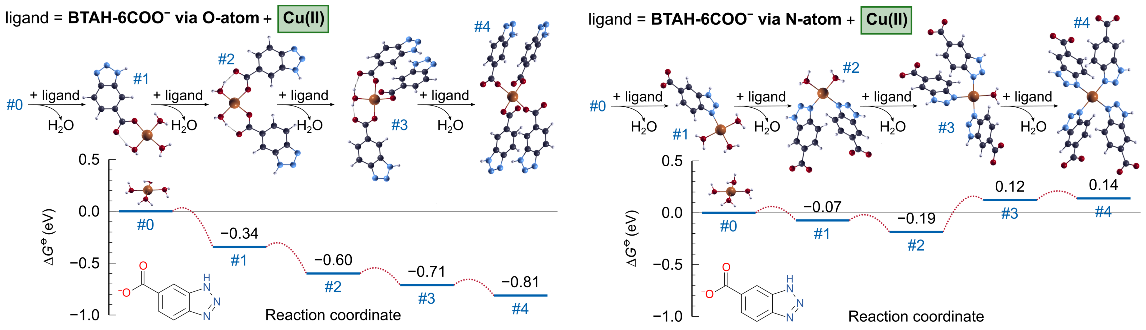

Figure C.5: Standard Gibbs energy ($\Delta G^{\ominus}$) reaction profiles for the formation of coordination complexes between the BTAH-6COO^{-} ligand and the Cu(II) ion. Monodentate ligand bonding via O and N atoms is considered.

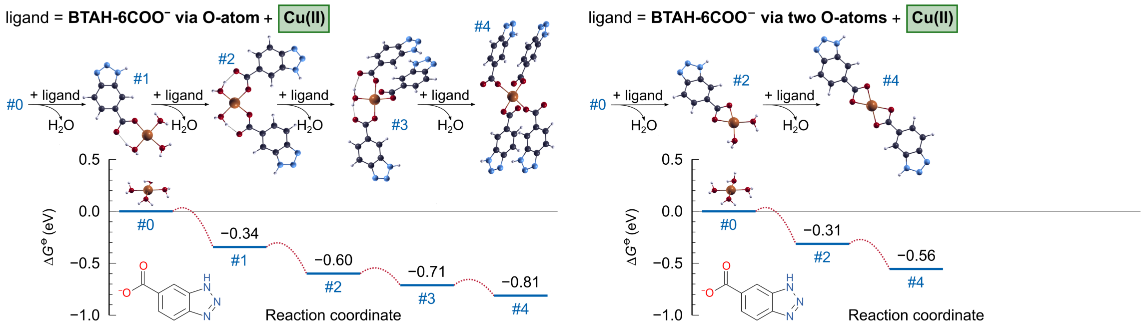

Figure C.6: Standard Gibbs energy ($\Delta G^{\ominus}$) reaction profiles for the formation of coordination complexes between the BTAH-6COO^{-} ligand and the Cu(II) ion. The via O-atom monodentate bonding is compared to the via O-atom bidentate bonding for the BTAH-6COO^{-} ligand.

References

[1] R. W. Revie, *Uhlig's corrosion handbook.* Chichester, England, UK, 2011.

[2] B. Hou, X. Li, X. Ma, C. Du, D. Zhang, M. Zheng, W. Xu, D. Lu, and F. Ma, "The cost of corrosion in China," *npj Mater. Degrad.*, vol. 1, pp. 1–10, 2017. DOI: `10.1038/s41529-017-0005-2`.

[3] V. S. Sastri, *Green corrosion inhibitors: Theory and practice.* Chichester, England, UK, 2011.

[4] A. Kokalj and D. Costa, "Molecular modeling of corrosion inhibitors," in *Encyclopedia of Interfacial Chemistry*, 2018, pp. 332–345. DOI: `10.1016/B978-0-12-409547-2.13444-4`.

[5] I. Milošev, "Contemporary modes of corrosion protection and functionalization of materials," *Acta Chim. Slov.*, vol. 66, pp. 511–533, 2019. DOI: `10.17344/acsi.2019.5162`.

[6] D. A. Winkler, "Predicting the performance of organic corrosion inhibitors," *Metals*, vol. 7, pp. 553-1–533-8, 2017. DOI: `10.3390/met7120553`.

[7] J. O. Bockris, A. K. Reddy, and M. E. Gamboa-Aldeco, *Modern electrochemistry 2B: Electrodics in chemistry, engineering, biology and environmental science.* New York, NY, USA: Springer, 1998, vol. 2.

[8] J. O. Bockris and D. A. J. Swinkels, "Adsorption of n-decylamine on solid metal electrodes," *J. Electrochem. Soc.*, vol. 111, pp. 736–743, 1964. DOI: `10.1149/1.2426222`.

[9] G. Gece, "The use of quantum chemical methods in corrosion inhibitor studies," *Corros. Sci.*, vol. 50, pp. 2981–2992, 2008. DOI: `10.1016/j.corsci.2008.08.043`.

[10] A. Kokalj, "Molecular modeling of organic corrosion inhibitors: Calculations, pitfalls, and conceptualization of molecule–surface bonding," *Corros. Sci.*, vol. 193, pp. 109650-1–109650-31, 2021. DOI: `10.1016/j.corsci.2021.109650`.

[11] I. B. Obot, D. D. Macdonald, and Z. M. Gasem, "Density functional theory (DFT) as a powerful tool for designing new organic corrosion inhibitors. Part 1: An overview," *Corros. Sci.*, vol. 99, pp. 1–30, 2015. DOI: `10.1016/j.corsci.2015.01.037`.

[12] A. Kokalj, "Ab initio modeling of the bonding of benzotriazole corrosion inhibitor to reduced and oxidized copper surfaces," *Faraday Discuss.*, vol. 180, pp. 415–438, 2015. DOI: `10.1039/C4FD00257A`.

[13] S. Peljhan and A. Kokalj, "DFT study of gas-phase adsorption of benzotriazole on Cu(111), Cu(100), Cu(110), and low coordinated defects thereon," *Phys. Chem. Chem. Phys.*, vol. 13, pp. 20 408–20 417, 2011. DOI: `10.1039/C1CP21873E`.

[14] Y. Jiang and J. B. Adams, "First principle calculations of benzotriazole adsorption onto clean Cu(111)," *Surf. Sci.*, vol. 529, pp. 428–442, 2003. DOI: `10.1016/S0039-6028(03)00277-2`.

[15] S. Peljhan, J. Koller, and A. Kokalj, "The effect of surface geometry of copper on adsorption of benzotriazole and Cl. Part I," *J. Phys. Chem. C*, vol. 118, pp. 933–943, 2014. DOI: `10.1021/jp409717e`.

[16] A. Kokalj, S. Peljhan, M. Finšgar, and I. Milošev, "What determines the inhibition effectiveness of ATA, BTAH, and BTAOH corrosion inhibitors on copper?" *J. Am. Chem. Soc.*, vol. 132, pp. 16 657–16 668, 2010. DOI: `10.1021/ja107704y`.

[17] P. Kutej, J. Vosta, J. Pancir, J. Macak, and N. Hackerman, "Electrochemical and quantum chemical study of dibenzylsulfoxide adsorption on iron," *J. Electrochem. Soc.*, vol. 142, pp. 829–834, 1995. DOI: `10.1149/1.2048543`.

[18] N. Kovačević and A. Kokalj, "The relation between adsorption bonding and corrosion inhibition of azole molecules on copper," *Corros. Sci.*, vol. 73, pp. 7–17, 2013. DOI: `10.1016/j.corsci.2013.03.016`.

[19] D. Gustinčič and A. Kokalj, "DFT study of azole corrosion inhibitors on Cu_2O model of oxidized copper surfaces: I. Molecule–surface and Cl–surface bonding," *Metals*, vol. 8, pp. 310-1–310-27, 2018. DOI: `10.3390/met8050310`.

[20] A. Kokalj, D. Gustinčič, M. Poberžnik, and M. Lozinšek, "New insights into adsorption bonding of imidazole: A viable C2–H bond cleavage on copper surfaces," *Appl. Surf. Sci.*, vol. 479, pp. 463–468, 2019. DOI: `10.1016/j.apsusc.2018.12.246`.

[21] J.-Y. Jhuang, S.-H. Lee, S.-W. Chen, Y.-H. Chen, Y.-J. Chen, J.-L. Lin, C.-H. Wang, and Y.-W. Yang, "Adsorption and reaction Pathways of 1*H*-pyrazole on Cu(100) and O/Cu(100)," *J. Phys. Chem. C*, vol. 122, pp. 6195–6208, 2018. DOI: `10.1021/acs.jpcc.8b00042`.

[22] S.-W. Chen, Y.-J. Chen, Y.-H. Chen, G.-J. Chen, S.-H. Chan, and J.-L. Lin, "Adsorption and reaction pathways of 1*H*-1,2,3-triazole on Cu(100) and O/Cu(100)," *J. Phys. Chem. C*, vol. 122, pp. 27 412–27 424, 2018. DOI: `10.1021/acs.jpcc.8b08007`.

[23] M. Finšgar and I. Milošev, "Inhibition of copper corrosion by 1,2,3-benzotriazole: A review," *Corros. Sci.*, vol. 52, pp. 2737–2749, 2010. DOI: `10.1016/j.corsci.2010.05.002`.

[24] N. Kovačević, I. Milošev, and A. Kokalj, "The roles of mercapto, benzene, and methyl groups in the corrosion inhibition of imidazoles on copper: II. Inhibitor–copper bonding," *Corros. Sci.*, vol. 98, pp. 457–470, 2015. DOI: `10.1016/j.corsci.2015.05.041`.

[25] C. Feiler, D. Mei, B. J. C. Luthringer-Feyerabend, S. V. Lamaka, and M. L. Zheludkevich, "Rational design of effective Mg degradation modulators," *Corrosion*, vol. 77, pp. 204–208, 2021. DOI: `10.5006/3597`.

[26] J. P. Perdew, K. Burke, and M. Ernzerhof, "Generalized gradient approximation made simple," *Phys. Rev. Lett.*, vol. 77, pp. 3865–3868, 1996. DOI: `10.1103/PhysRevLett.77.3865`.

[27] S. Grimme, "Semiempirical GGA-type density functional constructed with a long-range dispersion correction," *J. Comput. Chem.*, vol. 27, pp. 1787–1799, 2006. DOI: `10.1002/jcc.20495`.

[28] D. Gustinčič and A. Kokalj, "A DFT study of adsorption of imidazole, triazole, and tetrazole on oxidized copper surfaces: $Cu_2O(111)$ and $Cu_2O(111)$-w/o-Cu CUS," *Phys. Chem. Chem. Phys.*, vol. 17, pp. 28 602–28 615, 2015. DOI: `10.1039/C5CP03647`.

[29] E. R. McNellis, J. Meyer, and K. Reuter, "Azobenzene at coinage metal surfaces: Role of dispersive van der Waals interactions," *Phys. Rev. B*, vol. 80, pp. 205414-1–205414-10, 2009. DOI: `10.1103/PhysRevB.80.205414`.

[30] K. Tonigold and A. Groß, “Adsorption of small aromatic molecules on the (111) surfaces of noble metals: A density functional theory study with semiempirical corrections for dispersion effects,” *J. Chem. Phys.*, vol. 132, pp. 224701-1–224701-10, 2010. DOI: `10.1063/1.3439691`.

[31] A. Kokalj and S. Peljhan, “Density functional theory study of ATA, BTAH, and BTAOH as copper corrosion inhibitors: Adsorption onto Cu(111) from gas phase,” *Langmuir*, vol. 26, pp. 14 582–14 593, 2010. DOI: `10.1021/la1019789`.

[32] D. Vanderbilt, “Soft self-consistent pseudopotentials in a generalized eigenvalue formalism,” *Phys. Rev. B*, vol. 41, pp. 7892–7895, 1990. DOI: `10.1103/PhysRevB.41.7892`.

[33] Ultrasoft pseudopotentials for H, C, N, O, Cl, and Cu atoms were taken from the Quantum ESPRESSO Pseudopotential Download Page at `http://www.quantum-espresso.org/pseudopotentials` (files: `H.pbe-rrkjus.UPF`, `C.pbe-rrkjus.UPF`, `N.pbe-rrkjus.UPF`, `O.pbe-rrkjus.UPF`, `Cl.pbe-n-van.UPF`, and `Cu.pbe-d-rrkjus.UPF`), 2021.

[34] P. Giannozzi, S. Baroni, N. Bonini, M. Calandra, R. Car, C. Cavazzoni, D. Ceresoli, G. L. Chiarotti, M. Cococcioni, I. Dabo, A. Dal Corso, S. de Gironcoli, S. Fabris, G. Fratesi, R. Gebauer, U. Gerstmann, C. Gougoussis, A. Kokalj, M. Lazzeri, L. Martin-Samos, N. Marzari, F. Mauri, R. Mazzarello, S. Paolini, A. Pasquarello, L. Paulatto, C. Sbraccia, S. Scandolo, G. Sclauzero, A. P. Seitsonen, A. Smogunov, P. Umari, and R. M. Wentzcovitch, “QUANTUM ESPRESSO: a modular and open-source software project for quantum simulations of materials,” *J. Phys: Condens. Matter*, vol. 21, pp. 395502-1–395502-20, 2009, Code available from `http://www.quantum-espresso.org/`. DOI: `10.1088/0953-8984/21/39/395502`.

[35] P. Giannozzi, O. Andreussi, T. Brumme, O. Bunau, M. B. Nardelli, M. Calandra, R. Car, C. Cavazzoni, D. Ceresoli, M. Cococcioni, N. Colonna, I. Carnimeo, A. D. Corso, S. de Gironcoli, P. Delugas, R. DiStasio, A. Ferretti, A. Floris, G. Fratesi, G. Fugallo, R. Gebauer, U. Gerstmann, F. Giustino, T. Gorni, J. Jia, M. Kawamura, H.-Y. Ko, A. Kokalj, E. Küçükbenli, M. Lazzeri, M. Marsili, N. Marzari, F. Mauri, N. L. Nguyen, H.-V. Nguyen, A. Otero-de-la-Roza, L. Paulatto, S. Poncé, D. Rocca, R. Sabatini, B. Santra, M. Schlipf, A. P. Seitsonen, A. Smogunov, I. Timrov, T. Thonhauser, P. Umari, N. Vast, X. Wu, and S. Baroni, “Advanced capabilities for materials modelling with Quantum ESPRESSO,” *J. Phys: Condens. Matter*, vol. 29, pp. 465901-1–465901-31, 2017. DOI: `doi:10.1088/1361-648X/aa8f79`.

[36] Kokalj, Anton, *Pwtk: Pwscf toolkit*, version 2.1, 2021. [Online]. Available: `https://pwtk.ijs.si/`.

[37] A. Kokalj, “XCrySDen–a new program for displaying crystalline structures and electron densities,” *J. Mol. Graph. Model.*, vol. 17, pp. 176–179, 1999, Code available from `http://www.xcrysden.org/`.

[38] T. Williams, C. Kelley, and et al., *Gnuplot 4.4*, http://www.gnuplot.info/, 2011.

[39] Ink. Proj., *Inkscape*, version 1.0.2, 2023. [Online]. Available: `https://inkscape.org`.

[40] D. K. Kozlica, A. Kokalj, and I. Milošev, “Synergistic effect of SH-BimH and octylphosphonic acid as corrosion inhibitors for copper and aluminium – An electrochemical, XPS, FTIR and DFT study,” *Corros. Sci.*, vol. 182, pp. 109082-1–109082-26, 2021. DOI: `10.1016/j.corsci.2020.109082`.

[41] L. Bengtsson, “Dipole correction for surface supercell calculations,” *Phys. Rev. B*, vol. 59, pp. 12 301–12 304, 1999. DOI: `10.1103/PhysRevB.59.12301`.

[42] H. J. Monkhorst and J. D. Pack, “Special points for Brillouin-zone integrations,” *Phys. Rev. B*, vol. 13, pp. 5188–5192, 1976. DOI: `10.1103/PhysRevB.13.5188`.

[43] M. Methfessel, D. Hennig, and M. Scheffler, “Trends of the surface relaxations, surface energies, and work functions of the $4d$ transition metals,” *Phys. Rev. B*, vol. 46, pp. 4816–4829, 1992. DOI: `10.1103/PhysRevB.46.4816`.

[44] W. Tang, E. Sanville, and G. Henkelman, “A grid-based Bader analysis algorithm without lattice bias,” *J. Phys.: Condens. Matter*, vol. 21, pp. 084204-1–084204-7, 2009. DOI: `10.1088/0953-8984/21/8/084204`.

[45] A. Arnaldsson, W. Tang, G. Henkelman, and et al., “Computer program for Bader charge analysis,” Code avaialble from: `http://theory.cm.utexas.edu/henkelman/code/bader/`, 2019.

[46] P. E. Blochl, “Projector augmented-wave method,” *Phys. Rev. B*, vol. 50, pp. 17 953–17 979, 1994. DOI: `10.1103/PhysRevB.50.17953`.

[47] PAW potentials where obtained from a pseudopotenital library [107], `https://dalcorso.github.io/pslibrary`, version 1.0.0 (files: `H.pbe-kjpaw_psl.1.0.0.UPF`, `C.pbe-n-kjpaw_psl.1.0.0.UPF`, `N.pbe-n-kjpaw_psl.1.0.0.UPF`, `O.pbe-n-kjpaw_psl.1.0.0.UPF`, `Cl.pbe-n-kjpaw_psl.1.0.0.UPF`, and `Cu.pbe-dn-kjpaw_psl.1.0.0.UPF`), 2017.

[48] H. S. Yu, X. He, S. L. Li, and D. G. Truhlar, “MN15: A Kohn–Sham global-hybrid exchange–correlation density functional with broad accuracy for multi-reference and single-reference systems and noncovalent interactions,” *Chem. Sci.*, vol. 7, pp. 5032–5051, 2016. DOI: `10.1039/C6SC00705H`.

[49] M. J. Frisch, G. W. Trucks, H. B. Schlegel, G. E. Scuseria, M. A. Robb, J. R. Cheeseman, G. Scalmani, V. Barone, G. A. Petersson, H. Nakatsuji, X. Li, M. Caricato, A. V. Marenich, J. Bloino, B. G. Janesko, R. Gomperts, B. Mennucci, H. P. Hratchian, J. V. Ortiz, A. F. Izmaylov, J. L. Sonnenberg, D. Williams-Young, F. Ding, F. Lipparini, F. Egidi, J. Goings, B. Peng, A. Petrone, T. Henderson, D. Ranasinghe, V. G. Zakrzewski, J. Gao, N. Rega, G. Zheng, W. Liang, M. Hada, M. Ehara, K. Toyota, R. Fukuda, J. Hasegawa, M. Ishida, T. Nakajima, Y. Honda, O. Kitao, H. Nakai, T. Vreven, K. Throssell, J. A. Montgomery Jr., J. E. Peralta, F. Ogliaro, M. J. Bearpark, J. J. Heyd, E. N. Brothers, K. N. Kudin, V. N. Staroverov, T. A. Keith, R. Kobayashi, J. Normand, K. Raghavachari, A. P. Rendell, J. C. Burant, S. S. Iyengar, J. Tomasi, M. Cossi, J. M. Millam, M. Klene, C. Adamo, R. Cammi, J. W. Ochterski, R. L. Martin, K. Morokuma, O. Farkas, J. B. Foresman, and D. J. Fox, *Gaussian 16 Revision A.03*, Gaussian Inc. Wallingford CT, 2016.

[50] F. Weigend and R. Ahlrichs, “Balanced basis sets of split valence, triple zeta valence and quadruple zeta valence quality for H to Rn: Design and assessment of accuracy,” *Phys. Chem. Chem. Phys.*, vol. 7, pp. 3297–3305, 2005. DOI: `10.1039/B508541A`.

[51] A. V. Marenich, C. J. Cramer, and D. G. Truhlar, “Universal solvation model based on solute electron density and on a continuum model of the solvent defined by the bulk dielectric constant and atomic surface tensions,” *J. Phys. Chem. B*, vol. 113, pp. 6378–6396, 2009. DOI: `10.1021/jp810292n`.

[52] G. Luchini, J. V. Alegre-Requena, I. Funes-Ardoiz, and R. S. Paton, “GoodVibes: automated thermochemistry for heterogeneous computational chemistry data,” *F1000 Research*, vol. 9, pp. 291-1–291-14, 2020. DOI: `10.12688/f1000research.22758.1`.

[53] R. F. Ribeiro, A. V. Marenich, C. J. Cramer, and D. G. Truhlar, "Use of solution-phase vibrational frequencies in continuum models for the free energy of solvation," *J. Phys. Chem. B*, vol. 115, pp. 14 556–14 562, 2011. DOI: `10.1021/jp205508z`.

[54] A. Kokalj, M. Lozinšek, B. Kapun, P. Taheri, S. Neupane, P. Losada-Pérez, C. Xie, S. Stavber, D. Crespo, F. U. Renner, A. Mol, and I. Milošev, "Simplistic correlations between molecular electronic properties and inhibition efficiencies: Do they really exist?" *Corros. Sci.*, vol. 179, pp. 108856-1–108856-12, 2021. DOI: `10.1016/j.corsci.2020.108856`.

[55] S. L. Dixon and P. C. Jurs, "Estimation of pKa for organic oxyacids using calculated atomic charges," *J. Comput. Chem.*, vol. 14, pp. 1460–1467, 2004. DOI: `10.1002/jcc.540141208`.

[56] J. W. Ochterski, "Thermochemistry in gaussian," *Gaussian Inc.*, vol. 1, pp. 1–19, 2000.

[57] V. S. Bryantsev, M. S. Diallo, A. C. T. van Duin, and W. A. Goddard Iii, "Hydration of copper(II): new insights from Density functional theory and the COSMO solvation model," *J. Phys. Chem. A*, vol. 112, pp. 9104–9112, 2008. DOI: `10.1021/jp804373p`.

[58] J. V. Burda, M. Pavelka, and M. Šimánek, "Theoretical model of copper Cu(I)/Cu(II) hydration. DFT and ab initio quantum chemical study," *J. Mol. Struct. THEOCHEM*, vol. 683, pp. 183–193, 2004. DOI: `10.1016/j.theochem.2004.06.013`.

[59] M. Dlouhy and A. Kokalj, "How adsorbed H, O, OH, and Cl affect plain adsorption of imidazole on copper," *Corros. Sci.*, vol. 205, pp. 110443-1–110443-15, 2022. DOI: `10.1016/j.corsci.2022.110443`.

[60] A. Kokalj and M. Dlouhy, "Dissociative adsorption of azoles on Cu(111) promoted by chemisorbed O and OH," *Corros. Sci.*, vol. 209, pp. 110680-1–110680-12, 2022. DOI: `10.1016/j.corsci.2022.110680`.

[61] N. Kovačević and A. Kokalj, "DFT study of interaction of azoles with Cu(111) and Al(111) surfaces: role of azole nitrogen atoms and dipole–dipole interactions," *J. Phys. Chem. C*, vol. 115, pp. 24 189–24 197, 2011. DOI: `10.1021/jp207076w`.

[62] S. Sun, Y. Geng, L. Tian, S. Chen, Y. Yan, and S. Hu, "Density functional theory study of imidazole, benzimidazole and 2-mercaptobenzimidazole adsorption onto clean Cu(111) surface," *Corros. Sci.*, vol. 63, pp. 140–147, 2012. DOI: `10.1016/j.corsci.2012.05.024`.

[63] N. Kovačević and A. Kokalj, "Analysis of molecular electronic structure of imidazole- and benzimidazole-based inhibitors: a simple recipe for qualitative estimation of chemical hardness," *Corros. Sci.*, vol. 53, pp. 909–921, 2010. DOI: `10.1016/j.corsci.2010.11.016`.

[64] K. Cho, J. Kishimoto, T. Hashizume, H. Pickering, and T. Sakurai, "Adsorption and film growth of BTA on clean and oxygen adsorbed Cu(110) surfaces," *Appl. Surf. Sci.*, vol. 87, pp. 380–385, 1995. DOI: `10.1016/0169-4332(94)00506-0`.

[65] D. R. Lide, *Ionic radii in crystals.* Andover, England, UK: Taylor & Francis, 2005, pp. 12-14–12-16.

[66] S. Yang, X. Zhao, Z. Qi, Y.-H. Lu, G. Somorjai, P. Yang, A. Baskin, D. Prendergast, and M. Salmeron, "Chloride-assisted corrosion of copper and protection by benzotriazole," *ACS Appl. Mater. Interfaces*, vol. 14, pp. 6093–6101, 2022. DOI: `10.1021/acsami.1c15808`.

[67] P. Broekmann, M. Wilms, M. Kruft, C. Stuhlmann, and K. Wandelt, "In-situ STM investigation of specific anion adsorption on Cu(111)," *J. Electroanal. Chem.*, vol. 467, pp. 307–324, 1999. DOI: `10.1016/S0022-0728(99)00048-0`.

[68] S. Peljhan and A. Kokalj, "Adsorption of chlorine on Cu(111): A density-functional theory study," *J. Phys. Chem. C*, vol. 113, pp. 14 363–14 376, 2009. DOI: `10.1021/jp902273k`.

[69] D. K. Kozlica, J. Ekar, J. Kovač, and I. Milošev, "Roles of chloride ions in the formation of corrosion protective films on copper," *J. Electrochem. Soc.*, vol. 168, pp. 031504-1–031504-17, 2021. DOI: `10.1149/1945-7111/abe34a`.

[70] D. K. Kozlica, J. Ekar, J. Kovač, and I. Milošev, "Roles of chloride ions in the formation of corrosion protective films on copper," *J. Electrochem. Soc.*, vol. 168, pp. 031504-1–031504-17, 2021. DOI: `10.1149/1945-7111/abe34a`.

[71] A. Kokalj, "Corrosion inhibitors: physisorbed or chemisorbed?" *Corros. Sci.*, vol. 196, pp. 109939-1–109939-15, 2022. DOI: `10.1016/j.corsci.2021.109939`.

[72] A. Soon, M. Todorova, B. Delley, and C. Stampfl, "Oxygen adsorption and stability of surface oxides on Cu(111): A first-principles investigation," *Phys. Rev. B*, vol. 73, pp. 165424-1–165424-12, 2006. DOI: `10.1103/PhysRevB.73.165424`.

[73] ——, "Surface oxides of the oxygen–copper system: Precursors to the bulk oxide phase?" *Surf. Sci.*, vol. 601, pp. 5809–5813, 2007. DOI: `10.1016/j.susc.2007.06.062`.

[74] D. Gustinčič and A. Kokalj, "DFT study of azole corrosion inhibitors on Cu_2O Model of oxidized copper surfaces: II. lateral interactions and thermodynamic stability," *Metals*, vol. 8, pp. 311-1–311-28, 2018. DOI: `10.3390/met8050311`.

[75] L. Gašparič, M. Poberžnik, and A. Kokalj, "DFT study of hydrogen bonding between metal hydroxides and organic molecules containing N, O, S, and P heteroatoms: clusters vs. surfaces," *Chem. Phys.*, vol. 559, pp. 111539-1–111539-14, 2022. DOI: `10.1016/j.chemphys.2022.111539`.

[76] R. G. Pearson, "Absolute electronegativity and hardness: application to inorganic chemistry," *Inorg. Chem.*, vol. 27, pp. 734–740, 1988. DOI: `10.1021/ic00277a030`.

[77] A. Kokalj, "On the HSAB based estimate of charge transfer between adsorbates and metal surfaces," *Chem. Phys.*, vol. 393, pp. 1–12, 2012. DOI: `10.1016/j.chemphys.2011.10.021`.

[78] P. Crawford and P. Hu∗, "Importance of electronegativity differences and surface structure in molecular dissociation reactions at transition metal surfaces," *J. Phys. Chem. B*, vol. 110, pp. 2429–24 935, 2006. DOI: `10.1021/jp063472u`.

[79] W. Yang and R. G. Parr, "Hardness, softness, and the Fukui function in the electronic theory of metals and catalysis," *Proc. Natl. Acad. Sci. U.S.A.*, vol. 82, pp. 6723–6726, 1985. DOI: `10.1073/pnas.82.20.6723`.

[80] Y. I. Kuznetsov and L. Kazansky, "Physicochemical aspects of metal protection by azoles as corrosion inhibitors," *Russ. Chem. Rev.*, vol. 77, pp. 219–232, 2008. DOI: `10.1070/rc2008v077n03abeh003753`.

[81] A. Kokalj, N. Kovačević, S. Peljhan, M. Finšgar, A. Lesar, and I. Milošev, "Triazole, benzotriazole, and naphthotriazole as copper corrosion inhibitors: I. Molecular electronic and adsorption properties," *ChemPhysChem*, vol. 12, pp. 3547–3555, 2011. DOI: `10.1002/cphc.201100537`.

[82] X. Chen and H. Häkkinen, "Divide and protect: passivating Cu(111) by Cu-(BTAH)$_2$," *J. Phys. Chem. C*, vol. 116, pp. 22 346–22 349, 2012. DOI: `10.1021/jp3055894`.

[83] A. Kokalj and S. Peljhan, "Density Functional Theory Study of Adsorption of Benzotriazole on Cu_2O Surfaces," *J. Phys. Chem. C*, vol. 119, pp. 11 625–11 635, 2015. DOI: `10.1021/acs.jpcc.5b01677`.

[84] F. Grillo, D. W. Tee, S. M. Francis, H. A. Früchtl, and N. V. Richardson, "Passivation of copper: Benzotriazole films on Cu(111)," *J. Phys. Chem. C*, vol. 118, no. 16, pp. 8667–8675, 2014. DOI: `10.1021/jp411482e`.

[85] C. Gattinoni and A. Michaelides, "Understanding corrosion inhibition with van der Waals DFT methods: the case of benzotriazole," *Faraday Discuss.*, vol. 180, pp. 439–458, 2015. DOI: `10.1039/C4FD00273C`.

[86] C. Gattinoni, P. Tsaousis, C. Euaruksakul, R. Price, D. A. Duncan, T. Pascal, D. Prendergast, G. Held, and A. Michaelides, "Adsorption behavior of organic molecules: A study of benzotriazole on Cu(111) with spectroscopic and theoretical methods," *Langmuir*, vol. 35, pp. 882–893, 2019. DOI: `10.1021/acs.langmuir.8b03528`.

[87] M. Turano, M. Walker, F. Grillo, C. Gattinoni, J. Edmondson, O. Adesida, G. Hunt, P. M. Kirkman, N. V. Richardson, C. J. Baddeley, A. Michaelides, and G. Costantini, "Understanding the interaction of organic corrosion inhibitors with copper at the molecular scale: Benzotriazole on Cu(110)," *Appl. Surf. Sci.*, vol. 570, pp. 151206-1–151206-15, 2021. DOI: `10.1016/j.apsusc.2021.151206`.

[88] H. Wang, Y. Hao, S. Chen, M. Cheng, C. Li, S. Sun, and S. Hu, "DFT study of imidazoles adsorption on the grain boundary of Cu(100) surface," *Corros. Sci.*, vol. 137, pp. 33–42, 2018. DOI: `10.1016/j.corsci.2018.03.009`.

[89] D. Kumar, V. Jain, and B. Rai, "Imidazole derivatives as corrosion inhibitors for copper: A DFT and reactive force field study," *Corros. Sci.*, vol. 171, pp. 108724-1–108724-9, 2020. DOI: `10.1016/j.corsci.2020.108724`.

[90] A. Kokalj, S. Peljhan, and J. Koller, "The effect of surface geometry of copper on dehydrogenation of benzotriazole. Part II," *J. Phys. Chem. C*, vol. 118, pp. 944–954, 2014. DOI: `10.1021/jp409719c`.

[91] A. Kokalj, "Formation and structure of inhibitive molecular film of imidazole on iron surface," *Corros. Sci.*, vol. 68, pp. 195–203, 2013. DOI: `10.1016/j.corsci.2012.11.015`.

[92] ——, "Electrostatic model for treating long-range lateral interactions between polar molecules adsorbed on metal surfaces," *Phys. Rev. B*, vol. 84, pp. 045418-1–045418-17, 2011. DOI: `10.1103/PhysRevB.84.045418`.

[93] C. T. Campbell, Y.-K. Sun, and W. H. Weinberg, "Trends in preexponential factors and activation energies in dehydrogenation and dissociation of adsorbed species," *Chem. Phys. Lett.*, vol. 179, pp. 53–57, 1991. DOI: `10.1016/0009-2614(91)90290-P`.

[94] V. P. Zhdanov, J. Pavlíček, and Z. Knor, "Preexponential factors for elementary surface processes," *Catal. Rev.*, vol. 30, pp. 501–517, 1988. DOI: `10.1080/016149488080`.

[95] V. P. Zhdanov, "Arrhenius parameters for rate processes on solid surfaces," *Surf. Sci. Rep.*, vol. 12, pp. 185–242, 1991. DOI: `10.1016/0167-5729(91)90011-L`.

[96] J. Torras and C. Alemán, "Determination of New Cu^+, Cu^{2+}, and Zn^{2+} Lennard-Jones ion parameters in acetonitrile," *J. Phys. Chem. B*, vol. 117, pp. 10 513–10 522, 2013. DOI: `10.1021/jp402545g`.

[97] C. P. Kelly, C. J. Cramer, and D. G. Truhlar, "Aqueous solvation free energies of ions and ion-Water clusters based on an accurate value for the absolute aqueous solvation free energy of the proton," *J. Phys. Chem. B*, vol. 110, pp. 16 066–16 081, 2006. DOI: `10.1021/jp063552y`.

[98] V. S. Bryantsev, M. S. Diallo, and W. A. I. Goddard, "Computational study of copper(II) complexation and hydrolysis in aqueous solutions using mixed cluster/continuum models," *J. Phys. Chem. A*, vol. 113, pp. 9559–9567, 2009. DOI: `10.1021/jp904816d`.

[99] H. P. Lee and K. Nobe, "Kinetics and mechanisms of Cu electrodissolution in chloride media," *J. Electrochem. Soc.*, vol. 133, pp. 2035–2043, 1986. DOI: `10.1149/1.2108335`.

[100] C. Deslouis, B. Tribollet, G. Mengoli, and M. M. Musiani, "Electrochemical behaviour of copper in neutral aerated chloride solution. I. Steady-state investigation," *J. Appl. Electrochem.*, vol. 18, pp. 374–383, 1988. DOI: `10.1007/BF01093751`.

[101] J. Fritz, "Chloride complexes of copper(I) chloride in aqueous solution," *J. Phys. Chem.*, vol. 84, pp. 2241–2246, 1980.

[102] R. Arnek, I. Puigdomenech, M. Valiente, *et al.*, "A calorimetric study of copper(II) chloride complexes in aqueous solution," *Acta Chem. Scand. A*, vol. 36, pp. 15–19, 1982. DOI: `10.3891/acta.chem.scand.36a-0015`.

[103] M. Khan and M. Schwing-Weill, "Stability and electronic spectra of the copper(II) chloro complexes in aqueous solutions," *Inorg. Chem.*, vol. 15, pp. 2202–2205, 1976. DOI: `10.1021/ic50163a041`.

[104] A. G. Kudrev, "Calculations of the intrinsic constants of the complexation between Cu(II) and halide ions in solution," *Russ. J. Coord. Chem.*, vol. 34, pp. 34–37, 2008. DOI: `10.1134/S1070328408010065`.

[105] I. Milošev, N. Kovačević, J. Kovač, and A. Kokalj, "The roles of mercapto, benzene and methyl groups in the corrosion inhibition of imidazoles on copper: I. Experimental characterization," *Corros. Sci.*, vol. 98, pp. 107–118, 2015. DOI: `10.1016/j.corsci.2015.05.006`.

[106] A. Kokalj, C. Xie, I. Milošev, and D. Crespo, "How relevant are molecular electronic parameters for predicting corrosion inhibition efficiency: imidazoles as corrosion inhibitors of Cu/Zr materials in NaCl solution," *Corros. Sci.*, vol. 193, pp. 109900-1–109900-16, 2021. DOI: `10.1016/j.corsci.2021.109900`.

[107] A. Dal Corso, "Pseudopotentials periodic table: From H to Pu," *Comput. Mater. Sci.*, vol. 95, pp. 337–350, 2014. DOI: `10.1016/j.commatsci.2014.07.043`.

Bibliography

Publications Related to the Thesis

Journal Articles

M. Dlouhy and A. Kokalj, "How adsorbed H, O, OH, and Cl affect plain adsorption of imidazole on copper," *Corros. Sci.*, vol. 205, pp. 110443-1–110443-15, 2022. DOI: `10.1016/j.corsci.2022.110443`.

A. Kokalj and M. Dlouhy, "Dissociative adsorption of azoles on Cu(111) promoted by chemisorbed O and OH," *Corros. Sci.*, vol. 209, pp. 110680-1–110680-12, 2022. DOI: `10.1016/j.corsci.2022.110680`.

Published Scientific Conference Contribution Abstracts

M. Dlouhy and A. Kokalj, "The role of small coadsorbates on adsorption of azole molecules on copper surfaces," in *Book of abstracts: 25th Annual Meeting of the Slovenian Chemical Society*, Maribor, Slovenia: Slovenian Chemical Society, 2019.

——, "How azole corrosion inhibitors affect adsorption of corrosion relevant species," in *Book of abstracts: 11th Jožef Stefan International Postgraduate School Students' Conference and 13th Young Researchers' Day*, Planica, Slovenia: Jožef Stefan International Postgraduate School, 2019.

——, "Adsorption of azole-type corrosion inhibitors in the presence of coadsorbed corrosion-relevant species on Cu(111)," in *Book of abstracts: Quantum ESPRESSO Summer School on Advanced Materials and Molecular Modelling*, Ljubljana, Slovenia: Jožef Stefan Institute, 2019.

——, "Adsorption of imidazole on Cu(111) covered with corrosion relevant species," in *Book of abstracts: 26th Annual Meeting of the Slovenian Chemical Society*, Portorose, Slovenia: Slovenian Chemical Society, 2020.

——, "A DFT study of coadsorption between azole-type corrosion inhibitor molecules and corrosive relevant species on copper surfaces," in *Book of abstracts: 12th Jožef Stefan International Postgraduate School Students' Conference and 14th Young Researchers' Day*, Ljubljana, Slovenia: Jožef Stefan International Postgraduate School, 2020.

——, "A DFT study of adsorption of imidazole on copper surfaces covered with corrosion-relevant species," in *Book of abstracts: 13th Jožef Stefan International Postgraduate School Students' Conference and 15th Young Researchers' Day*, Ljubljana, Slovenia: Jožef Stefan International Postgraduate School, 2020.

——, "The effect of corrosion relevant species on the adsorption of imidazole on copper," in *Book of abstracts: 27th Annual Meeting of the Slovenian Chemical Society*, Portorose, Slovenia: Slovenian Chemical Society, 2021.

——, “How adsorbed H, O, OH, and Cl affect on the adsorption of imidazole on copper,” in *CrossNano: Crossborder Workshop in Nanoscience and Nanotechnology*, Ljubljana, Slovenia: Jožef Stefan International Postgraduate School, 2022.

M. Dlouhy, S. Stevanoska, L. Gašparič, A. Kokalj, and S. Džeroski, “Towards predicting corrosion inhibitors’ performance with machine learning,” in *Young researcher’s workshop on Machine learning for materials*, Trieste, Italy: SISSA Miramare Campus, 2022.

M. Dlouhy and A. Kokalj, “How corrosion-relevant species affect the adsorption of imidazole on copper surface,” in *European Corrosion Congress, Corrosion in a Changing World - Energy, Mobility and Digitallization*, Berlin, Germany: European Federation of Corrosion, 2022.

Biography

Matjaž Dlouhy grew up in a small village called Boračeva near Radenci. After finishing secondary school at Gimnazija Franca Miklošiča Ljutomer, he enrolled in the Chemistry study program at the Faculty of Chemistry and Chemical Technology at the University of Ljubljana. In 2015, he started collaborating with Senior Research Associate Dr. Antonija Lesar at the Jožef Stefan Institute (JSI) and was awarded a JSI scholarship in the same year. A year later, he graduated with a Bachelor's degree in Chemistry, with a thesis entitled "*Structure and Reactivity of Methyl Radical*" under the supervision of Prof. Dr. Tomaž Urbič.

In 2018, Matjaž received his Master's degree in Chemistry at the same faculty with a thesis entitled "*Reactivity and Stability of Hydrotrioxy Radical*" under the supervision of Prof. Dr. Tomaž Urbič and Senior Research Associate Dr. Antonija Lesar. That same year, he began working as a young researcher at JSI under the mentorship of Prof. Dr. Anton Kokalj and enrolled in the Ph.D. program in Nanosciences and Nanotechnologies at the Jožef Stefan International Postgraduate School. His research interests now include molecular modeling and the study of corrosion inhibition processes, among others, in accordance with his dissertation topic.

Throughout his career, Matjaž has been involved in organizing various conferences, workshops, and round table discussions, including the Quantum ESPRESSO Summer School on Advanced Materials and Molecular Modelling (2019), the 13th Jožef Stefan International Postgraduate School Students' Conference and 15th Young Researchers' Day (2021), the 4th and 5th Cutting Edge Conference (2021 and 2023), and a round table discussion on Ethics in Science (2022). In 2019, he became a member of the Association of Chemical Sciences Researchers of the Faculty of Chemistry and Chemical Technology at the University of Ljubljana – Cutting Edge, and in 2022, he was elected its president. Matjaž actively collaborates with The Association for Technical Culture of Slovenia (ZOTKS), where he prepares students for international scientific competitions and fairs. At ZOTKS, he is also a member of the committee responsible for the preparation of national chemistry competitions for primary and secondary school students. Matjaž has co-mentored two secondary school research projects that were acknowledged and awarded by the Krka prize committee in 2021 and 2022. Both research works were also awarded a golden award at the annual Meetings of Young Researchers of Slovenia. He has also co-authored Chemistry textbooks and workbooks for high school students. In recent years, Matjaž has served as a Society for Science Judge, selecting the best student projects in chemistry at the Regeneron International Science and Engineering Fair in the United States of America.